Simulation of Nearshore Processes and Testing of Implicit and Explicit Vegetation Representations in SWAN

Christophe Baron-Hyppolite

Simulation of Nearshore Process and Testing of Implicit and Explicit Vegetation Representation in SWAN

By

Christophe Baron-Hyppolite

in partial fulfilment of the requirements for the degree of

Master of Science

Coastal Maritime Engineering and Management

at the Delft University of Technology,
to be defended publicly on Wednesday July 18, 2018 at 11:30 AM.

Supervisor:	Dr. ir. J.D. Bricker	TU Delft
Thesis committee:	Prof. Dr.ir. S.G.J. Aarninkhof,	TU Delft
	Dr.ir.M.Zijlema,	TU Delft
	Msc.C.H.Lashley,	TU Delft
	Dr.ir. Celso Ferreira	GMU

ERASMUS +: ERASMUS MUNDUS MOBILITY PROGRAMME

Master of Science in

COASTAL AND MARINE ENGINEERING AND
MANAGEMENT

CoMEM

**Simulation of Nearshore Process and Testing of Implicit and
Explicit Vegetation Representation in SWAN**

Delft University of Technology
18 July 2018

Christophe Baron-Hyppolite

The Erasmus+: Erasmus Mundus MSc in Coastal and Marine Engineering and Management is an integrated programme including mobility organized by five European partner institutions, coordinated by Norwegian University of Science and Technology (NTNU).

The joint study programme of 120 ECTS credits (two years full-time) has been obtained at two or three of the five CoMEM partner institutions:

- Norges Teknisk- Naturvitenskapelige Universitet (NTNU) Trondheim, Norway
- Technische Universiteit (TU) Delft, The Netherlands
- Universitat Politècnica de Catalunya (UPC). BarcelonaTech. Barcelona, Spain
- University of Southampton, Southampton, Great Britain
- City University London, London, Great Britain

During the first three semesters of the programme, students study at two or three different universities depending on their track of study. In the fourth and final semester an MSc project and thesis has to be completed. The two-year CoMEM programme leads to a multiple set of officially recognized MSc diploma certificates. These will be issued by the universities that have been attended by the student. The transcripts issued with the MSc Diploma Certificate of each university include grades/marks and credits for each subject.

Information regarding the CoMEM programme can be obtained from the programme coordinator:

Øivind A. Arntsen, Dr.ing.
Associate professor in Marine Civil Engineering
Department of Civil and Environmental Engineering
NTNU Norway
Mob.: +4792650455 Fax: + 4773597021
Email: oivind.arntsen@ntnu.no

CoMEM URL: https://www.ntnu.edu/studies/mscomem

CoMEM Thesis

This thesis was completed by:
Christophe Baron-Hyppolite

Under supervision of:
Dr. ir. J.D. Bricker

As a requirement to attend the degree of
Erasmus+: Erasmus Mundus Master in Coastal and Marine Engineering and Management (CoMEM)

Taught at the following educational institutions:

Norges Teknisk- Naturvitenskapelige Universitet (NTNU)
Trondheim, Norway

Technische Universiteit (TU) Delft
Delft, The Netherlands

University of Southampton,
Southampton, Great Britain

At which the student has studied from August 2016 to July 2018.

Preface

The research is carried out as part of the completion of the Coastal and Marine Engineering and Management Erasmus master's program. The papers primary focus is on wave attenuation by coastal saltmarshes, specifically focusing on the representation of the vegetation. Due to the field data made available by GMU, modelling of the larger coastal region is possible and therefore carried out. The paper includes validation for all models as well as the comparison of the vegetation implementation.

C. Baron-Hyppolite
Delft, July 2018

Acknowledgements

There are many people responsible for my initial curiosity of this coastal engineering program. This this is a culmination of two years of very hard work, where support received by friends, family, supervisors and professors were vital to completing this program successfully.

This research process was both challenging and rewarding providing an opportunity to pick up multiple skills that will serve me well in the future. It also exposed me to the research process, which taught me to be more critical of my work and organisation. My ability to learn and adapt to different challenges were greatly helped by my two daily supervisors Dr. Jeremy Bricker and Phd. Chris Lashley, who were key to the successful completion of this research through our weekly meetings and daily guidance. They were consistently available for help, and provided constructive advice every step of the way. I would also like to thank Prof. Marcel Zijlema for promptly answering any questions I had on modelling using SWAN Standalone, no matter how simple the answer might be and Prof. Stefan Aarninkhof for his guidance and advice during the committee meetings.

I would also like to thank The George Mason University team who provided the field data vital to the creating and validating the models. Prof. Celso Ferreira provided vital insite during our weekly skype meeting stemming from his experience studying Chesapeake bay sites. Phd. Juan Garzon and undergrad Tyler Miesse oversaw processing of the field data sets and answered vital questions on interpreting the provided data, often answering questions that cleared major road blocks throughout the research process. Both the Delft and GMU teams provided vital encouragement and guidance that were necessary when the modelling got difficult.

Beyond the immediate help there are a number of people that provided there support through opportunities and encouragement they provided. I would first like to begin with Micheal and Gerald Songy for their initial guidance and suggestion to take chance and apply to this program. A special thanks to Prof. Øivind Arntsen, Sonja Marie Ekrann Hammer, Prof. Rober Nicholls and Madelon Burgmeijer for provideing the guidance and support to not only properly integrate myself in each university but exposed me to the culture of the host counties. I will also never forget my colleagues that were present everyday whether it be Charles Feys, Tom Cowen, or Albert Monclus Abadel who provided advice on Matlab and modelling in the room, or Ines Baez Rivero, Nadar Naderi and Michelle Gostic who along with the other provided needed escape during lunch time or after "work".

I would also like to thank my family and friends back home who provided their support. Whether it be intentional or not, the weekly hello from my father and mother, Jean Louis and Gina Baron-Hyppolite, or the daily goofing around with my brother Adrian Baron-Hyppolite and friend Antonio Corbia. Their presence provided a respite from the demands of completing this thesis.

A special mention is needed to my Aunt Charlotte whose support for my father and his family has provided me and my siblings the means to pursue our goals and ambitions without hesitation. Her generosity and support has made it possible for me to undertake one of the most rewarding experience of my life, providing me an opportunity to meet people that have positively influenced me both professionally and personally. Her contribution to this portion of my story will always be remembered.

Summary

The implementation of vegetation in the SWAN standalone model is done one of two ways. Either the vegetation is implemented implicitly through the use of manning roughness coefficients or explicitly through vegetation dissipation method presented in Dalrymple et al., (1984). Throughout literature both methods have been used through various degrees of success, however study such as Smith et al, (2016) and Keefer et al. (2017) have shown that the implicit implementation underestimates the dissipation by the vegetation though neither study has field data to validate this conclusion.

Through the use a field data made available by George Mason University (GMU) an analysis of the East shore Salt marsh is carried to validate the conclusions made in Smith et al, (2016) and Keefer et al, (2017). GMU provided pressure sensor data that is used to create wave spectra for four sensors found across the marsh. They also provide larger meteorological forcing files and bathymetry that allow for the creation of larger scale models. Using this data, a large scale regional model, a domain decomposition model and small-scale marsh model are made and assessed in their ability to first recreate key offshore storms, key flow patterns within the inlet, and the observed wave dissipation over the marsh. These models are made using Delft+SWAN module as well as the SWAN Stand alone.

Through this process it is shown that the models are able to recreate appropriate wave and water level forcing across the marsh though complications occur when attempting to recreate the Nearshore spectrum. The SWAN standalone model can recreate the observed dissipation rates accurately and definitively shows the difference between the two implementation methods, with the implicit method significantly underperforming when compared to the explicit method. The most significant contribution to this disparity in performance being the lack of drag force in the implicit implementation. The performance was also exacerbated by the flow characteristics in the area which indicate an inlet with low sensitivity to bottom friction.

Contents

Introduction

1.1. Motivation

Coastal zones have been the site of massive population growth for decades, leading to large, densely populated urban centers that have dramatically changed coastal environments around the world. This trend of growth shows no sign of slowing down as shown in (Neumann *et al.*, 2015), who suggested that by 2060, under their highest growth conditions the estimated population of major urban coastal areas would increase from 625 million to 949 million by 2030; eventually passing one billion by 2060. The combination of population increase and increase in economic activity has increased the flood risk to coastal cities, resulting in an increase in cost of flood protection in these regions (Hallegatte *et al.*, 2013). In Figure 1, several of the U.S. largest cities (shown by the red dots) are in hurricane strike zones. According to (Hallegatte *et al.*, 2013) three U.S. cities (New Orleans, New York and Miami) made up 31% of the worlds global cost in 2005; showing how costly protecting high value economic regions in coastal environments can be. In response to the cost of flood protection, many institutions have dedicated resources into researching alternative solutions to flooding, giving rise to the nature-based defense approach.
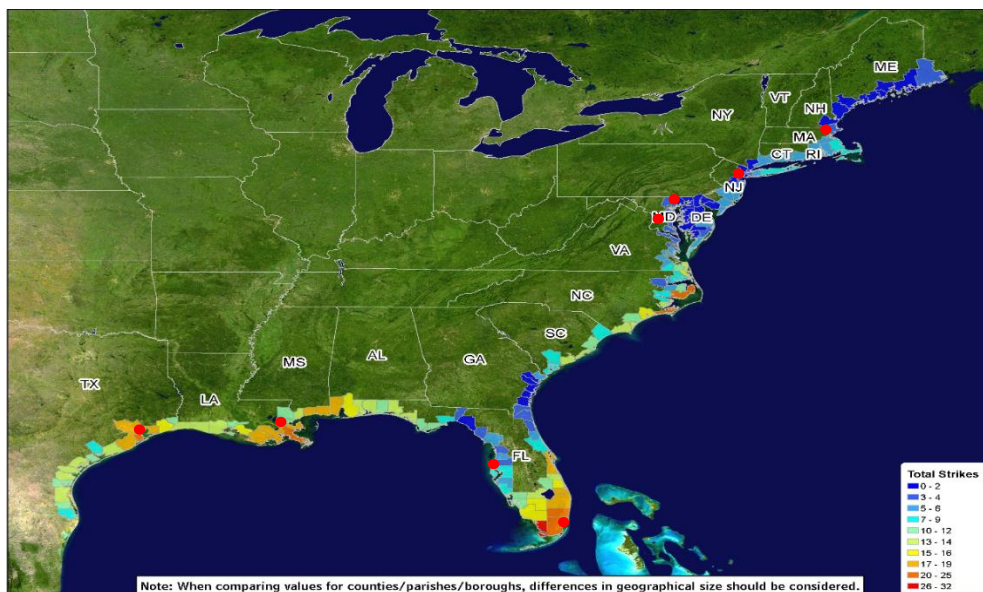
Figure 1 shows the hurricane strike zones on the East and Gulf Coast of the US, with the cities mentioned in (Hallegatte et al., 2013) indicated by red dots. From right to left you have Boston, New York City, Philadelphia, Washington DC, Miami, Tampa, New Orleans

Nature based solutions incorporate natural processes into coastal engineering solutions to minimize the impact that hard coastal engineering has on the surrounding environments. Of the many nature-based solutions saltmarshes and other vegetated foreshores have garnered a lot of interest due to their wave attenuation capabilities. The research began with observations

and studies conducted in the field in the US, UK and regions of Asia. These observations provided field data showing wave attenuation identified in papers such as (Putnam and Johson, (1949); Hasselmann et al, (1973); Dalrymple et al., (1984)) does occur. However, the early field observations attempted to establish a representative dissipation numbers for all vegetated foreshores, which was shown to not be accurate. Later on it was established that vegetation exerted a drag force on the water column reducing the energy of waves and storm surges (Kobayashi, Raichle and Asano, 1993), and that this drag force varies with the height and density (Méndez, Losada and Losada, (1999); Anderson and Smith, (2014)). Dietrich et al., (2011), shows that identical attenuation does not occur across all wetlands. The attenuation rates depend on vegetation, storm, bathymetric and topographic characteristics. Wetlands can also lose their effectiveness in reducing storm surge if the storm is slower causing more prolonged forcing of water surfaces Dietrich *et al.*, (2011). Observations such as this lead to more detailed analysis such as Vuik *et al.*, (2016), which concluded that attenuation can vary based on the water depth and wave heights during storms.

Currently many studies implement the use of numerical models to replicate real world conditions and conduct more detailed assessments of wave propagation in these environments. These models can vary depending on what they simulate and how they simulate, resulting in varied accuracies and uncertainties. Vuik et al (2016), used SWAN to recreate the Hellegat and Bath saltmarshes to help create wave dissipation models needed to relate marsh width, wave height to wave dissipation. Conducting this analysis depends greatly on the ability of the model to properly represent wave dissipation, propagation, and generation. In order to assess model accuracy studies like Keefer et al. (2017) and Smith et al, (2016) need to be conducted. Being that these models are also commonly used to create flood maps and develop flood defenses, assessing their ability is vital to ensuring the effectiveness of hydraulic infrastructure. Keefer et al. (2017), conducted such a study using the ADCIRC+SWAN coupled model to simulate hurricanes in a New Jersey site. The objective of this research was meant to compare the vegetation dissipation representations in the SWAN numerical model. However, the results from the research had no field data to validate. A similar analysis was conducted by McSmith et al, (2016) who validated the results using laboratory experiments. However, because lab experiment is set in controlled environments, it is typically good to have field observations to corroborate results, therefore there is an opportunity to do just that using available field data. The results will reduce uncertainties when using the SWAN model, while providing an opportunity to increase accuracies of existing models.

1.2.   Research objective

George Mason University has provided field data on the East Shore research site in the Chesapeake Bay during storm conditions between September 24th and October 2nd. The data is collected by a set of four field gauges spread across the length of the Salt Marsh. The field data provides an opportunity to assess local and regional hydrodynamic processes impacting wave attenuation on the marsh. It also provides an opportunity to conduct an analysis on wave

dissipation implementations in SWAN and assess the accuracy of the conclusions of Smith et al, (2016) and Keefer et al, (2017). Keefer et al, (2017) concluded that the explicit vegetation representation is more accurate at representing wave dissipation because the implicit manning roughness is meant to represent roughness for a relatively thin water layers. Smith et al, (2016), originally conducted a similar comparison using laboratory data, and came to the same conclusion. Suggesting that further research is needed on this subject to create standard values for different vegetation types like the manning roughness approach. For this reason, the main objective of this paper will be to validate the conclusion that vegetation dissipation approach proposed by Dalrymple et al., (1984) is a more accurate representation of vegetation due to its inclusion of drag force, using the field data provided by George Mason University.

Research Questions

1. To what extent does Delft 3D and SWAN accurately predict wave propagation over shallow foreshores?

2. What Drag coefficients formulation most accurately recreates energy dissiptaion in the explicit vegetation dissipation implementation at the easthshore site ?

3. How are the key physical differences between the implicit manning roughness approach and explicit vegetation dissipation approach shown in the model results?

Research approach

Deep water boundary conditions for the SWAN standalone model are not available however forcing files have been provided for the offshore wave climate in the forms of meteorological files and tide information. Using the coupled Delft3D+SWAN model (Delft Flow, Delft Wave) these wave climates can be simulated creating the boundary conditions necessary for the standalone SWAN model. These Delft 3D models will also allow for larger scale assessment of hydrodynamic processes that will be touched on in the paper. This paper will focus on the process from the generation of waves in a larger Delft 3D regional model to the propagation into the research site where the flow characteristics will impact the influence of bottom friction and drag forcing on the water column. Finally, the SWAN standalone model is created to determine wave energy dissipation and wave height reduction for the two vegetation implementations. Assessment of how these are implemented and what processes they influence will be made to properly explain their differences. From here it is possible to do comparison to results from other sites to see how the east shore site compares to other regions, and how consistent attenuation might be across multiple sites. The model runs are described below.

1. Delft 3D: The Regional model run responsible for recreating key storm events between September 24th and October 2nd, 2015.

2. Delft 3D: The Domain Decomposition model run responsible for simulating the inlet where key flow patterns are identified and described.

3. SWAN standalone: The base model run with no vegetation implemented

4. SWAN standalone: Manning roughness runs for different manning roughness values.

5. SWAN standalone: Vegetation dissipation implementation for different Drag coefficients.

1.3. Report Overview

Chapter 2 Background: This chapter focuses on summarizing important background information beginning with a description of the Models. Then section 2.2 will identify key hydrodynamic process such as wave generation, propagation, wind wave, swell waves, and storm surge. Section 2.3 describes the bottom roughness and how it is implemented in the models. Section 2.4 describes the implicit and explicit vegetation implementations. Each section will contain a subsection describing how the processes are implemented in SWAN or Delft 3D.

Chapter 3 Site Description: This chapter contains the site description as well as a description of the data provided by GMU and the supplementary data collected to fill the gaps. Section 3.1 contains the site description, identifying Sources of major influence such as the large basin to the north of the site that contributes to the ebb tidal flow rate. Section 3.2 describes the GMU data provided and gives a more detailed description of the site wave climate. Section 3.3 describes data taken from offshore buoys and government data bases.

Chapter 4 Methodology: This chapter is separated into four sections describing the creation of the largest Regional model in section 4.1, the domain decomposition in section 4.2 and the SWAN standalone in section 4.3. A description of all assumptions and why they were made is described in these sections as well as a brief description on their analysis in the results section.

Chapter 5 Results: This chapter is broken up like chapter 4, but now describe the results from each model. First it assesses if key hydraulic processes are well captured then it discusses the validation of each model. It then describes the points to be discussed in the following chapter.

Chapter 6 Discussion: Again, separated by model, this section discuss the key points identified in the results section. But also contains sections relating results to other sites 6.4. and limitations section 6.5.

Chapter 7 Conclusion: summarizes the previous section and identifies the next steps that can be taken, building off this work.

2. Background

2.1. Models

Both the Delft 3d and SWAN standalone models are used to conduct the analysis of this paper and therefore require a proper description. This section generally describes both models and the modules that are used for this research. The governing equations are then briefly described along with a description of the governing equations of both models.

Delft 3D

Delft3D is a numerical modeling suite that simulates flow, sediment transports, waves, water quality, morphological developments, and ecology in its own individual modules. These modules can be coupled together to combine the processes when necessary. This paper requires the combination of the delft 3D flow and wave modules to simulate wind forcing, tidal forcing, wave propagation, and surge propagation. The wind forcing, tide and surge are simulated in the flow module while the wave generation and propagation is done by the wave module (Delft 3D uses SWAN in its wave module).

The flow module forms the hydrodynamic basis for several the available delft 3D modules, such as the interaction between waves and currents with the delft3D wave model. It simulates two-dimensional depth averaged or three-dimensional unsteady flow forced by tides, meteorological phenomena, pressure gradients or energy gradients. The flow module derives its governing equations from the Naiver Stokes equations for incompressible fluids. It formulates unsteady shallow water equations, horizontal motion equations, continuity equations and transport equations for conservative constituents.

When coupling the Flow and wave modules, wave current interaction are simulated resulting in changes in set-up, current refraction, bottom friction, forcing, turbulence and bed shear stress (with the first three impacting waves while the last three impacting the currents). The interaction can be computed by using user defined flow variables, offline coupling, and online coupling. User defined variables indicate that the wave conditions are assigned spatially uniform water levels and current velocities. Offline coupling uses flow results from an executed flow model and implements it into the wave model. Online coupling occurs when flow and wave are run in tandem, with the modules passing information between each other.

SWAN

SWAN (Simulating Waves Nearshore) is a third generation Phase Averaged Numerical Model which incorporates empirical expressions for key nearshore processes that allow it to simulate wave propagation from deep water to shallow water. Phase averaged models describe a wave field by its energy spectrum using the energy balance and action balance equations. The use of

the energy spectrum through these equations, allows models such as SWAN to significantly reduce computational time. This shorter computation time makes them more applicable for risk assessment and larger scale studies of coastal regions. However, they do not resolve individual waves making assessment of phenomena, such as bound long waves and other wave-wave interactions difficult to replicate.

SWAN describes waves in a two-dimensional wave action density spectrum in both deep and shallow water, allowing it to predict the second order moment of waves accurately across the complete cross-shore profile. The evolution of the wave spectrum is described by the spectral action balance equation described in Hasselmann *et al.*, (1973) shown in equation 1 below.

$$\frac{\partial}{\partial t}N + \frac{\partial}{\partial x}c_xN + \frac{\partial}{\partial y}c_yN + \frac{\partial}{\partial \sigma}c_\sigma N + \frac{\partial}{\partial \theta}c_\theta N = \frac{S(\sigma,\theta)}{\sigma}$$

equation 1

$$S(\sigma,\theta) = S_{tot} = S_{in} + S_{nl3} + S_{nl4} + S_{ds,w} + S_{ds,b} + S_{ds,dr}$$

equation 2

N represents the action density spectrum, cx and cy are the celerity in the x and y direction, and c_σ and c_θ are the celerity relative to the wave direction and relative frequency. equation 2 shows the input and dissipation variables that will be described later in this section. On the right-hand side of the equation the S represents energy density due to the generation, dissipation, and nonlinear wave-wave interactions. The implementation of these processes into the model are shown in Figure 2 shows the general process in which SWAN goes through to determine the energy spectrum and wave filed componenets.
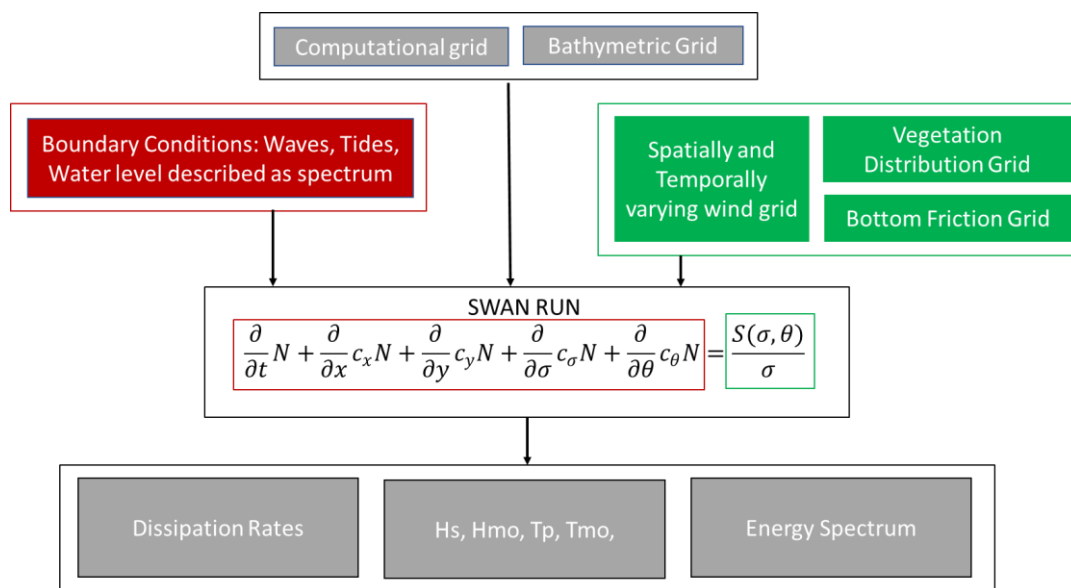
Figure 2 shows the general process in which SWAN goes through to determine the energy spectrum and wave filed componenets.

and are described further in the later sections beginning with the hydrodynamic processes and their representation in the energy spectrum.

2.2. Wave propagation and Energy Profile Evolution

A wave field goes through a complex evolution from its generation source to its complete dissipation or reflection. Modern day numerical models must simulate as much of this process as possible to create accurate results. Therefore, a strong grasp of these processes must be formed before being able to effectively understand how a model replicates these processes. For a SWAN model general knowledge on wave generation, dispersion and propagation must be understood, as well as the wave attenuation process. Details on storm surge will also be described to properly relate these processes to surge simulation.

Wave Generation

Waves can be locally generated short wind waves, long period swell, and short-wave groups that can lead to the formation of bound long waves. There are also much longer period waves such as tidal waves and tsunami waves that are formed by gravitational forcing from the moon and sun (tides) or sudden shifts in bed levels or water levels (tsunamis). For this paper, locally generated waves, swell, tides and storm surge are the most significant processes impacting the project site.

Wind waves are generated by forcing on the water surface from wind originating from storms. The speed of the wind and associated wind drag are very important to producing observed wave climates. Starting with (Wu, 1982), wind drag is proposed to be linearly related to wind speed. Meaning the higher the wind speeds the higher the drag coefficient. However, based on recent observation it was shown that this formulation over estimates drag coefficients. This was clarified in Zijlema et al,(2012), who used observations from a number of storms in the Norths Sea to test the applicability in the Wu drag coefficient model. From this paper is was concluded that as appose to the linear relationship, wind, and drag increased linearly up to 20 m/s wind speed and then plateaus at 31.5 m/s followed by a decrease in drag as the velocity increases past this peak. In appendix A.1 a figure taken from Zijlema et al,(2012) shows the comparison between the Wu derivation and the newly derived relationship.

While waves are generated by the wind and its associated drag force, the characteristic of the wave are also controlled by the fetch, duration of sustained winds, and the celerity of the wave being produced. The relationship between fetch, sustained wind duration and wind speed is shown by the figure generated from Bretschneider et al. (1970) in appendix A.2. In this figure it is shown that larger fetch, wind speed and wind duration result larger wave heights and longer wave periods. This figure also shows that while wave heights and periods are enhanced by fetch or wind speed, they can also be limited. This allows for the prediction possible wave climates to be produced by local storms. Wave celerity also effects how influential storms are on individual waves. If the celerity is higher than the wind speed, then the storm is not able to

influence the wave. However, if celerity is smaller than the wind speed, then energy is transferred between the wind wave interface and the characteristics of the waves are altered.

The complex wave fields developed by these storms propagate in the prevailing wind generation direction at different speeds, or frequencies eventually separating into groups with similar celerity and periods. This process is known as dispersion and is responsible for wave groupiness and the formation of swells. Swell waves have a higher celerity then wind generated short waves, meaning that they reach the shore before the shorter-wave fields. These waves have lower frequency and amplitude and can be found on the 0.1 to 0.04 Hz range of a variance density spectrum (typically the separation between wind and swell wave occurs at 10 second periods). The general accretion is that the longer a wave period the further away its generation point. Once a wave field leaves a generation point its behavior can be altered by bottom friction, wave-wave interactions, pressure variability, and wind forcing. These can all lead to a transfer of energy from one period or frequency band to another. Studies like (Barber and Ursell, 1948) and (Bretschneider, 1952) conducted studies on the decay of wave characteristics over significant distances. Barber et al, (1948) used observations to show that the upper limit of a wave period is generated by the wind, and that wave propagate in dependently of each other depending on their wave characteristics. Bretschneider et al, (1952) showed the decay rate of wave height and period over a significant distance, shedding light on the evolution of waves over large distances. He also indicated the relationship between wind speed and fetch depicted by his diagram in appendix A.2.

Swan implementation

In SWAN, the transfer of wind energy to wave energy is calculated using (Phillips 1957) and is incorporated into the sum of linear and exponential growth terms shown below:

$$S_{in}(\sigma, \theta) = A + BE(\sigma, \theta)$$

equation 3

Where A and B are based on the frequency, wind speed and direction, and are described in (Cavaleri and Rizzoli, 1981), (Pierson and Moskowitz, 1964) and (Tolman, 1992) for A. B is applied in two different ways in SWAN; the first being from WAM cycle 3 discussed in Snyder *et al.*, (1981). The second is rescaled in terms of friction velocity described by Komen et al, (1994). Wind generated waves described above are normally found with periods that range from 1s to 25s or frequencies of 1 to 0.04 s; encompassing capillary, short, long and swell waves. Waves with longer periods begin to fall into the category of infra-gravity waves, surges and tides which can have periods varying from 25s to 12 hrs. Because SWAN describes wave fields by their energy spectrums it has the capability of producing energy spectrum profile that will elaborate on the wave climate experienced in the region. Figure 3 below shows the energy distribution of each category of waves.
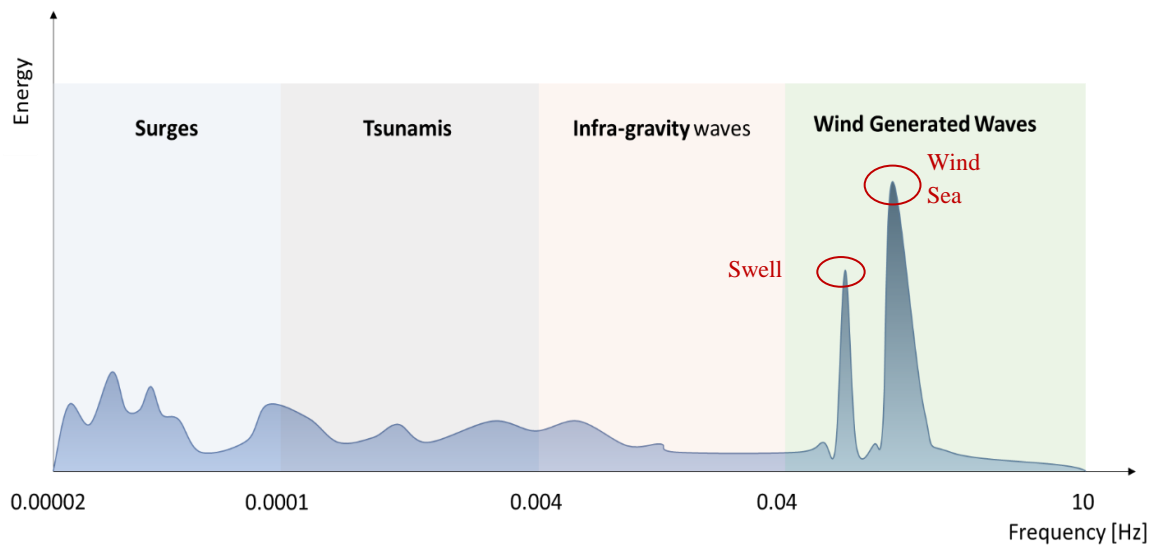
Figure 3 shows the dfferent oceans waves and their associted frequencies.

Storm Surge

Strom surge is caused by a combination of atmospheric pressure difference and wind forcing due to storms. When a storm moves over a region, the low-pressure system causes a rise in mean sea level that can lead to flooding in coastal regions that are not adequately protected. Storm surges typically have a period of a few minutes to a few days, placing them in the category of long gravity waves. The effectiveness of atmospheric pressure and wind at generating surge is dependent on the water depth, atmospheric pressure is more influential in deep water than shallow water. In shallow water storm surge generation is dominated by wind forcing. These relations can be seen in the depth averaged equations of motion and continuity (Murty, Flather and Henry, 1986). There are two simplified relationships that can be formed by simplifying the hydrodynamic equations discussed in appendix A.3. The simplifications for hydrostatic conditions are shown below in equations 4 and 5.

$$\Delta\eta = -\frac{\Delta p}{\varrho g}$$

equation 4

This equation gives a way to determine the change in surge height between two points of varying pressure. From this equation it is assumed that for every 10^2 Pa of pressure difference, a centimeter of mean water level increase is generated. The second relationship gives the balance between the slope of the sea surface due to surge and wind shear. This allows for an estimation of surge as a factor of wind stress, continental shelf width and water depth (Murty, Flather and Henry, 1986).

$$\eta = \frac{\tau_s}{\varrho gh} L$$

<div align="right">**equation 5**</div>

equation 5 implies that as a storm approaches the coast the fetch over the continental shelf "L" decreases reducing the surge height. It also shows that the reduction is depth h, increases the surge height as a storm approaches the coast. Another important factor to consider is the wind shear which, according to (Wamsley *et al.*, 2009) , becomes more of a factor as the storm approaches shallow water. Therefore, from this equation the ratio of shelf length to water depth is important when determining surge height. This ratio would be important when comparing storm surge in open coast to storm surge in estuaries. (Wamsley *et al.*, 2009) also showed that the confinemant of the storm surge is important in terms of water level. If the water has no escape the relation above will most likely breakdown, meaning that surge level will increase. SWAN does not have the ability to simulate surge, instead another model such as ADCIRC or Delft 3D would need to simulate the storm surge. For this research, the storm is simulated using Delft 3D. Storm surge is implemented into delft 3D using the hydrostatic pressure equations under the shallow water assumption. It is dependent on pressure gradients provided by the space varying meteorological files. Pressure gradients dominate external forcing a peak wind speeds during storm events.

2.3. Nearshore processes

The Nearshore processes discussed in this section are vital to the ability of SWAN to replicate wave propagation over shallow water regions and vegetation. They give SWAN the capacity to simulate hydrodynamic processes in estuarine regions. This section will describe wave breaking, bottom friction, and drag forces.

Wave Breaking

The interaction between the bed and the wave lead to shoaling, which is characterized by an increase in the wave crest and a flattening of the trough. The shoaling process can lead to a steepness induced breaking described in (Miche, 1944). He recognized steepness limits in both deep and shallow water that show that wave breaking is partly dependent on the ratio of the wave height and wavelength. This leads to the formulation of breaker indexes which, using the equation 6 below, can be used to determine the maximum wave height or the breaking water depth.

$$H_b = \gamma d_b$$

<div align="right">**equation 6**</div>

Wave breaking is a significant process to consider when assessing the effectiveness of vegetated foreshores. When a wave breaks a significant amount of energy is lost, reducing wave height. This reduction in wave height can lead to a lowering in wave forcing on local flood defenses, reducing flood risk in surrounding areas

In general it is common practice to apply breaker paramteres of 0.8 or 0.73, however brekaer parameters can vary greatly depending on the type of wave climates. (Nelson, 1994) and (Massel, 1996) showed that shallow water environments are better represented by lower breaker indexes. They suggested that breaker indexes as low as 0.55 are more applicable in environments where bed slopes are close to horizantal. The results were validated through both field and laboratory experiments.

Swan implementation

In Swan the wave breaking is implemented using the (Battjes and Janssen, 1978) equation which is expanded to include directional bins. This relationship is shown in equation 7.

$$S_{ds,br}(\sigma, \theta) = \frac{D_{tot}}{E_{tot}} E(\sigma, \theta)$$

equation 7

Dtot is the total dissipation due to breaking and Etot is the total wave energy. The Dtot depend on equation 6, and typically use a default value of 0.73.

Bottom Friction and Roughness

Although the implicit representation of vegetation focuses on adapting bottom friction formulation, both the implicit and explicit representations need to include bottom friction. This addresses the shear stress that the sea bed has on the water column. Over the past couple of decades, bottom friction has gone through several changes and adaptation that has led to the formulations currently used in SWAN.

(Putnam and Johson, 1949) is one of the pioneering papers discussing wave propagation and bed roughness interactions, they created formulas based on the relationship between wave height, friction, and depth. This paper showed that dissipation due to bottom friction is negligible at depth larger than half the deep-water wavelength. Their results also suggested that steep bed slopes have a significantly lower impact on wave height due to bottom friction dissipation than gentle slopes. Longer period waves also seemed to react differently to bottom friction than shorter period waves as shown in Figure below taken from (Putnam and Johson, 1949).

Table 4--<u>Influence of wave period on reduction of wave height by bottom friction</u> (H_0 = 5 ft, k = 0.01, and slope = 1/300)

Distance from point where h ≈ L_0/2	$\frac{H}{H_0} = \frac{\text{Wave height at point x}}{\text{Wave height in deep water}}$		
	Frictionless[a]	T = six sec	T = 12 sec
pct			
0	1.000	1.000	1.000
21.7	0.980	0.978	0.980
43.4	0.935	0.928	0.935
65.2	0.920	0.905	0.916
73.9	0.910	0.887	0.905
87.0	0.925	0.872	0.929
90.0	0.935	0.867	0.950
91.3	0.945	0.868	0.960
93.5	0.965	0.868	0.978
95.7	0.990	0.867	1.003
97.9	1.020	0.856	1.023
100.0	1.060	0.840	1.014

Figure 4 was taken from Putnam et al (1949). It shows the result of the short and long period waves propagating over a uniform bottom friction of 0.01.

Further work has been done on bottom friction, with the focus being on development of roughness coefficients that appropriately describe beach profiles around the world. However, the complexities in this lye in the fact that beaches are not homogenous, making it rare for one roughness coefficient to represent multiple beach profiles (similar can be said for estuarine environments). Much of the early work on bed roughness used the Nikuradse roughness as a starting point but found that it ignored much of the fundamental processes occurring in wave propagation because it was not developed for oscillatory flow and ignored bed forms.

Hasselmann *et al.*, (1973) conducted a large field study as part of the Joint North Sea Wave Project (JONSWAP), to determine the structure of the source function governing the energy balance of wave spectrum with emphasis placed on wave growth under stationary offshore wind conditions and the attenuation of swell in water of finite depth. To do this they assessed the theoretical aspect of multiple processes that could affect spectral energy balance in wave fields, such as non-linear energy transfer due to wave-wave interactions, energy loss due to white-capping, interactions between short and long waves and dissipation due to shallow water. It was found that non-linear energy transfer due to wave-wave interactions result in a minimal amount of dissipation, with bottom interactions being the most responsible for storm surge attenuation. It provided field data that shows dissipation rates of 0.038 m^2/s^3 because of 3D sea bed features, providing a drag of 0.015 for the study area.

(Madsen and Rosengaus, 1988) conducted and experiment on bottom friction using linearized form of the boundary layer equations and an eddy viscosity formulation of shear stress. The turbulent bottom boundary layer flow was determined using the directional spectrum. This allowed the dissipation to be expressed in spectral form with the friction factors determined from Jonsson 1966. The bottom roughness was based from equivalent Nikarudse values and the understanding on how bed forms influence the bed roughness. In these experiments, Grant and Madsen 1976, Stefanick 1979 and Grant and Madsen 1982 were used to describe the

influence of bed forms on the bed roughness. Grant and Madsen 1982 were found to agree with experimental results and was therefore incorporated into equation 8 below to determine k_b.

$$\frac{k_b}{A_{br}} = K \frac{\eta}{A_{br}} \frac{\eta}{\lambda}$$

<div align="right">**equation 8**</div>

Where η is the ripple height and $\frac{\eta}{\lambda}$ is the steepness of the ripple. This value can be incorporated in (Madsen, Poon and Graber, 1988) theory to determine the spectral wave attenuation. Together, these papers showed that spectral dissipation models can accurately describe wave dissipation. However, they did note that this experiment was carried out for a single sediment size and profile, therefore results should on be used as an indicator of potential trends. Many more experiments are needed for different beach profile to determine the validity of these results.

2.4. Vegetation Implementations

Implicit Manning N roughness coefficient

Manning roughness coefficients are bottom roughness values given to surfaces based on bed characteristics such as material, surface irregularities, flood plain cross section, obstructions in the flood plain, and vegetation (Arcement and Schneider, 1989). Each of these contributions are considered in equation 9 below.

$$n = (n_b + n_1 + n_2 + n_3 + n_4)*\text{m}$$

<div align="right">**equation 9**</div>

Selecting an appropriate N value involves good observation, selection of coefficients that most closely represents the point of interest and checking the determined manning value against other locations of similar characteristics. This method does leave some uncertainty in how the factors are selected, since selection depends on whether the engineer believes that the vegetation is tall, medium or short. This uncertainty was somewhat addressed by national land cover data base, which gives coastal regions manning coefficients based that can be used by engineers in the U.S. However, there are still some key interactions that the manning roughness coefficient may not properly represent. Drag coefficient caused by water flowing through marshland can vary vertically or horizontally and impact much more of the water column than the manning bottom roughness coefficient.

Implementation in SWAN

Because the Manning n coefficient is a bottom roughness coefficient, it is not included with the "vegetation" command in the SWAN command file. Instead implementing manning roughness coefficients in SWAN would require the creation of a spatially varying manning coefficient file that can be incorporated into the friction command.

The bottom friction is generally incorporated in SWAN using the (Bertotti and Cavaleri, 1994) formulation shown below.

$$S_{ds,b} = -C_b \frac{\sigma^2}{g^2 sinh^2 kd} E(\sigma, \theta)$$

<div align="right">**equation 10**</div>

Where Cd is the bottom friction coefficient which, in SWAN can be expressed in three different ways, through (Hasselmann *et al.*, 1973), (Collins, 1972) or (Madsen, Poon and Graber, 1988) expression described in section 2.1. Hasselmann et al, (1973) is an empirical formulation of the bottom friction. It uses a constant value to represent the bottom friction, these values typically perform well under most cases and differ for swell and wind generated waves. The (Collins, 1972) interpretation of bottom friction is based on drag law, it uses a nonlinear formulation. (Madsen, Poon and Graber, 1988) is an eddy viscosity formulation for monochromatic waves propagation. It is more complex than the other two formulations because it considers the complex 3D structure found at the bottom. The Madsen formulation is used in concert with Manning n values in order to incorporate manning values into the SWAN formulation. In order to do this the manning n values, need to be converted the Nikarudse friction length Kn, which is done using Bretschneider et al. (1986) shown in equation 11.

$$K_n = Hexp[-(1 + \frac{kH^{\frac{1}{6}}}{n\sqrt{g}})$$

<div align="right">**equation 11**</div>

The Nikarudse variable determined from equation 11 is incorporated into equation 12 to determine the nondimensional friction factor (f_w) which is incorporated in to the Madsen equation for the bottom friction coefficient shown by equation 13 and is incorporated back into the source term (equation 10) to determine the reduction of wave energy as a result of the manning roughness.

$$\frac{1}{4\sqrt{f_w}} + \log \frac{1}{4\sqrt{f_w}} = m_f + \log \frac{a_b}{K_N}$$

<div align="right">**equation 12**</div>

$$C_b = f_w \frac{g}{\sqrt{2}} U_{rms}$$

<div align="right">**equation 13**</div>

Explicit Vegetation Dissipation Approach

The explicit vegetation dissipation approach represents vegetation as stiff cylinders of a given diameter and height. These representations depend greatly on the drag imposed by vegetation which itself can vary due to several factors. This section will describe the research that has

been done in the past couple of decades about drag coefficients for vegetation. It will also be followed by a brief description of its representation in SWAN.

Dissipation by Drag forces

Wave propagation through vegetated field is dependent on multiple vegetation characteristics, such as vegetation height, density, and brittleness. All these contribute to the drag force that the vegetation can exert on the wave. Vegetation can also contribute to an effective depth, which means that waves feels the bed earlier resulting in breaking further away from shore. These features, combined with bed roughness, exert a lot of influence on wave propagation. (Kobayashi, Raichle and Asano, 1993) formulated a 2D problem of small amplitude waves propagating over a submerged kelp field using linearized momentum equations. (Dalrymple *et al.*, 1984) formulated a parabolic model for calculating the combined refraction and diffraction of monochromatic linear waves. This model lead to the creation of equation 14 below which gives a damping rate "w" that is a factor of numerous damping process such as bottom friction or drag force.

$$w = \frac{2n\sigma\alpha}{k}$$

<div align="right">**equation 14**</div>

$$\alpha = \frac{2C_D}{3\pi} \frac{D}{b} \frac{a_0}{b} (sinh^3 k + 3 sinh ks) \left(\frac{4k}{3 sinh kh (sinh 2kh + 2kh)} \right)$$

<div align="right">**equation 15**</div>

Incorporation of drag force was expressed as α and is a factor of the drag coefficient C_D and vegetation characteristics such as vegetation height s and spacing b. (Dalrymple *et al.*, 1984) also showed that the damping caused by drag effects the energy of the wave through conservation of energy equation (equation 16 shown below). This shows that dissipation is a factor of drag forces exerted by the water column on the vegetation. Dalrymple assumed the vegetation to be stiff vertical cylinders in the water column.

$$\frac{\partial E c_g}{\partial x} = -\epsilon_D = F_D u$$

<div align="right">**equation 16**</div>

Using the results from (Dalrymple *et al.*, 1984); Kobayashi, Raichle and Asano, 1993) assumed that the effects of vegetation were expressible through drag forces, and were able to obtain an analytical solution for small amplitude wave propagation over a vegetated field. This solution showed that vegetation does exert influence of local waves and was compared with a kelp experiments which showed that conservation of energy equation and linear wave theory are both appropriate to use to represent wave attenuation by vegetation.

The understanding of wave attenuation by vegetation was further explored by (Méndez, Losada and Losada, 1999) who created a model to test the hydrodynamics over submerged and emerged vegetation for both regular and irregular wave fields. This study is significant because up until this point most research had been focused on monochromatic wave propagation over submerged vegetation. Mendez and Losada also considered vegetation motion as appose to Dalrymple and Kobayashi who assumed stiff vegetation. The drag coefficients for rigid and swaying vegetation were taken from Kobayashi et al (1993). The C_D values were determined as a function of Reynolds number (which determine the flow characteristics over vegetation i.e. turbulent or laminar). Rigid vegetation had higher drag coefficients ranging from 0.09 to 1.55. The swaying drag coefficients had lower drag coefficients, ranging from 0.33 to 6.9. (Méndez, Losada and Losada, 1999) show several conclusions from their study.

1. The taller the vegetation the higher the dissipation.

2. The larger the depth the smaller the dissipation,

3. The denser the field the higher the dissipation.

4. Dissipation, due to increase density reaches a peak once the vegetation field is so dense that it behave more like a step.

5. Drag force along a wave along the field is not constant.

Building on Mendez and Losada (Anderson and Smith, 2014) continued the assessment of vegetation characteristics confirming the results on vegetation height but also determining that wave attenuation seemed to be more dependent on stem density and the ratio of vegetation height to water depth (the relationship was confirmed by (Vuik *et al.*, 2016). They also found that attenuation rate increases with wave height, which makes sense if considering the breaker index discussed in the breaking section. It was also determined that there was a favoritism to attenuation of high frequency waves as appose to low frequency wave.

Implementation in SWAN

$$S_{ds,veg} = \sqrt{\frac{2}{\pi}} g^2 \tilde{C}_D b_v N_v \left(\frac{\bar{k}}{\bar{\sigma}}\right)^3 \frac{sinh^3 + 3\sinh \tilde{k}ah}{3kcosh^3\tilde{k}h} \sqrt{E_{tot}} E(\sigma, \theta)$$

equation 17

SWAN has been equipped with the ability to simulated wave energy dissipation due to vegetation induced drag. This is done by using the cylinder approach described by Dalrymple *et al.*, (1984), in which the vegetation is represented as stiff vertical cylinders with the drag coefficient values (C_D) as the main calibration parameter. The Dalrymple vegetation dissipation expression as altered by (Mendez and Losada, 2004) to incorporate spectral properties into the equation. Mendes and Losada expressed the dissipation due to vegetation as total dissipation (D_{tot}) which is already incorporated into the breaking wave dissipation

formulation shown above equation 17. Allowing for the creation of the expression below, which shows the change in energy spectrum due to vegetation dissipation as represented in SWAN. SWAN also allows for dissipation to vary horizontally and vertically, to represent vegetation fields more appropriately. This is done by summing the dissipation rate of each horizontal or vertical movement and is represented in Figure 5 above (Team, 2017a).
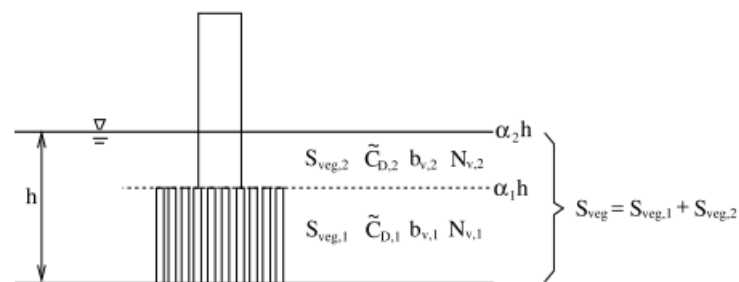
**Figure 5** Shows a representation of how vegetation is represented in SWAN (Team, 2017a)

3. Site and Data description

The following chapter will focus on the description of the East Shore Project site, the site data provided by GMU and the outside data collected to create the delft 3D and SWAN models. Section one describes the project site and key feature that influence the propagation of waves towards the site. Section two describes the data provided by GMU, giving a general description and a brief description of their interpretation. The third section covers external data collected from government websites and other internet sources that were vital to building and validating the model. This section will provide a clear overall picture of the site and the data used to answer the main research question.

3.1. Project Site
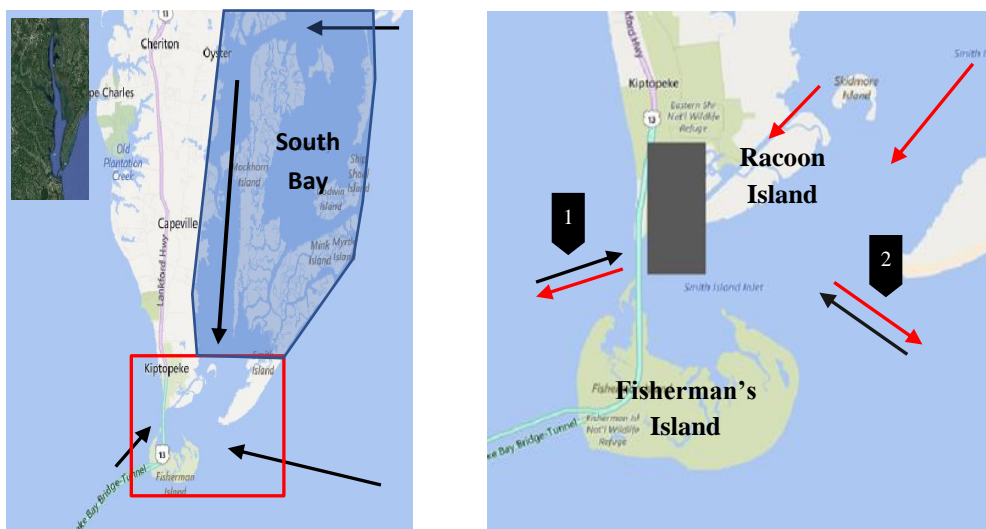
Figure 6 depicts the research site along with key contributions from wave and water level flow directions. Important features are also labeled such as the South Bay due to their influence of the flow at the research site.

The Chesapeake Bay is the largest Estuarine ecosystem in the United States stretching about two hundred miles north. This bay consists of a relatively deep main channel bordered by marshland, small towns and two large cities. At the mouth of the Chesapeake Bay another smaller bay called the South Bay can be seen (accented in blue to the right of Figure 6. Unlike the Chesapeake Bay, this bay is dominated by marshland and is bordered by a system of barrier islands. Between the mouths of these two bays is the East-Shore Project site, which is shown on the right of Figure 6 by the gray box in the right image. There are two main inlets that contribute to the hydrodynamic forcing at the site, indicated by the numbers one and two in Figure 6. Wave forcing penetrates through these two inlets generated from the Atlantic by

offshore storms, which can vary from seasonal storms to category four hurricanes. Therefore, the wave climate oscillates between swell and locally generated wind waves, however the relatively shallow bathymetry prevents waves above two meters from penetrating to the site unless a sufficient surge is present. Inlet two transitions from a depth of about seven to two meters over a length of two thousand meters, giving it a very gentle slope of 0.2 percent. Inlet one has a gentle slope 0f 0.6 percent, transitioning from a depth of seven to one meter over one thousand meters. The shallowness of this area is the result of being located at the termination point of multiple sediment pathways. The first of these pathways come from the longshore sediment transport along the barriers island. The second of these pathways comes from the mouth of the southern basin. The sediment pathways result from the general north-northeast direction of the wave climate produced by the winds generated by the north to south pressure difference.

The East-Shore site experiences a diurnal tide cycle, meaning that there are two high and low water events per day. The tidal range between these periods vary from one meter to half a meter. With the most landward portion of the site being around a meter above mean sea level, the site is only partially inundated during high spring tide and is completely out of the water during low spring tide. During the transition from ebb to flood, waves are able to penetrate both inlets resulting in a east and west wave direction, depositing sediment into the research area. During the transition from flood to ebb the dominant flow from the research site enters from the mouth of the South Bay indicated by the red lines in the right image of Figure 6. The flow continues around racoon island and exits through inlet number one, into the main channel of the Chesapeake Bay.

The project site is covered by Spartina Alterniflora, a saltmarsh plant found commonly along the east coast of the united states. The area also consists of deciduous coastal forest, coastal shrubland and coastal grassland all indicated in later chapters. These all contribute to the flood climates impacting the surrounding community.

3.2. GMU Data Description
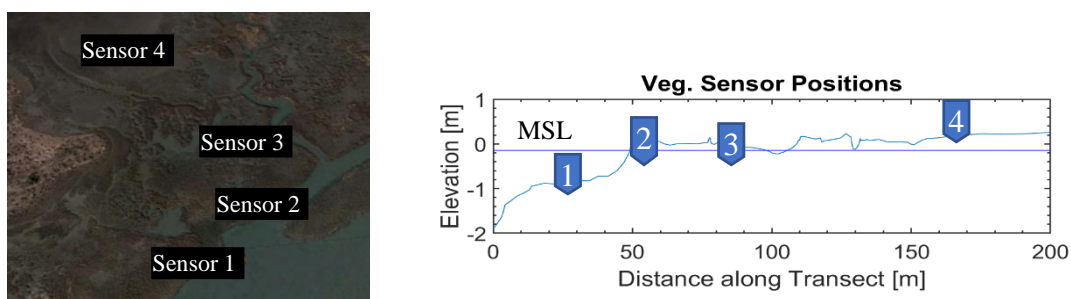
Figure 7 shows the sensor elevation as well as their position of the marsh site. The Marsh sit is indicated by the black box in the picture on the right in figure 6.

Two sets of data are used in the making of the Delft3D and SWAN models, the first being the GMU data which provides detail on the wave and wind data in the area. The wave data was taken using trublue pressure gauges set at varied levels on the bed. George Mason University also provided a significant amount of information on vegetation characteristics and bathymetry. Figure 7 shows the position of the sensor on a transect crossing the study site. The second set of data includes bathymetric data, tide data, land cover data and wave buoy data retrieved from the NOAA website and the US geological survey website. All the field data is provided in NAVD88 vertical datum which is converted to MSL (Mean Sea Level) by the process discussed in appendix A.5. The marsh elevation varies form -0.72 meters to 0.4 meters about the mean sea level.

GMU General Wave climate
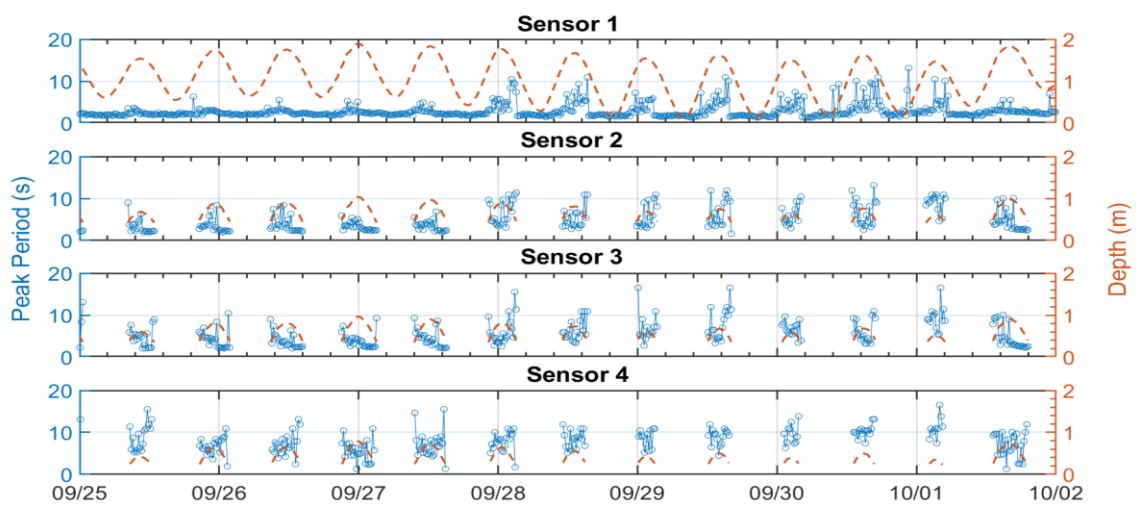
Figure 8 shows the peak period, and water depth for each sensor, with the depth indicated ed in orange while the peak period is indicated in blue.

Indicated by Figure 8, the sensors showed a range of periods varying from 2 seconds to 10 seconds, with a majority of the wave climate energy residing within the two to six second period range (Appendix D shows the wave spectra determined from the model as well as the field data). This indicates a dominance of locally generated wind wave in the region. The depth measurements at sensor two, three and four show gaps in the data. These are the results of both dry points and water levels that are too low for the sensor to accurately provide relevant data. The periods shown above indicate a transition of periods from short to long periods. The energy transitions from short wind waves to longer swell waves.

Significant Wave Height

	Peak Hm0	Mean Hm0	Reduction	Dis. Beginning of Transect
S1	0.42	0.2271	0 %	29 m
S2	0.2792	0.1679	34 %	54 m
S3	0.1478	0.0780	65 %	84 m
S4	0.0599	0.0298	87 %	168 m
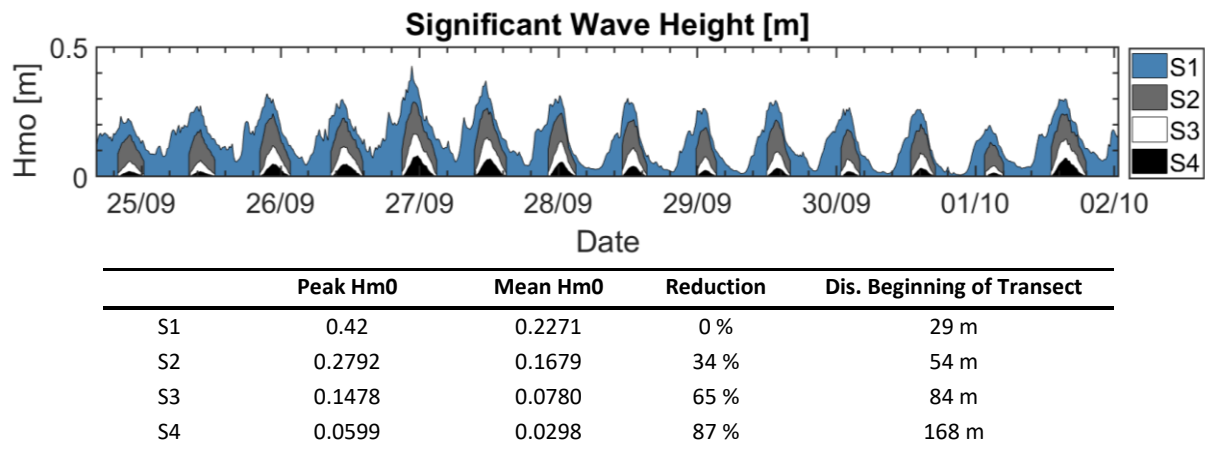
Figure 9 show the wave data recorded by all sensors relative to each other. Below is a table describing wave height and dissipation rates**.**

The significant wave height shown in Figure 9 were determined by the zero moment of the field data's spectral profile. The peak wave height occurs on September 27th with a magnitude of 0.42 meters then reduces gradually as the wave propagates across the foreshore. Figure 9 indicates all wave heights during the time of interest from sensor one to sensor four. A clear dissipation is observed, as well as the dry points that were observed in the depth in Figure 8. In this section the dry points are present in sensors two to four and are represented by gaps in the data.

GMU Water Level data
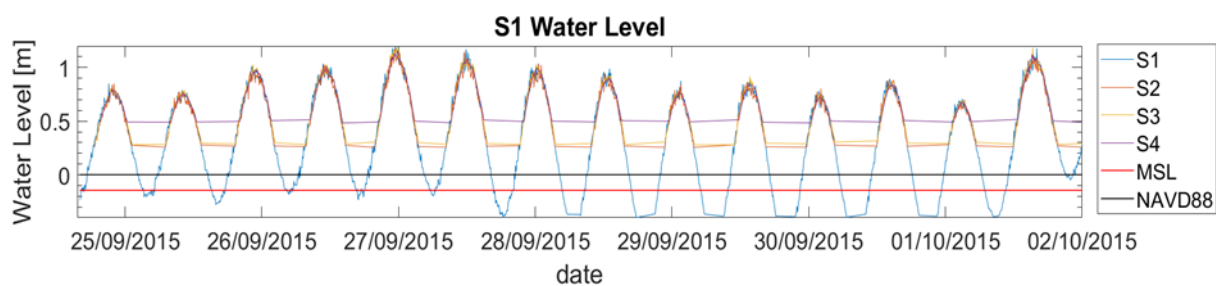
Sensor	Peak Water Level	Mean Water Level	Percent Change	Max Depth	Mean Depth
S1	1.4632	0.1943	0	2.209	0.9401
S2	1.46	0.5081	0.0022	1.352	0.4044
S3	1.5352	0.4762	-0.049	1.482	0.4762
S4	1.437	0.686	0.018	1.194	0.4443

Figure 10 shows an image indicating water levels along the transect for each sensor as well as the MSL and NAVD88 vertical datums. The Water level table below provides more detailed information on the water level data

The water level data was also extracted from the spectral analysis conducted on the pressure gauge data. It shows an increase in water level that corresponds with the two storms discussed in previous chapters. Peaks in water level for each sensor are shown in Figure 10 along with a figure showing its oscillation about the NAVD88 vertical datum. The data reveals a relatively constant water level from sensor 1 to sensor 4, with very small variations in the results. The water level will impact the influence that the bottom friction or roughness will have on the water column, with higher water levels result in less depth induced and bottom friction induced dissipation.

GMU DEM bathymetry

The bathymetry provided by GMU was created through a combination of surveys of the research site and incorporation of the Virginia Beach Digital elevation model to include the surrounding bathymetry. The Virginia Beach Digital elevation model is typically used for tsunami studies but provides detailed bathymetry with a 10 to 30-meter resolution. It uses the WGS 84 horizontal datum and Mean High water as its vertical datum which was converted to accommodate the NAVD88 vertical datum used in the survey. Together the bathymetry provided information on a 4 by 6-kilometer area at a resolution of 5 meters. The transitions between vertical datums are conducted using data from the NOAA website which is described in appendix A.5. For implementation into the SWAN and delft 3D models, this data was converted into xyz and bot files, the formats of which are described in appendix B.
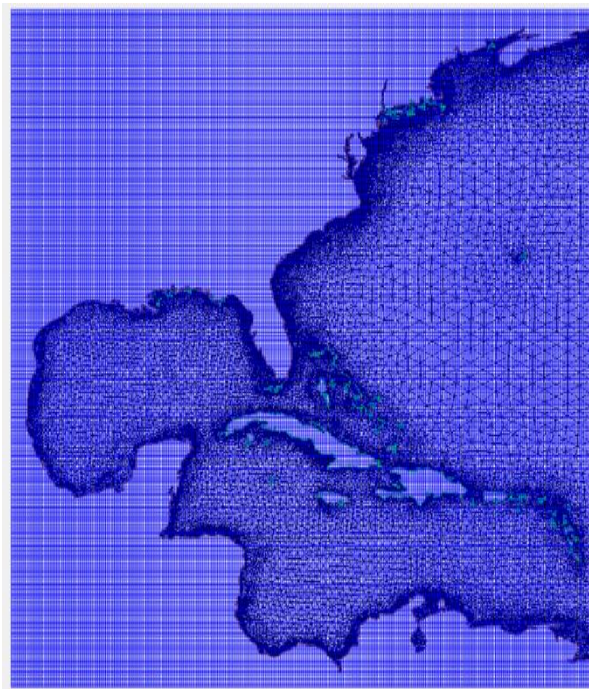
Figure 11 fort.22 extent is shown above, with the model detail shown in the table below.

Fort.22

The Fort.22 file is aa ADCIRC file that describes the wind conditions of a region for a given period. The Fort.22 file provided to us by GMU comes from a study done by them on weather forecasting systems. Using the Meteorological file from six different forecasting systems they create an ADCIRC+SWAN model of the Chesapeake Bay for hurricane Joaquin, Irene, Sandy, and a severe winter storm. From this study it was determined that the ECMWF (European center for medium range weather forecast) file provided the most accurate data for wind speeds and water levels, with the highest correlation occurring at the mouth of the bay where it reached over 95% correlation to station data (Garzon, 2018).

This file can only be read by ADCIRC or SMS and therefore also needs to be converted to an appropriate format. This data is large and coarse and will therefore not be used in SWAN stand

alone, however this will be used in Delft3D to determine the boundary conditions at the site. For this, it is converted to three equidistant grids that contain the x component of the wind, the y component of the wind and the pressure changes over the entire region. The format for this file will also be discussed in the appendix B.

3.3.   Other Data

Bathymetry

Along with the SWAN model, a larger regional model is made to determine the boundary conditions. The bathymetry provided by GMU does not extend to the deep or intermediate water. Because of this, two other data sets will be used for the regional simulation. The first will be GEBCO bathymetry for the largest region stretching into the Atlantic Ocean. This data set is constructed using data provided by many countries all over the world. However, it does have its limitations, to begin its resolution is 900 meters meaning that it is relatively course and should not be used for nearshore calculations. However, for deep water conditions this is fine because the bathymetry has little influence over wave propagation. This bathymetry uses the WGS84 as its coordinate system, which is spherical coordinate system (longitude and latitude). Because of its wealth of data sources, the vertical datum used for this data is MSL (mean sea level). While not as important in the deep ocean, at nearshore conditions this datum is defined using local mean sea levels, meaning that MSL in one location may not be equal to MSL at another. For nearshore conditions the Virginia Beach Digital Elevation Model describe in the GMU bathymetry section was found and extended to encompass the south bay and offshore regions.

Buoy Data
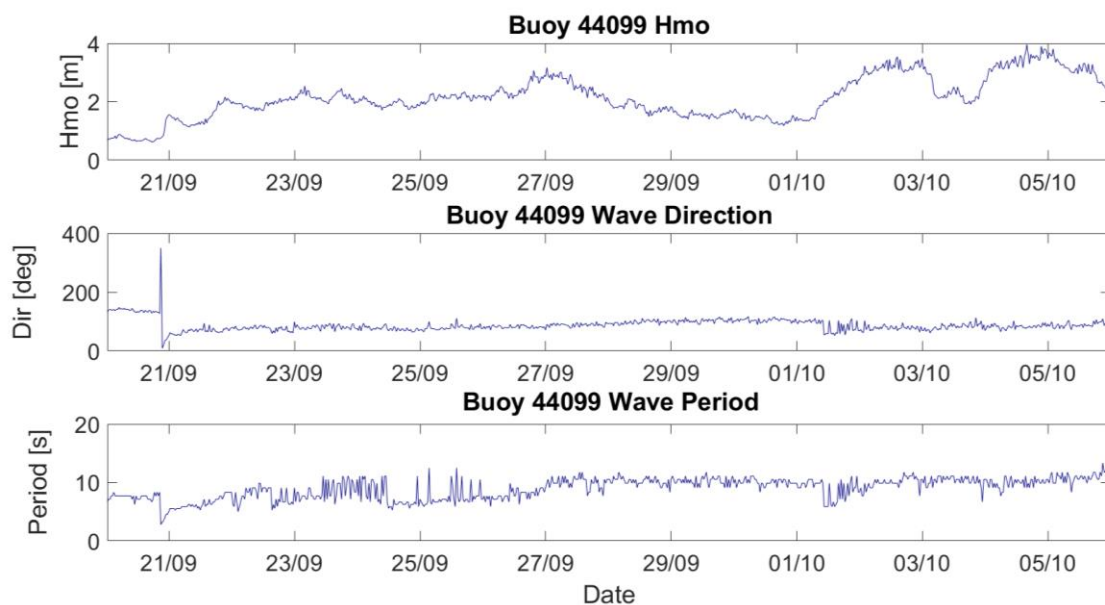
Figure 12 shows the buoy for an offshore site that is used to validate the largest scale regional model. This shows the significant wave height, dominant wave direction and dominant wave period.

The buoy data provided by the NOAA website is used to validate the result of the initial large-scale model used to create the boundary conditions at the site. These buoys provide significant wave height, peak wave period, average wave period, water level and wave direction. The results of the validation will be discussed in the methodology section of the paper. Figure 12 above shows the wave data provided by buoy 44099, the closest buoy to the project site. The data was taken over a period of 15 days, starting on September 20th, 2015 and lasting until October 6th, 2015.

The field data indicates wave conditions that are being influenced strongly by local wind generated waves and swell waves that are partially produced by both hurricane Joaquin and a storm to the north which will be shown later. The ability for the model to simulate these conditions depends on the accuracy of the wind files, the bathymetry and bottom friction. Along with these wave buoys there are water level monitoring stations in the area that provide data for validation of the flow regional model. Together these buoys will validate the regional model that is used to produce the boundary conditions necessary for the stand-alone SWAN model. The locations of these buoys are shown in Figure 13 below, with the tide stations shown on the left and the wave buoys on the right.
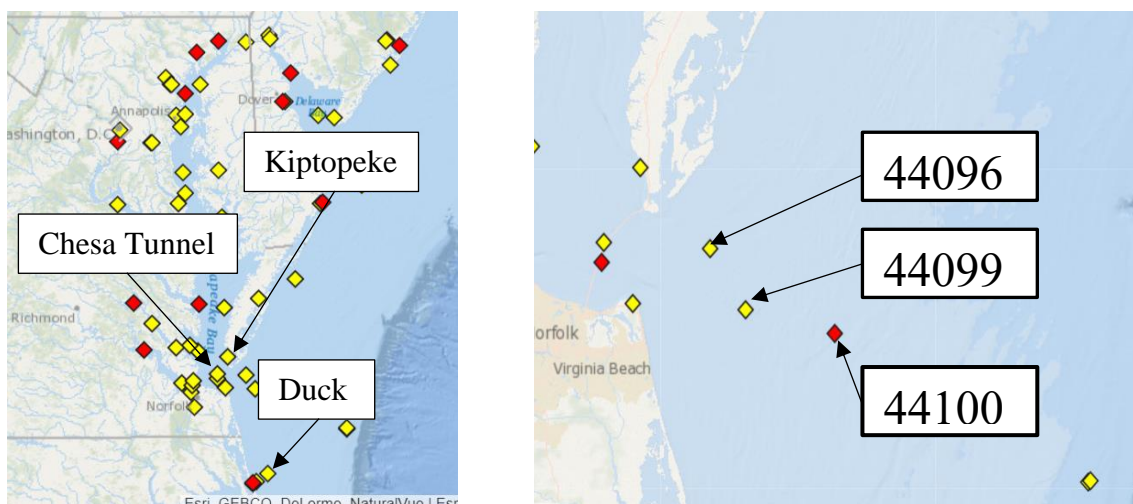
Figure 13 shows buoy positions on the right and tide stations on the left that are used to validate the results of the largest regional Delft 3D model. Buoy 44099 is the buoy shown in figure 6.

4. Methodology

4.1. Approach

To run the SWAN standalone model several data files need to be put together. These include the computational grids, bathymetric grids, landcover files, wind files, and boundary condition files. Most of these can be extracted by the files provided by GMU, however the boundary files need to be produced from existing data or models. For this paper, the boundary conditions are produced by Delft Dashboard and Delft 3D numerical models. This means that two separate models are created, the SWAN model for the main analysis and the larger regional model to produce the boundary conditions. The regional model has its domain decomposed to properly simulate nearshore processes.

The process will include gathering data necessary for the regional model, which includes wind data covering all significant storm events that effect the project site. Next the bathymetry would need to meet the same conditions, limiting the choices in bathymetry to GEBCO. Tidal information will also need to be provided for the boundary conditions of the larger model, to properly simulate water level.

The resulting regional model encompasses a large portion of the Atlantic Ocean and is forced by the wind conditions and tidal boundary conditions. This model propagates wave conditions to the site but needs to be refined to extract the boundary conditions at the site. To achieve this, a domain decomposition is done of this larger model. The domain decomposition refines the grid to the point where all important bathymetric features are included; this requires more refined bathymetric data. A combination of the Virgina Beach tsunami digital elevation model and DEM data will be implemented for the smaller grids. From this model, two dimensional spectral files are produced and implemented into SWAN for the final model run.

The SWAN model uses these boundary conditions along with the landcover data to simulate the propagation of waves over the foreshore. From these results the implicit and explicit vegetation representation are compared allowing for the identification of the more appropriate representation.

The following section will describe the creation of these models, describing the selection of boundary conditions, their extents, and the choices behind key physical parameters. It will begin by first describing the large scale regional model, then the domain decomposition and finally the SWAN model.

4.2. Regional Model (large scale)

Wind conditions

As discussed in chapter 3.2 the wind conditions for this larger scale regional model were determined using a fort.22 file produced by the ECMFW model. This provided wind velocity and pressure change information over a very large region, encompassing both the Atlantic Ocean and the gulf coast. Due to the sites location the domain was reduced to only include the Atlantic Ocean. From this domain, the buoy data and pressure data were used to identify the key storms in the region. This includes two northernly storm from September 20th to September 30th and hurricane Joaquin from September 26th to October 6th. The three storms are shown in Figure 14 below with the left showing two pressure depressions in the center of the domain. These depressions create wind blowing from north-northeast, creating a front that coincides with the first peak shown in buoy 44099. The wind speed currently reaches a max of 16.11 m/s. The second storm shown in Figure 14 at the top right is driven by transition from
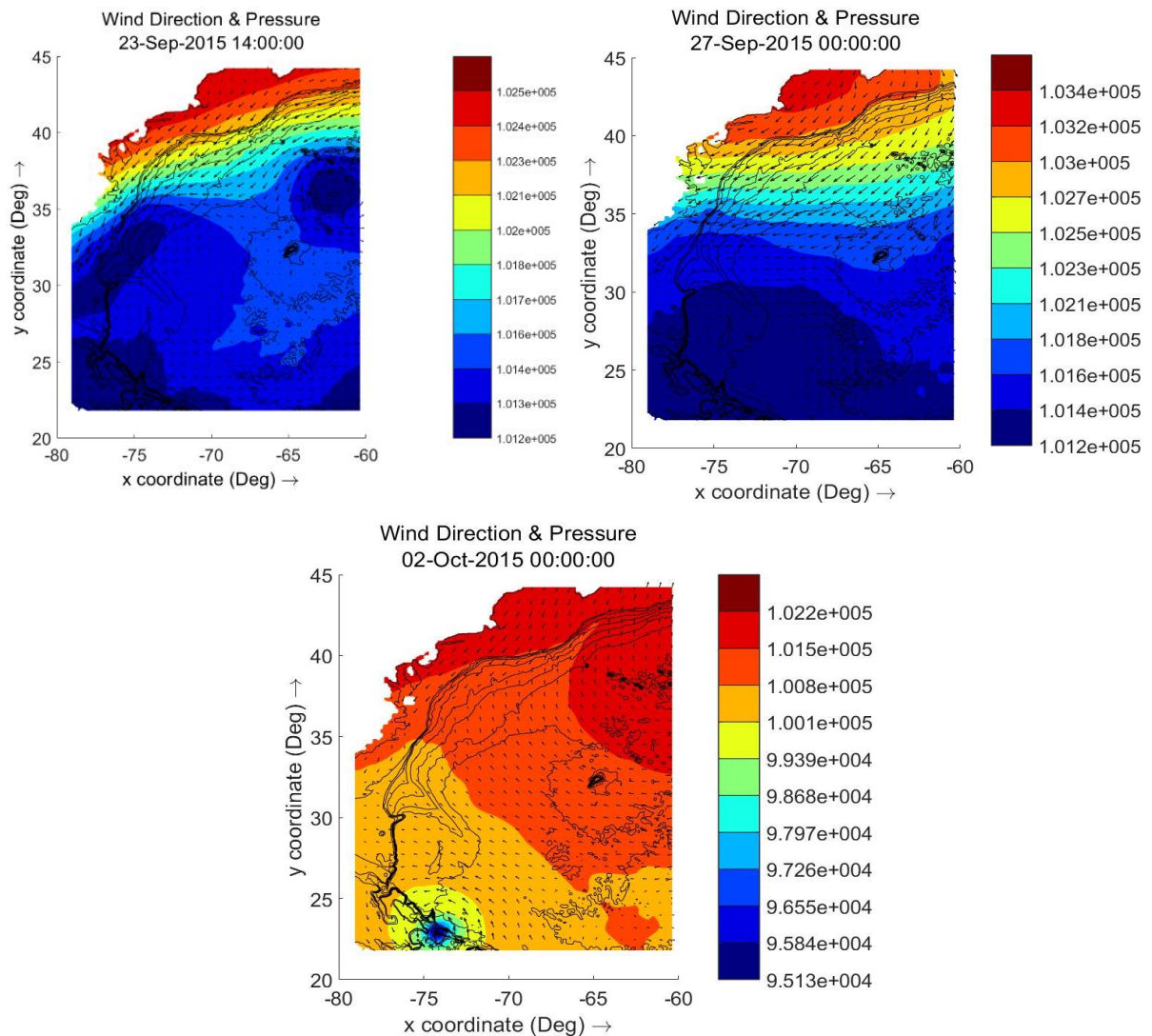
Figure 14 shows the storm and wind direction for three key storm events that occurs in the large regional model domain. They coincide with peak wave heights in the buoy data.

high to low pressure that crosses the Atlantic. This creates an east-northeast wind that blows at a max of 13.24 m/s over a large fetch. The third storm shows Hurricane Joaquin reaching category four near the Bahamas. The hurricane produces winds that reached up to 40 m/s during the time shown below, however its distance from the site makes wind speed less important until the swell produced by the hurricane reaches the site. The presence of the hurricane does alter the surrounding pressure field producing another north-northeast wind front near the site. From this information the extent of the boundary is chosen, to encompass all these points of interest creating a computational grid that is 200 by 250 grid cells at 0.075 degrees resolution. This means 50,000 grid cells that are 8.75 km long and 8.75 km wide.

Bathymetry

For the bathymetry the GEBCO data was chosen, as previously suggested in chapter 3.2. due to the size of the region the model must simulate, there are few data sets that encompass the region. The GEBCO data is implemented through delft dashboard and can reach a resolution of 900 meters. The results using this bathymetry are validated up to deep water to intermediate conditions using the buoy data.

Boundary Conditions

Boundaries indicate the point in the domain where the external world influences the region inside the domain. A boundary can either be open or closed, where open boundaries are associated with water to water interfaces such as the open ocean and closed boundaries refer to water-land interfaces such as river banks or coastlines. Open boundaries allow the movement of wave climates across their border. They can apply water level, tidal, transport, flow and wave forcing to a domain, however their application must be done with care to avoid inaccuracies or instabilities within the domain. The regional model has boundaries set in the open ocean, with the wave climate being generated predominantly by winds, air pressure and tides. The winds are found within the domain therefore the open boundaries in this model will be tide boundaries applied through astronomical forcing files.

To determine the most appropriate boundary type for the regional model, both Reimann and Water level boundaries are tested. The results of this comparison are shown in Figure 15, with setup one indicating water level boundaries applied on all sides. Setup two indicating a combination of water level applied on the eastern boundary and Reimann applied on the north, south and west boundaries. Setup three representing a domain with all Reimann boundaries. The water level boundaries were chosen because the tidal forcing applies water level and velocity information to the domain. The Reimann boundaries were chosen because of their weakly reflective nature, allowing for the instabilities caused by the hurricane being near the domain extent to be reduced.

The forcing of this model will come primarily from wind, and tides. With the wind file addressed all that is left to describe is the tide data. Delft dashboard provides several tidal data bases. For this model the TPXO 7.2 is used.
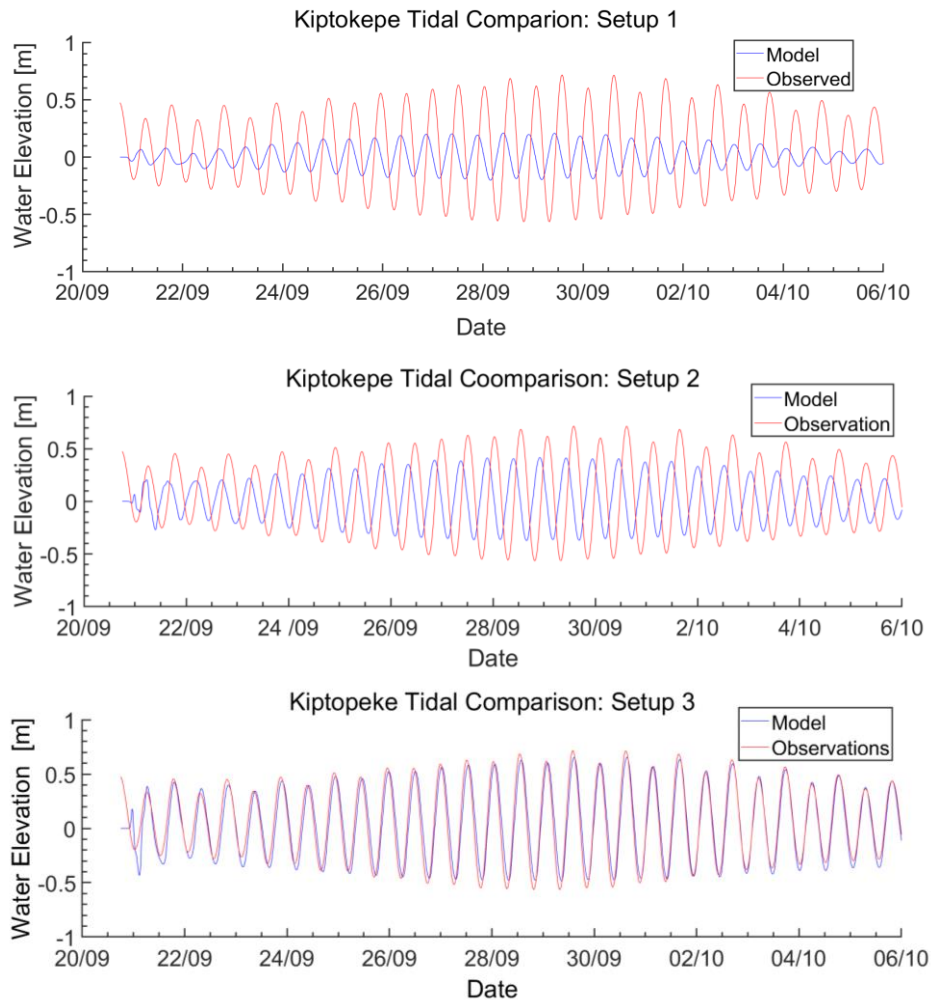
Figure 15 shows the comparison between tides calculated for the three different boundary condition setups. Setup 1 showing only water level boundaries, followed by setup 2 which indicated the combination of water level and Reimann boundaries and setup 3 indicating all Reimann boundaries.

TPXO7.2 is a series of fully global models of ocean tides, which best fit, in the least square sense the Laplace Tidal Equations and altimetry data. This data is consistently updated based on new bathymetry and tidal information, increasing its efficiency for every new version. The accuracy of this model has been compared to CSR4.0, GOT99.2b, NAO.99b, FES2004, TPXO7.1 and DDW99 in Kim *et al.*, (2011), where it provided the most accurate representation of oceanic tidal forcing. This data is implemented in both the Reimann and water level boundaries.

Between the setups, the Reimann boundary conditions simulate the tides much better than the water level boundary conditions for this model. Both the Reimann and water level boundaries input the tidal information described above as astronomical forcing files. The files apply tides

in the form of their astronomical components, which include the main semi diurnal tidal components (S2, M2, K2 and N2), the Diurnal tidal components (K1,O1 and P1,) and the long period components (MF, MM, and SSA). The key difference between these boundary types are how they handle reflection. The water level boundaries handle reflection through alpha values which dampen the tides as they approach the boundary. However high alpha values also lead to tide that are out of phase. For this model the alpha value was set to 10,000 which caused a phase shift in setup one and two shown in Figure 15. This alpha value did not do much to reduce the reflection at the boundaries resulting in the smaller tidal range predicted by the model shown in blue as compared to the station data shown in red. Setup two shows that the inclusion of the Riemann boundary greatly reduced the reflection in the model, however the presence of the water level boundary still causes inaccuracies. Therefore, setup three with only Reiman boundaries applied is the most appropriate setup among the three.

Reimann boundary conditions were formulated in the work of Verboom et al, (1984) using weakly reflective boundary condition described in Engquist et al, (1977). Assuming zero flow along the boundary condition allows the Riemann invariants to be determined. These invariants are two waves moving in the opposite direction and are a function of water level (ς), velocity in the normal direction (U), and the depth (d). These Reimann invariants are represented by equation 18 shown below (Team, 2017b).

$$F_R(t) = U + 2\sqrt{gd} + \varsigma\sqrt{\frac{g}{d}}$$

equation 18

Reimann boundary conditions are weakly reflective boundaries typically to waves that are normal to the boundary but also reduce the reflection of oblique waves.

Other Physical Parameters

Validation v. Regional Model Constants		
Variables	**Validation model**	**Regional Model**
Domain Size	268 x 140	250 x 300
Resolution	0.2 - 0.05	0.075
Time Steps	5 min - 10 min	12 sec
Bottom Roughness (Flow)	0.02	0.02
Bottom Roughness (Wave)		0.038
Surface roughness		0.001, 0.0025, 0.003
Boundary	Reimann	Reimann

Table 1 shows the physical parameters recommended by the validation model and the parameters chosen for the regional model.

Creation of the model begins with Delft Dashboard validation case Nederhoff et al, (2014). The information from this report is used as a starting point for selecting appropriate physical and general model parameters. The Nederhoff et al, (2014) report conducts two model tests in the Gulf of Mexico that asses the ability of the Delft 3D model to replicate water levels using the available data sets. Only the first of these two models are used as a reference in this paper. This model is tidally forced, using the GEBCO global bathymetry and the TPXO7.2 tidal models. The boundary conditions are weakly reflective Reimann boundaries. The settings for the base setup are shown in table 1 along with the settings chosen for the regional model.

From this Nederhoff et al, (2014) it was determined that the grid should be about 1.5 time the area of interest to properly get all key processes involved in the model. Smaller than this and the semidiurnal constituents are not completely reproduced, larger and the diurnal constituents are over estimated. Due the wind forcing that needs to be applied to the model, the domain needs to be made much larger than the study site.

Nederhoff et al, (2014) showed that an increase in grid resolution increases accuracy by 12% percent, when refining the grid from 1/5 degrees to 1/20 degrees (0.2-0.05). The resolution chosen for this paper's regional model is set to 1/20 (8.25 km), which is half the resolution of the wind file. Given that most of the domain is located to in deep water, the resolution is not altered relative to the GEBCO bathymetry. The regional model domain is indicated in Figure 16 along with domain decomposition discussed in the following section.
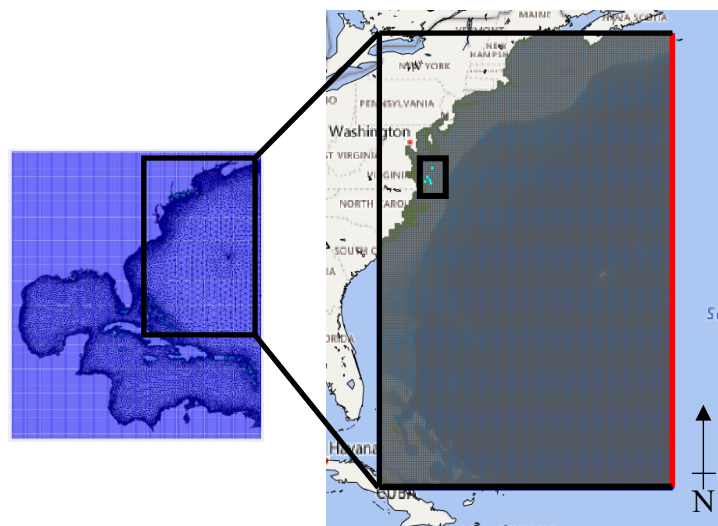
Figure 16 shows the regional model domain with the boundary changed in setup 2 discussed in the boundary conditions section shown in red. The smaller domain decomposition is also indicated by the smaller rectangle within the domain. This domain is cut from the wind file shown on the left.

Time steps influence the ability to simulate the phenomenon desired. Stable accuracy was determined in Nederhoff et al, (2014) at 5 to 10 minutes steps, so this is where the model testing began. However, the validation case was testing tides while the regional model test waves as

well. The time step of 12 seconds was chosen based on the maximum period observed by the buoy data for the regional model.

The validation model only used one bottom roughness because it was only testing the tidal simulation of the model. It used the default of 0.02 for a manning roughness coefficient, which typically represents the bottom roughness for sandy sea beds. The Regional model simulates both wave and tide, meaning that the flow and wave module will be used. Flow module describes bottom roughness through manning roughness values. The default value is 0.02, which represents the expected roughness of sand, as discussed in Chow et al, (1959). Because the model will mostly represent the offshore sea bed, the default 0.02 value was kept. The Wave model uses the JONSWAP bottom friction determined in (Hasselmann *et al.*, 1973), who determined that for swell climates 0.038 is an appropriate representation of the bottom friction. However the wave climate in this area is not only dominated by swell waves, locally generated wind waves also dominate in this region. (Bouws *et al.*, 1983) observed that 0.067 is more applicable for wind-sea climates, an observation which has been used in many papers to represent wave climates dominated by locally generated wind waves. The roughness is found through calibration and discussed further in the domain decomposition section.

In the flow model wind drag can be assigned break points where the roughness value changes. The validation case provides no guidelines for this, the delft 3D flow manual shows that surface roughness will reach a peak at a certain wind velocity and then decreases. This is corroborated by Powell et al. (2003) and (Zijlema, van Vledder and Holthuijsen, 2012), which showed a logarithmic relationship with surface drag and wind speed. However, Zijlema et al, (2012) used the 0.038 JONSWAP coefficient because the 0.067 overestimated the dissipation rate. SWAN uses the Wu relationship to describe the wind drag coefficient which uses a linear distribution to describe drag coefficient growth. This relationship does use the larger JONSWAP roughness coefficient as well. The storm wind velocities are also below 20 m/s which is the point at which the drag coefficients transition from the linear growth to the logarithmic growth. Therefore, for the wind drag coefficient, the Wu relationship equation 19 was used to assign drag coefficients at 0m/s, 7.5 m/s and 20 m/s.

$$C_D(U_{10}) = \begin{cases} 0.0012875 \\ (0.8+0.065*U_{10})*10^{-3} \end{cases}$$

<div align="right">**equation 19**</div>

Where the value of 0.001285 is used when U10, the wind velocity 10 meters above the ground is lower than to 7.5 m/s. The formula in the second row is used when U10 is greater than or equal to 7.5 m/s.

Analysis

The results of this model are validated using three offshore buoys with wave height, direction and peak period data. Along with this validation, a qualitative assessment of the key storms

discussed in chapter 3 will be done. Relating them to their modeled wave height, and their relation to the results.

4.3. Domain Decomposition model

Domain decomposition is the process of incorporating fine computational grids into larger coarse grids. This is often done for sites where smaller scale changes in bathymetry can greatly affect the wave climate. Using a course grid may mean overlooking areas of significant importance, that will effectively reduce the accuracy of the model. The regional model described in the previous section uses GEBCO data which is appropriate for deep water calculations but runs into problems when applied nearshore. The GEBCO bathymetry is created using data from numerous other countries, meaning that its datum is set in mean sea level, which can vary locally. Due to these problems using this bathymetry nearshore to acquire boundary conditions would not result in an accurate model. The coarseness of the regional model also needs to be refined to accurately represent the project site. The regional model currently has a resolution of 0.075 degrees or 8 kilometers, which is way to course. The SWAN standalone computational grid has a resolution of 5 meters, the domain decomposition will need to refine the grid close to this resolution while keeping the run time of the model at a reasonable length. To transition from 8 kilometers to around 10 meters, the regional model was broken down into five grids, with three of those five transitioning from GEBCO bathymetry to the Virginia Beach Digital elevation model bathymetry and eventually the DEM bathymetry provided by GMU. The transition between these bathymetries will be discussed in the following sections.

Bathymetry and Domain

Domains	Bathymetry	Size	Resolution [deg]	Resolution [m]	Indicator
Region	GEBCO	250 x 300	0.075	8250	
1	GEBCO	42 x 32	0.015	1650	
2	Virginia Beach DEM	87 x 82	0.003	330	
3	Virginia Beach DEM+DEM	117 x 107	0.0006	66	
4	DEM	92 x 157	0.00012	13	
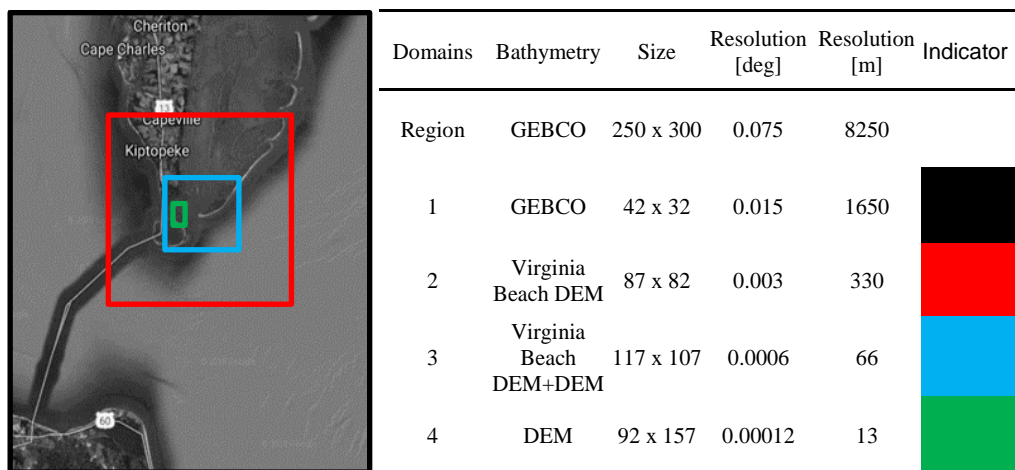
Figure 17 shows extent of the domain decomposition grids. The extent of gird 1 is equal to the extent of the image, the extent of the proceeding grids matches the color provide in the table on the right. The regional grid is the regional model which is not shown in this image but was shown in previous chapters.

The grid resolutions are reduced by increments of five, any larger and the model may run into instabilities. The decomposition starts at deeper to intermediate water, to address any

differences in water depth between the Virginia Beach DEM and GEBCO data. This difference in water depth is partially due to the different vertical datums and the coarseness of the GEBCO data. The decomposition then continues until it reaches the smallest domain surrounding the boundary points of the SWAN standalone model. The Grid sizes and resolution along with a map of their placement is shown below.

The bathymetry for the inner most grids were combined with the GMU data because the GMU data most closely resembles reality. Conversions from NAVD88 and MHW to MSL is necessary to ensure the appropriate combination of the regional model and the domain decomposition. From the NOAA it was determined that MHW (mean high water) is 1.26 meters from (MSL) mean sea level and that NAVD88 is 0.145 meters. After the conversion, the domains are checked to ensure that the key feature line up, smoothing out and adjusting any obvious differences which may influence the project site.

Other physical parameters

The forcing of the domain decomposition model is identical to the forcing applied in the regional. It uses a combination of wind and tidal forcing to generate appropriate waves and water levels. The forcing for wind drag is kept as the Wu relation, the manning values for the regional model and domain one are kept at 0.02, however domains three, four and five use a manning roughness coefficient of 1.5 to represent the combination of sand and mud found in the regions. From literature the roughness and breaker parameter vary greatly for nearshore regions, making these values ideal for calibration of the model. The bottom roughness uses a JONSWAP coefficient, which varies from 0.038 for swell climates to 0.067 for wind sea. This is used as the calibration range for the models, bottom frictions of 0.038, 0.05, 0.06 and 0.067 are applied. The breaker parameter is implemented using the bore base model of (Battjes and Janssen, 1976). The calibration range for breaker parameters is determined using the equation below which can be applied to the GMU data.

$$H_{max} = \gamma d$$

equation 20

Where H_{max} is the maximum wave height (0.42 m) and d is the depth (1.19 m). Using these values, a γ of 0.32 is determined as the lower threshold of the breaker range. The values that are tested are 0.73 which is the default, 0.65, 0.6, 0.5 and 0.4.

Analysis

The results of this model will also be checked qualitatively to determine whether the wave propagation and flow are behaving as expected. This will be validated by the comparison with the GMU data for wave height and water level. The spectral profile will also be checked to assess how well the model is able to recreate the energy profile.

4.4. SWAN Standalone Model

The SWAN model is the primary source of analysis for the project site because of its ability to simulate nearshore processes including dissipation by vegetation and bottom friction. The SWAN model can use landcover files to represent areas of varied stress on the water column. The implicit manning roughness coefficient will be applied by separating different land classification into manning values. The explicit vegetation dissipation approach uses the landcover data to indicate where vegetation characteristics, such as height and density, are applied. Using this information in combination with the boundary conditions determined by the coupled Delft 3D flow and wave model, dissipation rates are compared to the field data to identify the more appropriate vegetation dissipation representation. The setup of the SWAN model follows the same set up as the domain decomposed model, excluding the numerous domains. Instead a single domain uses the boundary conditions produced by the domain decomposition model and the same physical parameters to simulate wave propagation of vegetation.

Boundary conditions
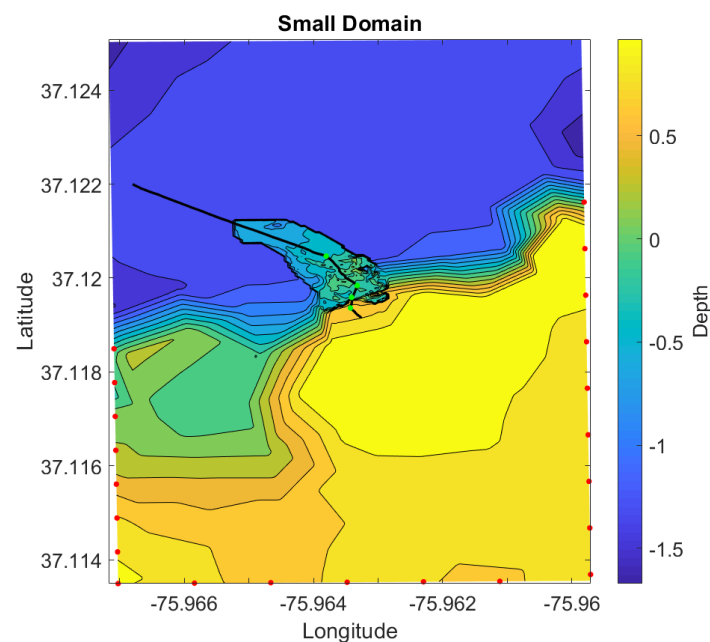
Figure 18 shows the small domain with the points selected for the boundary conditions (red) and the sensor location (green). The depth in this domain is about the Mean Sea level vertical datum.

The area of the decomposed domain model was selected based on the locations of the observation points needed to record the SWAN standalone boundary conditions. These boundary conditions were chosen based on bathymetric features, such as spits or berms in the water. These will interfere with forcing if applied to close and can result in abnormalities. It was also determined to be important to ensure a single point represents an area of relatively smooth depth with no sudden changes. Figure 18 shows the bathymetry and the boundary points chosen for the model (red points along the outside). These are assigned the spectral

profile from the domain decomposed model in.sp2 format (discussed in the SWAN user manual), which provides the energy density as a factor of frequency and direction. The sensor locations are also shown in green at the center of the image, resting on the black line that indicates the transect that will be studied in detail.

Information of vegetation characteristics was provided by GMU. The vegetation data was collected along the transect and contains two types of vegetation Spartina Alterniflora and Spartina Patens. Spartina patens is located to the rear of the marshland and is therefore ignored. Figure 19 shows the characteristics of Spartina Alterniflora across the width of the marshland. For the Standalone model the GMU determined the vegetation plant height during the study period should be set to 0.71 meters, with a stem diameter of 5.21 millimeters and a vegetation density of 334 stems per square meter. These values are the average of the vegetation characteristics shown in Figure 19 and are indicated by the red lines on the graph. These values will be used to assess appropriate drag coefficients of the research site for the explicit vegetation dissipation representation.
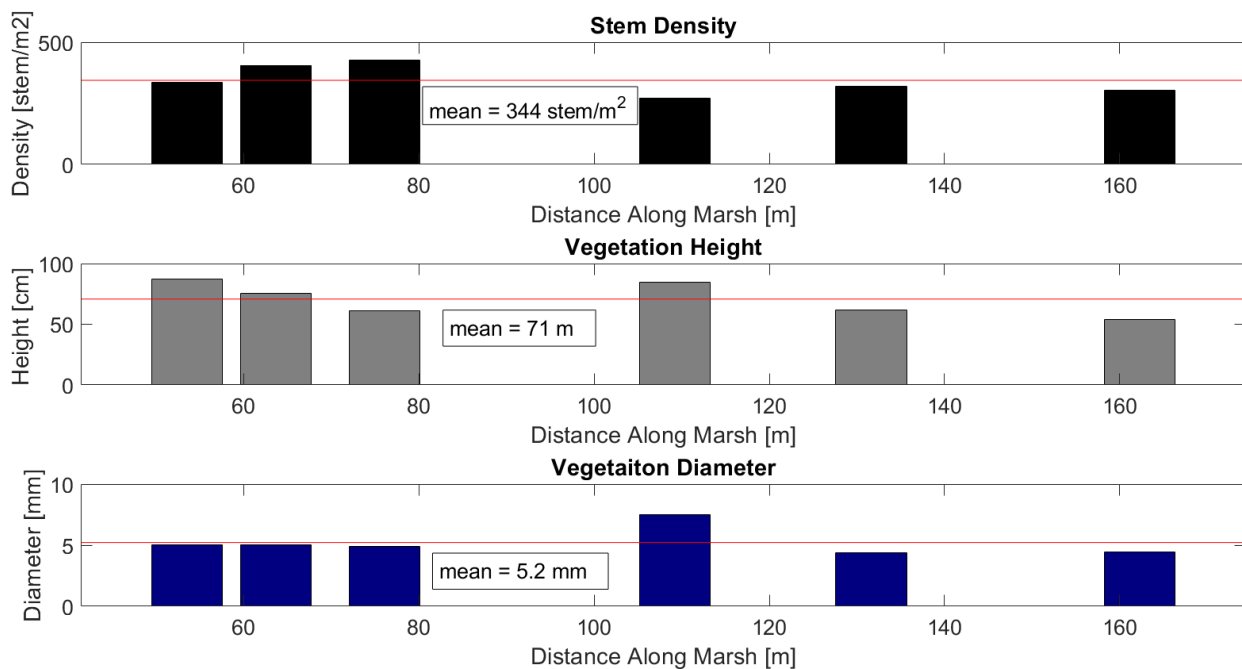
Figure 19 vegetation characteristics data provided by GMU along the Marshland.

Vegetation Drag Coefficient

The selection of the drag coefficient is based on three formulations, the first of which is the (Méndez, Losada and Losada, 1999) formulation showed inequation 21. This was determined through laboratory experiments using flexible plastic strips to represent the vegetation.

$$C_D = \frac{2200^{2.2}}{Re} + 0.08$$

equation 21

Landcover Classes	Manning Values
Deciduous Flood Plain	0.14
Grassland	0.07
Shrubland	0.06
Brackish Marsh	0.045
Salt Marsh	0.035
Ocean	0.02

Table 2 shows the manning coefficients for each provided by Bunya et al,(2010) for different vegetation classes**.**
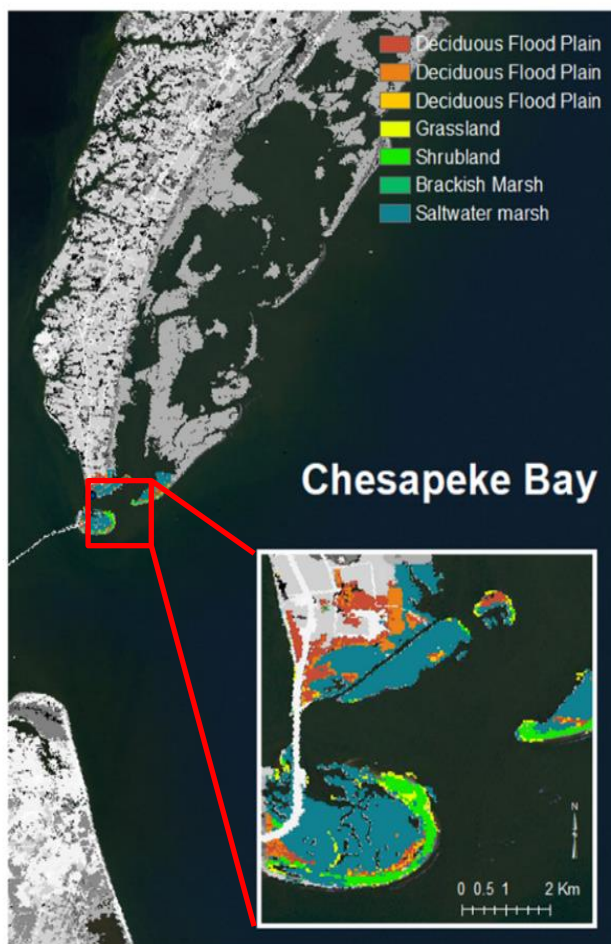

Figure 20 shows the vegetation classification distribution throughout the research site. The table above indicates the associated roughness values used in Bunya et al. 2010**.**

The other two formulations were determined for spartina alterniflora plants, the first presented in (Jadhav and Chen, 2012) determined from field observations taken during a tropical cyclone (equation 22).

$$C_D = \frac{2600}{Re} + 0.36$$

equation 22

The final formulation is determined using the drag relation discussed in (Anderson and Smith, 2014), who used synthetic Spartina Alterniflora in a lab experiment to produce equation 23.

$$C_D = \frac{744^{1.27}}{Re} + 0.76$$

equation 23

Re in these equations represent the Reynolds number determined as a function of velocity, stem diameter, viscosity, and density. Since the vegetation species is constant throughout most of the marsh, the diameter does not change much, however the velocity is strongly dependent of the wave climate. The current velocity during the period of interest vary from 0.1 m/s to 0.7 m/s giving a range of Reynolds number from 430 to 5000. Using this Drag coefficients are chosen for different time periods.

Manning Roughness values

Manning values are taken from Bunya *et al.*,(2010), who used the manning roughness coefficient associated with Louisiana Gap land cover data sets. The Louisiana site contains similar vegetation species as the project site. The manning roughness applied here is also a general value applied to vegetation types that share similar characteristics, such as saline marshland who are all assigned the same value of 0.035.

Vegetation Implementation

The implementation of the vegetation characteristics and manning roughness is done using land cover files. These files describe area with vegetation and without, assigning vegetated sites a value of one and none vegetated sites a value of zero. In the case of the manning coefficient multiple land cover classes are identified using Virginia GAP land cover data provided by the USGS. This data set separates landcover all over the U.S into classes, each with their own characteristics. Bunya *et al.*,(2010) used these classes to assign the manning roughness values to their vegetation. Using the Virginia GAP landcover data I am able to make Figure 20. The are several vegetation classifications shown in this figure, however the site is dominated by salt marsh, shown in blue. Due to its location saltmarsh is expected to dominate the area. The GAP data is also used for the vegetation dissipation file, where the salt marsh is chosen as the only land cover class of interest, the rest is ignored.

In SWAN these files are incorporated using the vegetation, nplant and friction commands. The vegetation command indicates that characteristics are being described. The nplant command indicates that vegetation landcover files are bring imported. The manning roughness values are incorporated using the Madsen bottom friction formulation, since manning is a bottom roughness coefficient that has had its values increased to replicate dissipation by vegetation.

Water level and Wind

The Delft 3D model provides both water levels and wind data to the SWAN standalone model. The water levels are incorporated as spatially varying grids provided by the Delft 3D flow module. The wind data is extracted from the meteorological file and is implemented as a constant value across the entire grid. Due to the relative coarseness of the Wind data, any small local fluctuations in wind might be overlooked.

Analysis

This model is used to assess the implementation of vegetation and will therefore consist of multiple runs to assess drag forcing, and manning bottom roughness. The three drag force formulations described above will be compared for their ability to recreate the dissipation conditions. From this the most optimal drag formulation is chosen to conduct the final validation of the SWAN standalone model for explicit vegetation representation.

The manning roughness will incorporate the Bunya et al. 2010 values discussed above. Different values, such as the one representing vegetation brackish marshland and intermediate marshland is applied to see their impact on the accuracy of the model. The two representations will be assessed on their ability to recreate the wave heights and spectral profiles. The results are also qualitatively assessed to ensure what is observed follow general expectations of the marsh.

5. Results

The results section is separated into three sections for each model. The sections first asses the model ability to recreate key hydrodynamic characteristics, such as the storms for the large regional model or the tidal flow for the domain decomposition model. Then the validation is shown., indicating points of error and areas of discussion for the next chapter. The SWAN standalone portion is separated between the manning implementation and the vegetation implementation.

5.1. Regional Model

For the Delft 3D regional model, it is important that all storms of significance are completely resolved between September 20th and October 3rd. This model is validated using significant wave height, wave direction, water level and peak period. Figure 21 shows the results of the model for three time periods discussed in chapter 3 (regional model). In chapter 3 it was shown that the wind blows predominantly from north to south, except for the Oct 2nd storm profile which shows that the pressure depression caused by the hurricane causes a change in east-southeast wind to blow, creating a front near the sites indicated by green diamond. The wind velocity for the September 23rd storm reaches a peak of about 15 m/s, with and north-northeast peak wind direction. The winds are strongest over the site, generating wave of 2.5 meters near the site. The September 27th storm produces wind up to 18 m/s blowing in the east-northeast direction. This higher wind speeds are not in the path of the site, meaning their impact on the
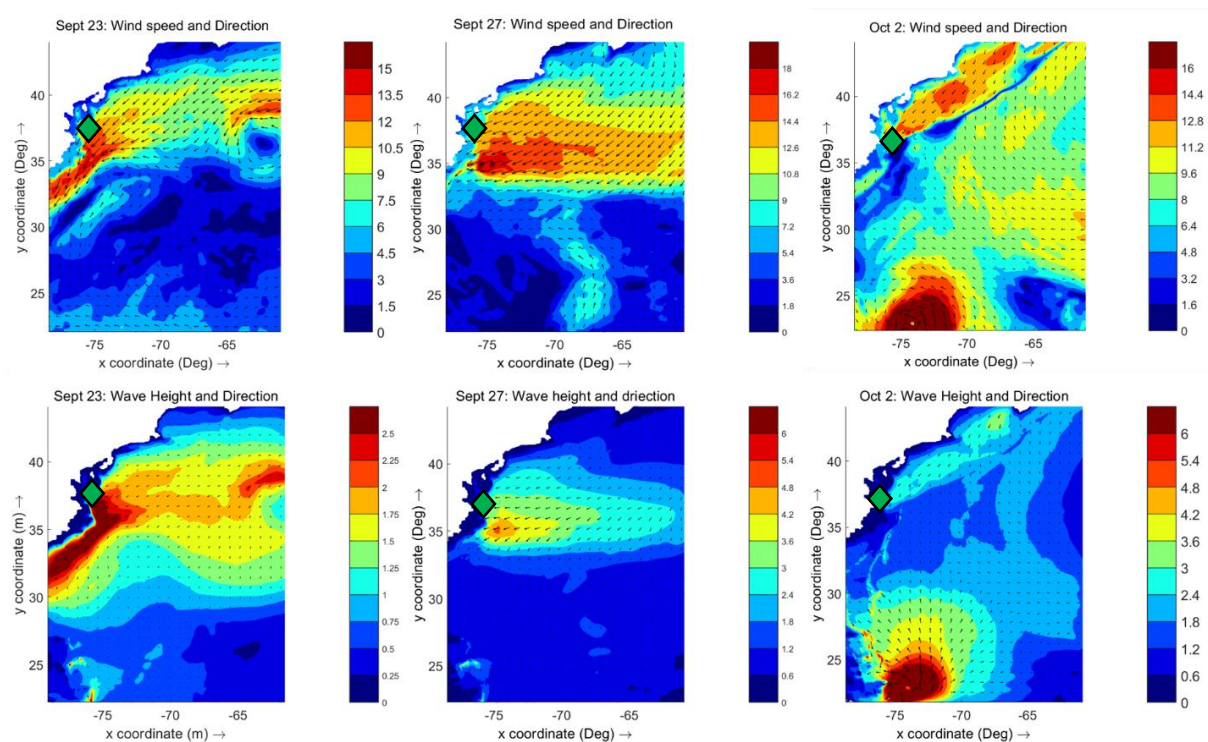
Figure 21 shows the results of the Delft 3D regional model, comparing the wind velocities (top) to the significant wave heights (bottom).

site is minimal instead a large wind field of 15 m/s wind encompasses the site is most likely responsible for the resulting wave climate. This storm generates significant wave heights of 3.6 m near the site. The October 2nd storm occurs because of a front produced by the interaction between the wind field caused by hurricane Joaquin and a northern pressure depression. The winds from this storm reached speed of 16 m/s and produce significant wave heights of 3.5 meters near the site.

Validation

The Following section shows the regional model results and they're in comparison to the NOAA buoy data, for wave heights, periods and water levels. The correlation and error between each variable is briefly described in this section but are shown in appendix

Significant Wave Height

The regional model was compared to three buoys in the area, each with a significant wave height, a wave direction and peak wave period. Figure 22 shows the results of the significant wave height comparison. The trends between the model and buoys are captured well for the significant wave height, each giving a correlation of around 80%. The table shows the correlation and normalized root mean square error (ME). The largest error occurred at buoy 44100 with a value of 16 %. The underestimation of the wave heights may be caused by several variables, in delft 3D this can be caused by breaker parameters, bottom friction and wind drag. The buoys are all located in water of 15 to 25 meters depth. With wav height of 3 to 4 meters it is unlikely that these waves are depth limited. Bottom friction is also unlikely to be the leading cause of the underestimation for the wave. However, in the flow module the water levels showed to be slightly sensitive to the manning bottom roughness. A high manning roughness can cause a model to be too dissipative resulting inaccurate water levels which can
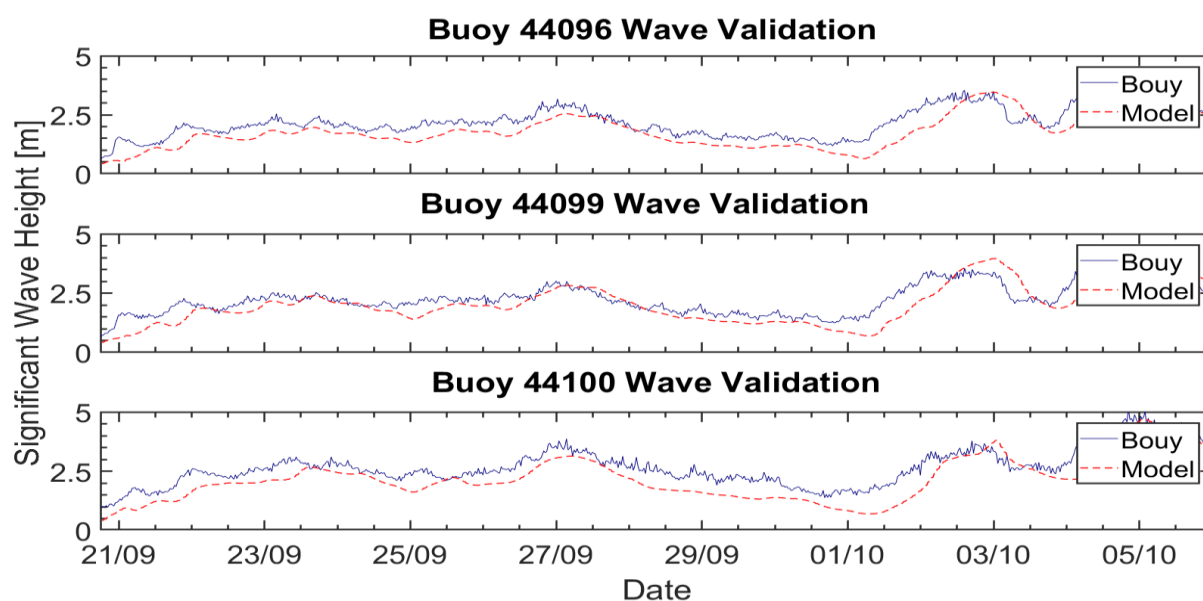

Figure 22 is the significant wave comparison between the NOAA buoy data and the Delft 3D model. The model is shown in red and the buoy data is shown in blue.

impact the wave heights. However, as previously stated the water depth large making depth induced breaking unlikely in this region. Wind drag, along with sustained wind duration and fetch all influence wave generation and propagation. The wind speeds for all the local storms are all below 20 m/s meaning that a linear relationship is valid, but the under estimation may indicate a drag coefficient that is too low. However, for the Domain decomposition model, the correlation and error are reasonable enough to move on.

Wave Direction

The Figure 23 shows the comparison between the wave direction determined by the model and the buoys. The direction for both is recorded using the nautical convention with the angle between north and the x axis being equal to zero. The nautical convention means that angles increase clockwise to the x axis, making east equivalent to 90 degrees. The observation from the buoys show a dominant wave direction between 0 and 150 degrees or east, northeast, and southeast. The correlation for the direction is very low because the model had issue simulating the fluctuations in the direction. This can most likely be explained by the temporal resolution of the wind data, which changes every six hours, therefore both wind direction and speed remain constant for six-hour intervals. However, the model waves are produced well within the north-northeast peak wave propagation direction with the root mean square error not varying more than 9 degrees. Therefore, these results are also acceptable to use for the domain decomposition model boundaries.
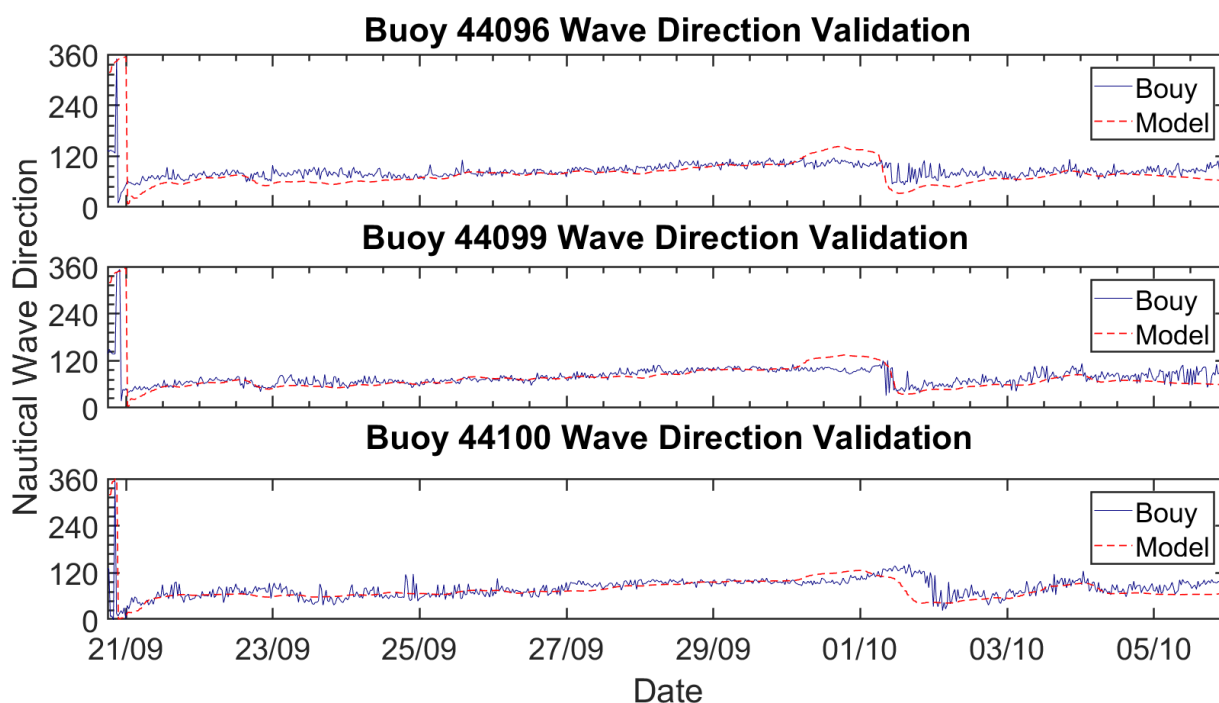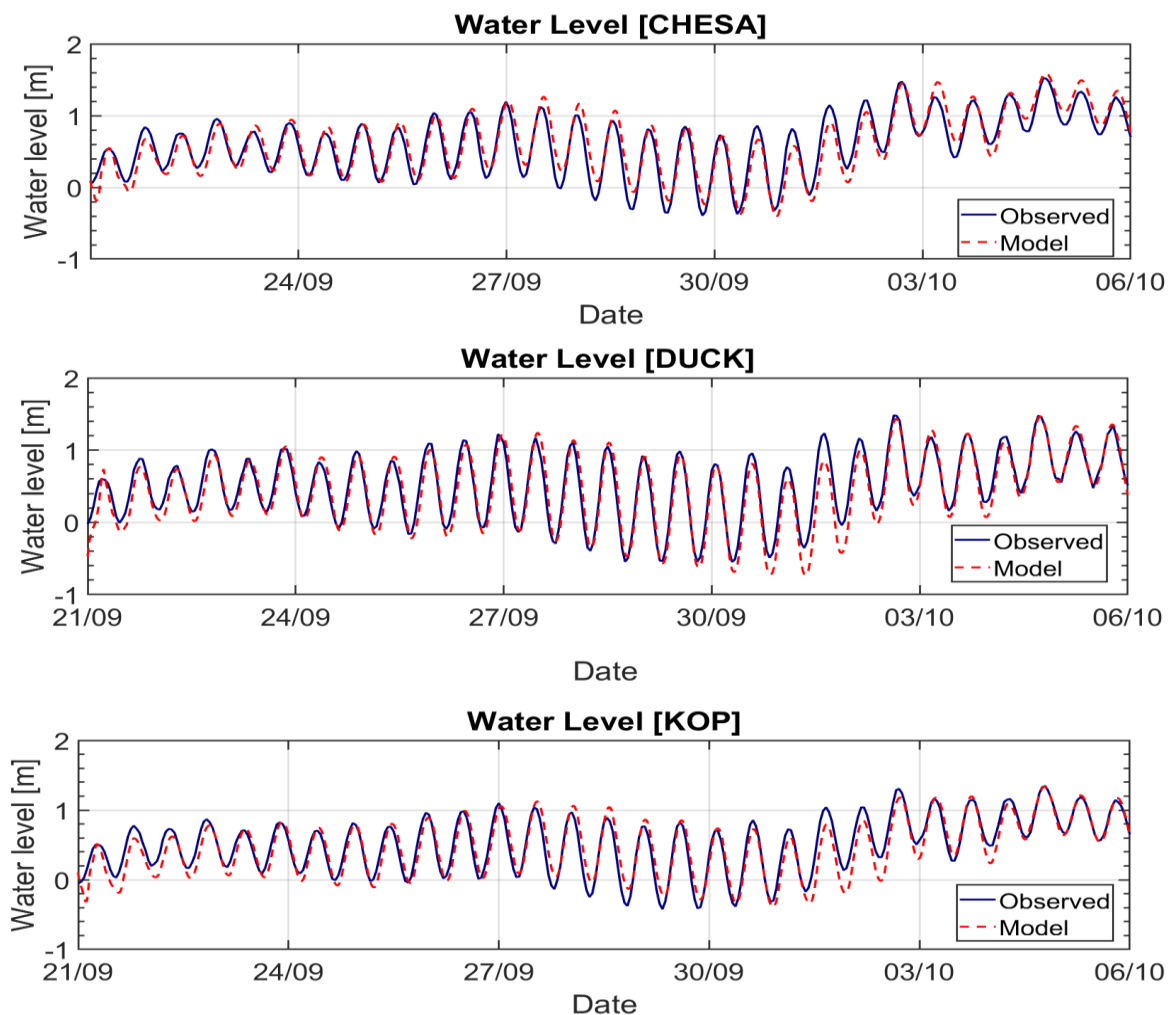

Figure 23 shows the comparison between the NOAA buoy data and the Delft 3D model results.

Water level

The model water level results are validated against historical data provided by tide stations in the region. The wind data was already validated using ADCIRC, where is was found to have a 95% correlation with this Chesapeake Bay tide station data. The model produced similar results, with a correlation of 93 % near the research site. The most significant error occurred at the Kiptopeke station where it reached 11% error. These values corroborate that results of the wind data validation, meaning the wind data is implemented properly, and can produce reasonable results for the domain decomposition model.

Figure 24 shows the water level comparisons between the model shown and red and the observed that provided by the tidal stations shown in figure 13. These water levels are measure about the MSL vertical data.

Peak Period

The model produced a smoother peak period indicated by the maximum value of the parabolic fit of the wave energy spectrum, for given time intervals. This value is used to compare with recorded buoy data provided by the NOAA for three offshore buoys at water depths varying from 15 to 20 meters. In general, the model underperforms when recreating the observed peak periods. The correlation between the model and the observed wave periods are less than 20%. Low correlations such as this is also observed in the wave directions and is primarily due to the temporal resolution of the meteorological files, causing an improper recreation of wave direction fluctuations. Fluctuations are also observed in this period data indicating a possible source of inaccuracy. The Root mean squared error varied between two and four seconds which is substantial for period of 8 to 12 seconds long. This issue is likely to reappear in the spectra, shifting the frequency energy to the higher ranges. Figure 25 below shows the peak wave period comparison between the buoy data and model data.
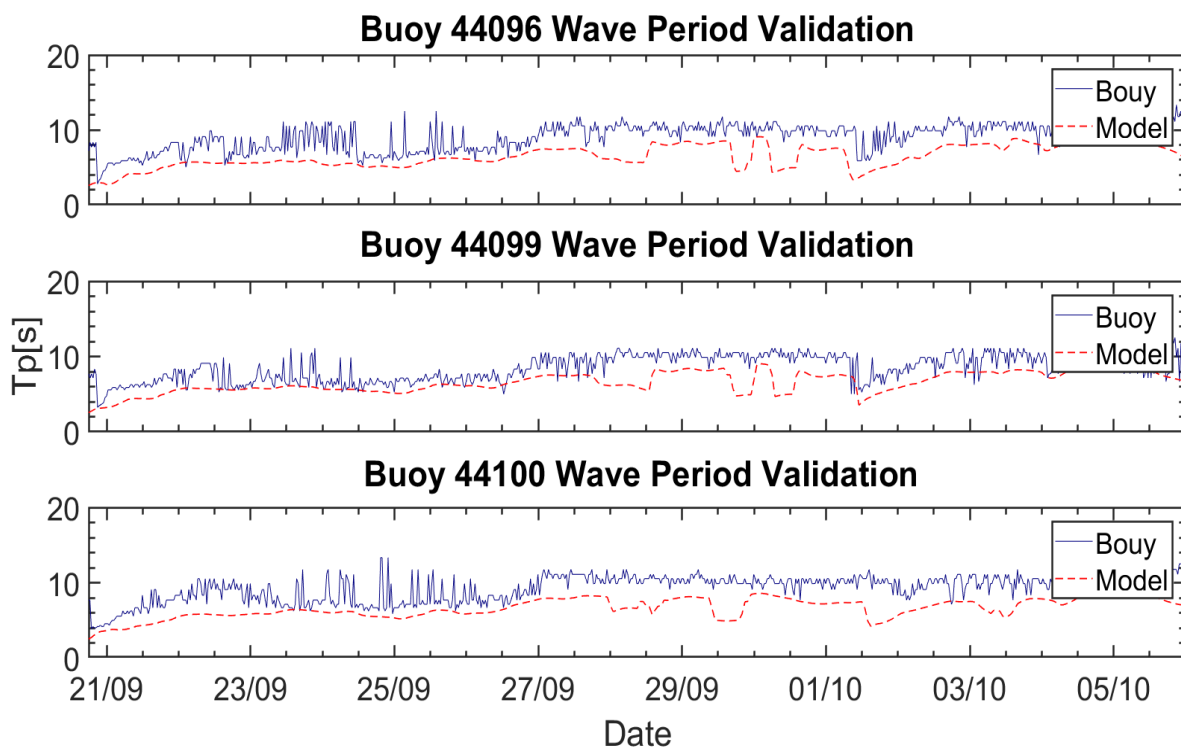
Figure 25 shows the comparison of the peaks periods from the buoy data shown in blue and the model data shown in red. The buoy data is provided by the three buoys shown in figure 13.

Points of Discussion

- Though the regional model performs well it shows difficulty in fully resolve storms surge, specifically beyond October 1st. The model implements storm surge through pressure gradients implemented by the meteorological forcing file. Inabilities to recreate storm surge may stem from improper simulation of pressure gradients in the domain. Errors like this may also be caused by the model resolution where course

model results in values that overlook key pressure or wind fluctuations that lead to appropriate resolution of the surge.

- The wave files also show a persistent underestimation which may indicate a dissipative model. The regional model also showed difficulty in recreating observed wave periods.
- The wave periods and wave heights all stem from the amount of energy transferred from the wind to the wave field, indicating a possible cause of inaccuracies

5.2. Domain decomposition Model

The Domain decomposition model is validated by significant wave height and water level using the GMU site data. Qualitatively the model simulates the expected flow patterns, with the waves penetrating during flood tide but the discharge from South Bay dominating the flow during ebb tide. Figure 26 shows these flow patterns as well as the associated current velocities and peak directions. The highest current velocities occur at the two major inlets but dissipate significantly as the approach the center of the research site.

During the period of no storm surge, indicated by the red box in Figure 27, the basin shows a phase relationship that is indicative of short tidal basins. A short tidal basin characteristic indicates a basin where the internal and external water level mirror each other. In the tidal signal this is shown by maximum current velocities occurring during a period of flow reversal and zero current velocities occurring during maximum and minimum water levels. In Figure 27 this can be seen at all three observation points, indicating a basin characteristic that is more inertially dominant and may show a lack of sensitivity to bottom friction or roughness. During storm surge conditions (shown in blue) the rising period current velocities increase typically indicating and increase in flood dominance. Moving further into the shallower regions of the basin indicated by the red and green observation points, a phase shift is observed. This is indicative of regions where bottom friction is influencing the tide. The profiles develop a progressive wave profile as the peak velocities slowly become in phase with the high-water points.
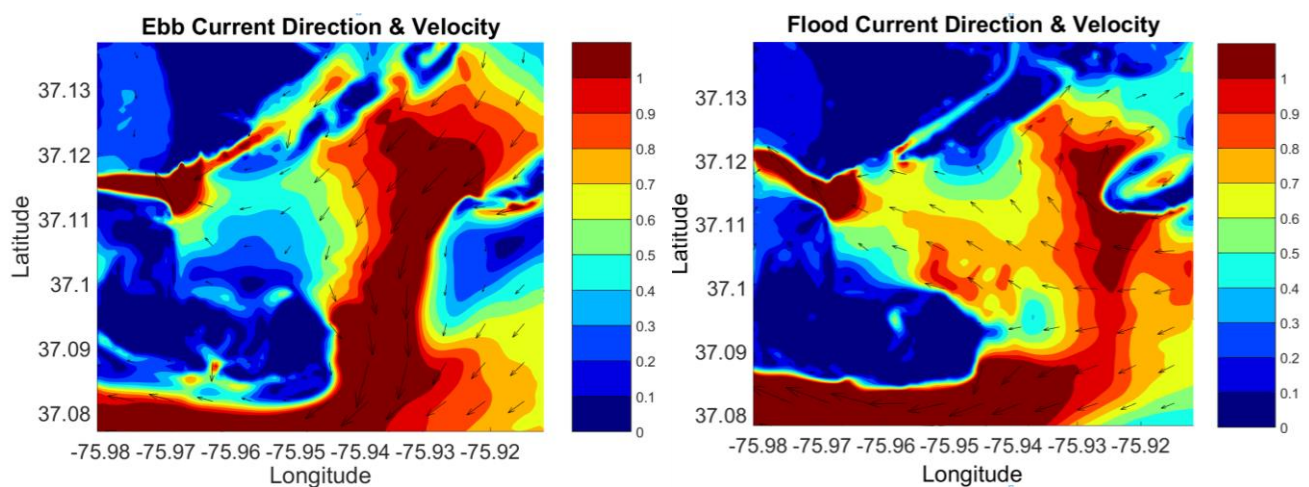

Figure 26 the top two images indicate key ebb and flood flow patterns. The colors indicate current velocity magnitudes while the arrow indicate the dominant current velocity direction.
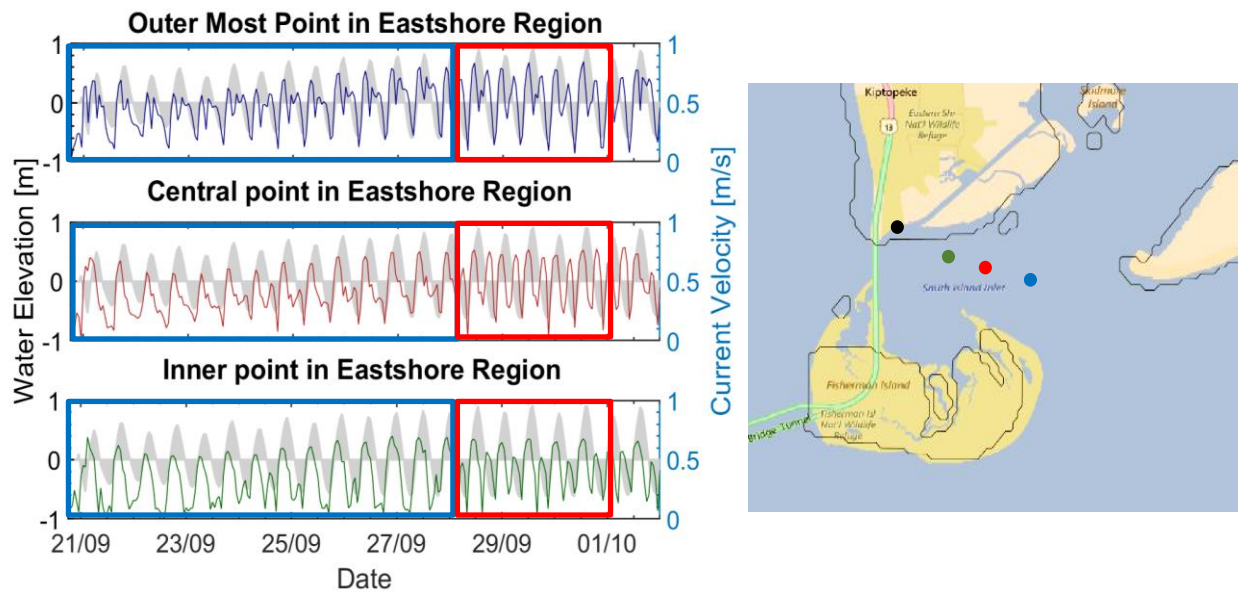
Figure 27 shows the relationship between the horizontal and vertical tide signals in the region, to help identify the dominant tidal characteristics. The figure is color coded to match the colored dot on the map to the right, indicating the positions at which these readings were taken. The storm surge period is outlined by the blue box and the period with no storm surge is indicated by the red box.

Figure 28 shows the same profile but for the salt marsh start from sensor one indicated by the black point in Figure 27. This figure shows a vertical and horizontal tide that are fully in phase at sensor one but slowly shift out of phase as the current propagates over the marsh. When the tidal signals are fully in phase it is indicative of progressive wave patterns where the tide is significantly influenced by bottom friction. Due to the shallowness of the marsh it makes sense for the friction to cause phase lag between the tidal signals. However significant wave heights in the region showed minimal change in the red and green regions indicated by the dots in Figure 27. This indicates that though the tide is impacted by the bed here, the wave height is minimally influenced by the bottom friction. It is expected that the implementation of vegetation will most likely enhance this characteristic due to increase forcing either by drag or bottom friction (depending on the forcing type).
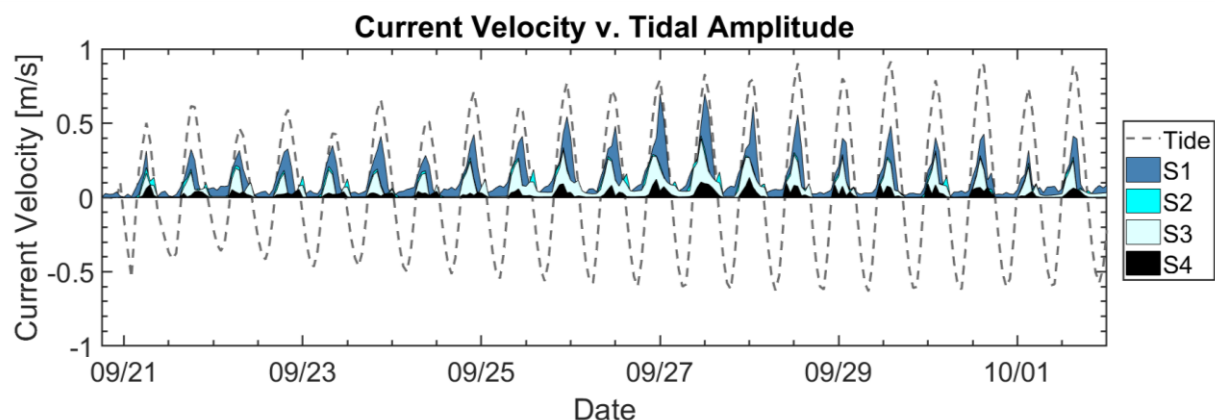
Figure 28 shows the relationship between the tidal signal and the velocities at each sensor. This shows a reduction in velocity the further into the marshland.

Validation

Figure 29 shows the water level results for the domain decomposition model, with its associated correlation, root means square error and the normalized root mean square error. Like the regional validation model, the water levels are well recreated by the model, following the wind file correlation of 95%, with this model achieving a correlation of 98%. The normalized error is 19% mainly caused by underestimations at low water levels, and the events past October 1st shown in gray. The correlation on the right shows a tendency of the model to underestimate the water levels. This model can appropriately recreate the water levels for a majority of the time period and therefore can be used to produce water levels for the SWAN standalone model. The SWAN model will conduct most of its analysis during September 27th at the highest water level point. The rest of the points excluding the gray section will be used for validation of the SWAN model.

The tide signal is incorporated into Figure 29 in the right picture to assess the ability of this model to simulate storm surge. It shows that between September 25th -28th the model can recreate the surge well, giving relatively accurate results at high water. However, at low water the model has trouble simulating the surge accurately, giving inaccurate results during the observed time. Between September 28th and October 1st, the storm is dying down and another is picking up, at this point there is no surge and the model replicates the sea state well. Past October 1st marks the point at which Hurricane Joaquin increases to category 4, creating the depression that causes the October 2nd front that seems to contribute a significant amount surge to the site. The model performs the worst here, producing the largest error. The results of the
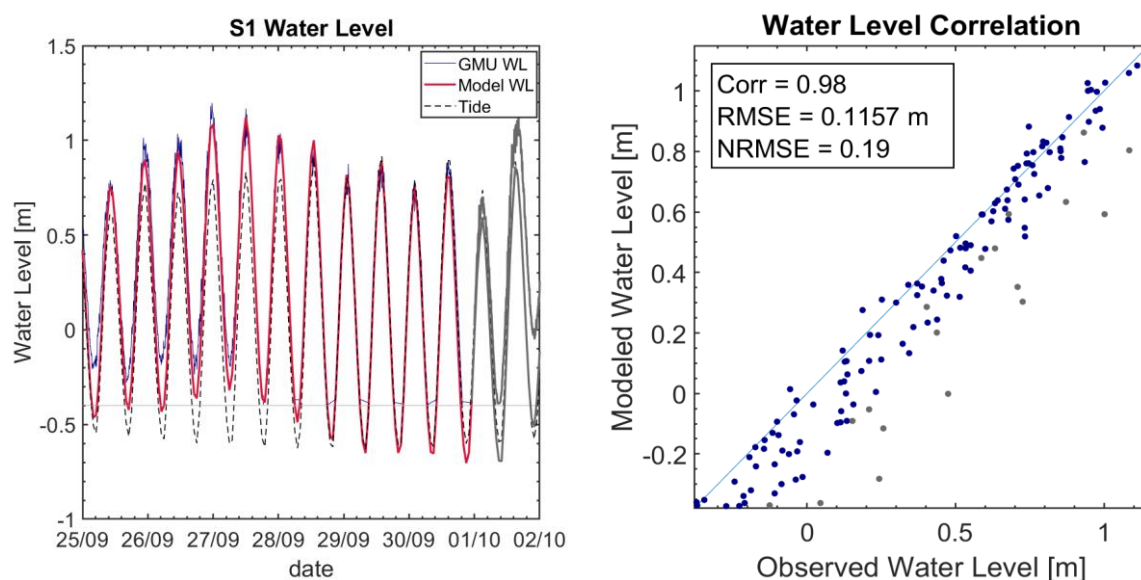

Figure 29 shows the water level validation for the Domain decomposition model.

model fit the tide signal almost perfectly in this gray area, indicating an inability to recreate the surge. This may indicate a limitation in the meteorological data when modeling this region.

Figure 30 shows the significant wave height validation of the model (in red) against the GMU field data (in blue). The model can recreate the wave heights relatively well, with a correlation of 0.86 and normalized error of 0.16. The correlation on the right shows a tendency of the model to overestimate the wave heights, with better correlation occurring at higher wave heights. The gray region matches the one discussed in the water levels. It is expected that the model would have difficulty recreating the wave heights at this time because of its difficulty in recreating the water level. The results of the correlation show that the model can appropriately recreate the wave heights at the research site. September 27th, chosen as the most accurate point in time to conduct the SWAN standalone. Therefore, the results of the SWAN standalone should be accurate for both water level and wave forcing.
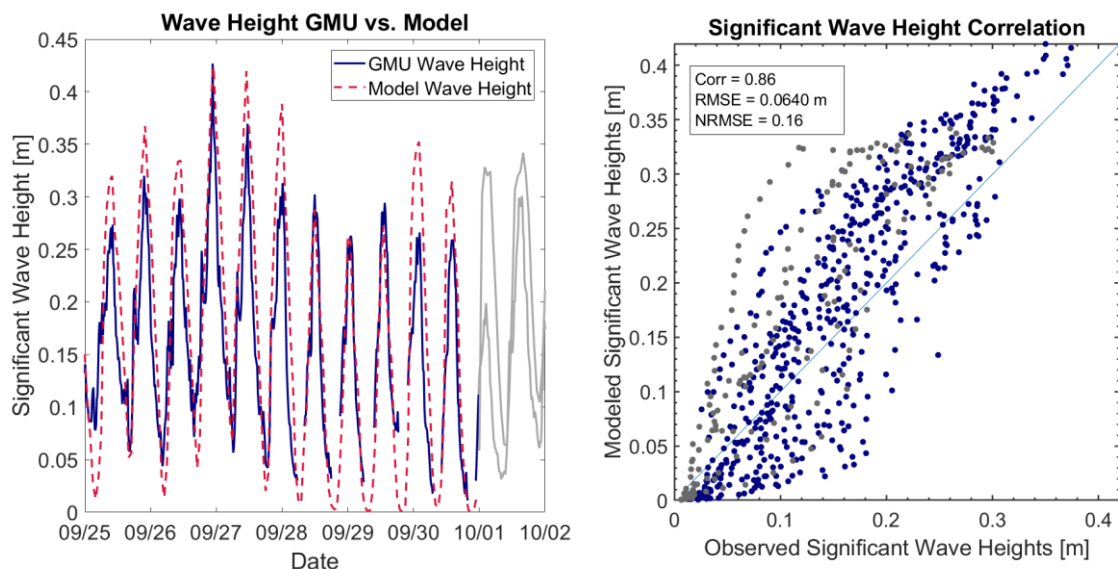
Figure 30 shows the significant wave height correlation for the Domain Decomposition model.

Points of Discussion

- The model generally showed a tendency to overestimate wave heights but underestimate water levels.
- The increase in bottom friction at the site showed to increase phase shift, causing high current velocities to occur at high water levels directly in front of the salt marsh. Combining this knowledge with the drag formulations, which indicate a reduced drag coefficient with increased current velocity, it is possible that these conditions increase wave penetration into the marsh.
- The tidal characteristics also showed a inertially dominant profile for a majority of the region, which indicates an area with low sensitivity to the bottom friction

5.3. Standalone SWAN Model

Swan standalone and the Delft 3D wave module are the same numerical model; however, the Delft 3D module is limited in its ability to change certain options available in SWAN such as the vegetation implementation. This suggest that the two model results should be similar where the vegetation does not influence the flow. This assumption holds true, indicating the proper implementation of the boundary conditions produced by the Delft 3D domain decomposition model. Because the SWAN standalone model is operated in stationary mode, a single time is chosen to conduct the analysis. September 27th at midnight is chosen from the model results because it is the most accurate point produced by the model in terms of water level and wave heights. This period also experiences the highest water level and wave height during the storm and is therefore considered the most extreme case available. Sept 27th is also situated directly at the beginning of the falling tide period, where a majority of the flow in the site is coming from the southern basin to the north and exiting the major inlets to the east and west, shown in chapter three site description. The water level currently is 1.2 meters with a significant wave height of 0.42 meters coming from the north- northeast (between 0 and 90 degrees).
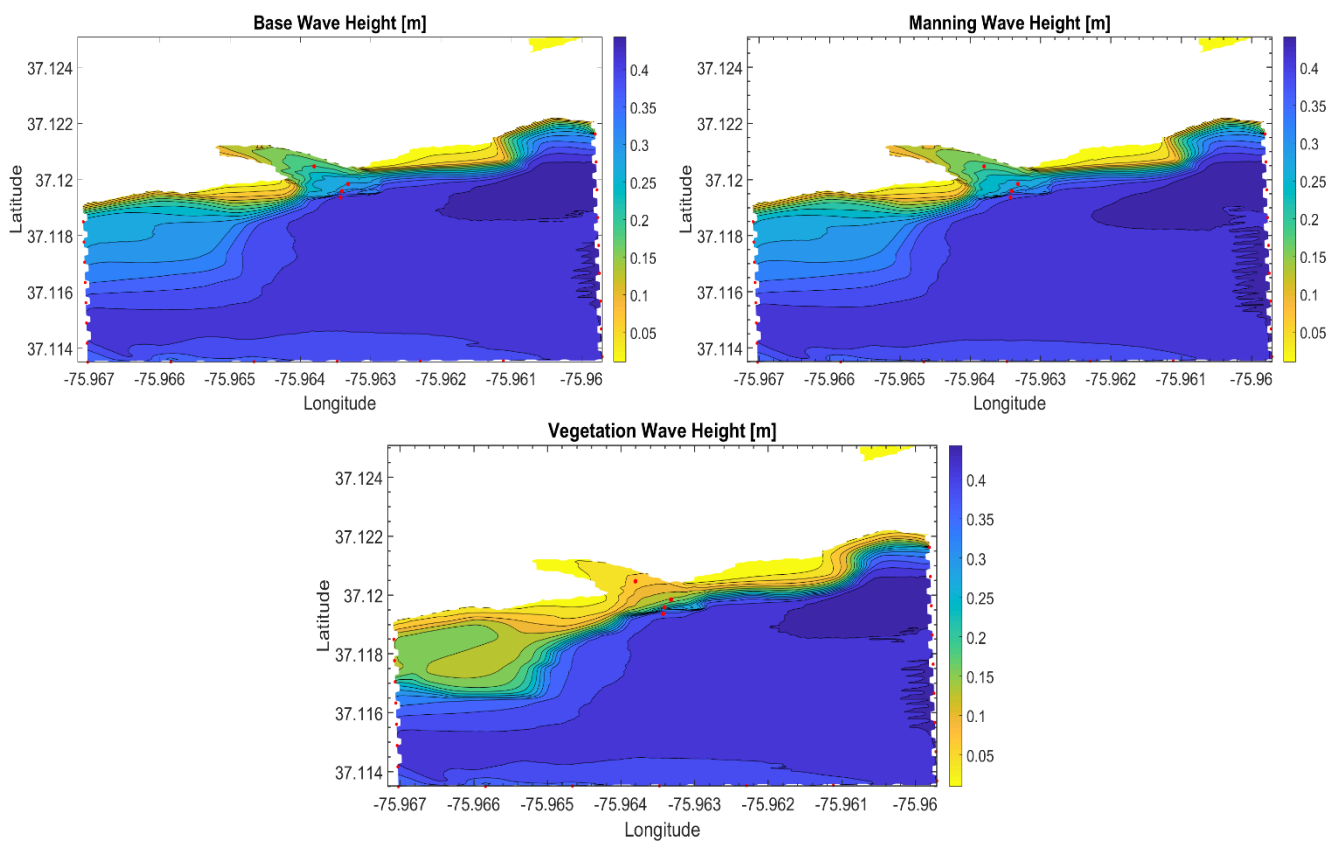
Figure 31 shows the distribution of wave heights across the domain for the base case (JONSWAP), the implicit representation (Manning Roughness) and the explicit representation (Vegetation Dissipation)

In Figure 31 the three main model runs are shown, the first being the base model with the JONSWAP coefficient of 0.06 applied to the domain. The Manning Roughness coefficient is shown to the right of the base model. These two models do not vary greatly, similar wave height reduction is observed across the domain. The vegetation dissipation implementation does show much larger wave height reduction. This is discussed further in the proceeding section. The wave heights for sensor one (furthest from the marsh), agree with the domain decomposition model results, however the vegetation implementation suggest the marsh effects the wave heights at sensor one. It is important to note that sensor one is not located over any vegetation, meaning that adjacent marshland must be impacting the incoming wave heights. In Figure 32 the flow is coming in from the right (north 0 deg), experiencing drag and friction caused by the surrounding marshland before reaching the site. Implementing the vegetation explicitly shows a clear increase in reduction of wave height coming from this northern direction as well as an increase in refraction as the wave reorients themselves eastward facing the marsh edge. This interaction most likely causes the reduction in wave height seen at sensor one when the vegetation is applied. These results appear to validate the conclusion of Smith et al (2016) and Keefer et al (2017), where it was suggested that because the manning coefficient is meant to be implemented for thin water layers in channel flows, simply enhancing it does not do enough to recreate wave height reduction over marshland. The ineffectiveness of the manning equation is also enhanced by the wave climate, which has shown to be minimally affected by bottom friction.
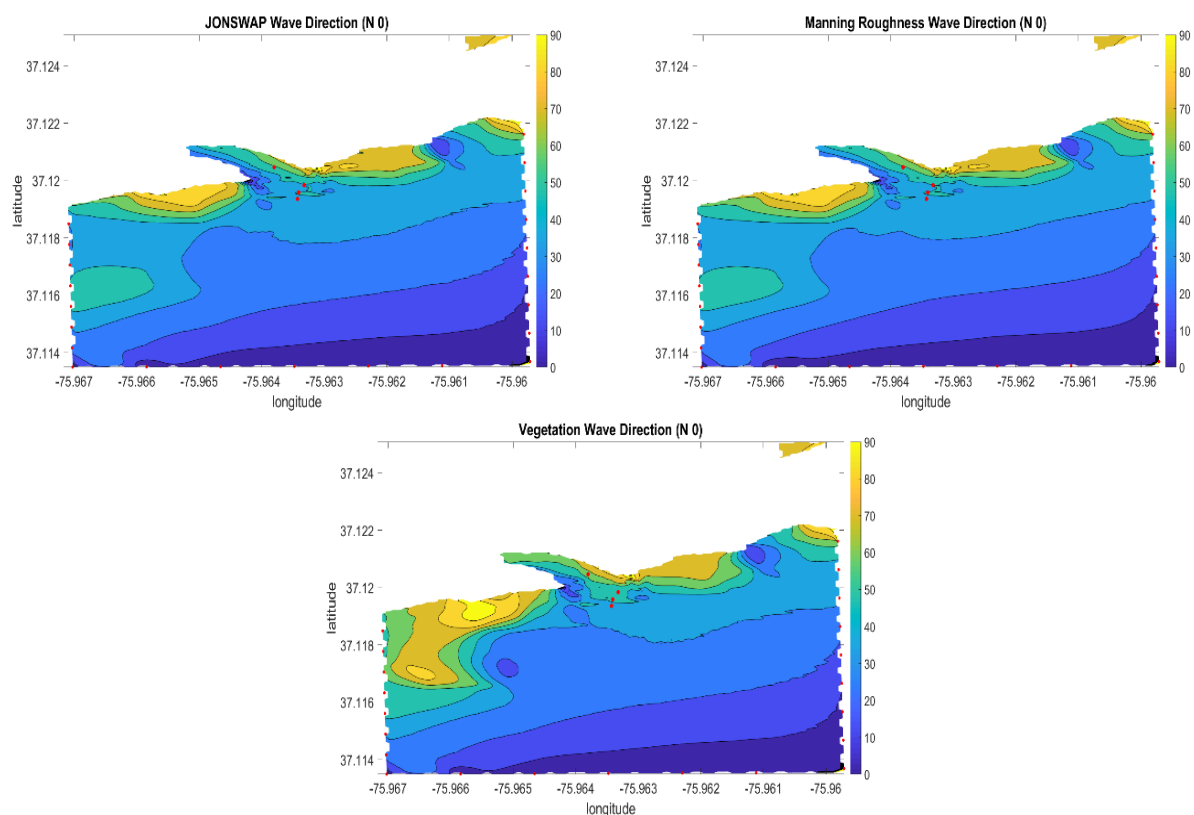

Figure 32 shows the peak wave direction for each model run with the base (JONSWAP) on the right, the implicit (manning roughness) and the explicit (vegtation dissipation). Note that in these images north points right with east located 90 degrees clockwise from the north arrow. The nautical convention is used with 0 degrees indicating north

Explicit Vegetation Dissipation Implementation

While the base run was calibrated in the previous section using the domain decomposition model, the vegetation dissipation and manning roughness formulations were calibrated using the standalone model. Variations in the drag force for the vegetation dissipation and manning roughness coefficients are applied as discussed in the methodology. The results of these comparisons are shown below, starting the vegetation implementation.

Figure 33 shows the comparison between the three drag coefficient formulations discussed in chapter four. These equations are all based on Reynolds numbers, which were determined for varying current velocities provided by the domain decomposition model. The red, blue and green lines indicate the wave height reduction using the maximum, average and minimum current velocity values respectively, in the drag coefficient formulations. Figure 33 shows a significant reduction in wave heights between 40 to 80 meters, which is indicative of the wave breaking zone typically found at the beginning of the marsh. In this region most of the drag formulations reproduce wave height within 20% error of the observed sensor one wave height, apart from the low current velocity Mendez and Losada (1999) and the Jadhav and Chen (2012), whose drag coefficients are significantly larger than all the other. At sensor two Anderson and Smith (2014) finally drops below the 20% error threshold and continues to fall with the other low current drag coefficient formulations. At sensor three the effects of the accuracy of the peak current velocity drag forces are no longer below the threshold with the Mendez and Losada (1999) and Anderson and Smith (2014) performing the same and Jadhav and Chen (2012) performing the best. The use of the average current velocity proved to be the
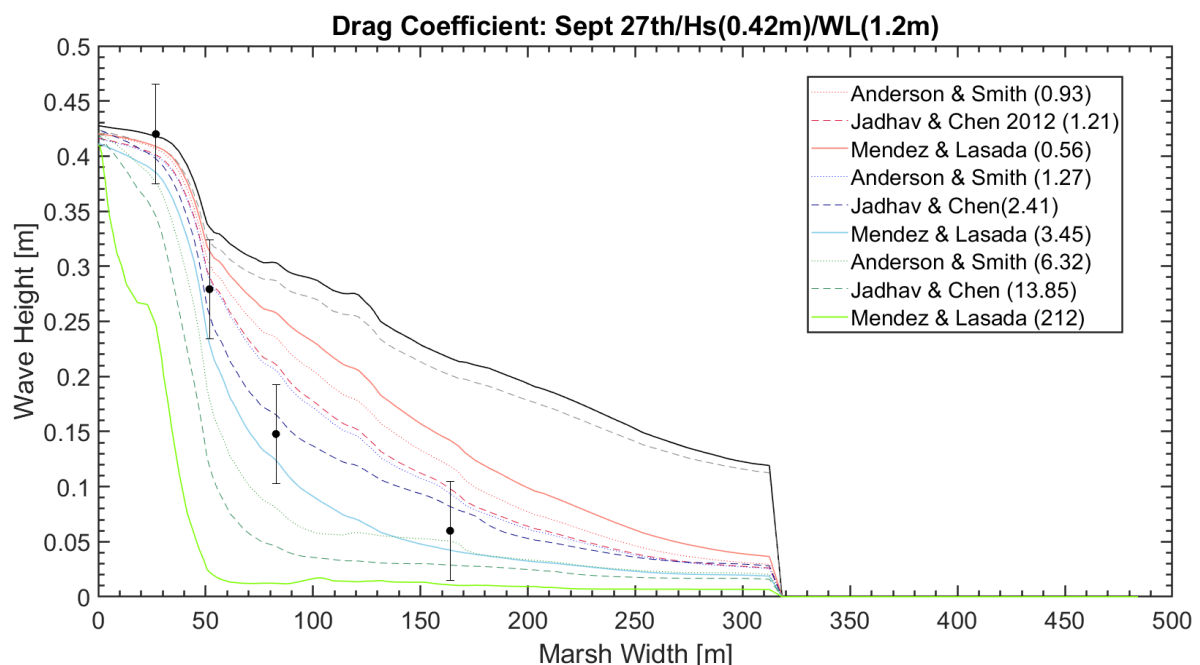
Figure 33 vegetation dissipation implementation comparisons between Mendez and Losada (1999), Jadhav and Chen (2012), and Anderson and Smith (2014) are shown above. The red indicates a max current velocity, the blue indicates an average current velocity and a min current velocity. The black dots indicate observed wave height. The values indicate the drag formulations used as well as the magnitude of the coefficients in the parentheses.

best method in recreating the entire marsh, however the fit is not exact. Both the Mendez and Losada (1999) and the Jadhav and Chen (2012) are within the 20% error marker and give results reasonably close to the observed value. Qualitatively the Jadhav and Chen value performs slightly better and is therefore chosen as the best fit. This assessment shows that both Mendez and Losada and Jadhav and Chen drag coefficient represent the dissipation reasonably well throughout the marsh, but validation on how it recreates the end of the marsh is needed. These results also show that the drag force varies greatly with the current velocities, which are not constant throughout the extent of the marsh. The accuracy of the model would benefit from the implementation of varied drag forces based on changing Reynolds number because of fluctuating current velocities.

Implicit Manning Roughness Implementation

The implicit Manning roughness implementation comparison is shown above in Figure 34. From this figure the manning roughness formulation has minimal impact on wave dissipation, not varying much from the JONSWAP bottom friction formulation. It is unable to replicate wave dissipation caused by the marshland vegetation for this site. The initial wave dissipation caused by the vegetation in the first 50 meters of the cross-shore profile is also not present here. This is most likely due to the reduced dissipation caused by the lack of proper representation of vegetation. The breaking zone is also much smaller in this profile, occurring between 30 and 50 meters reducing much less energy than the vegetation. The base manning roughness of 0.35 for salt marshes was originally used as a starting point, then the factors for marsh uniformity were added. The manning values for shrubs and marsh forest were also implemented to see if
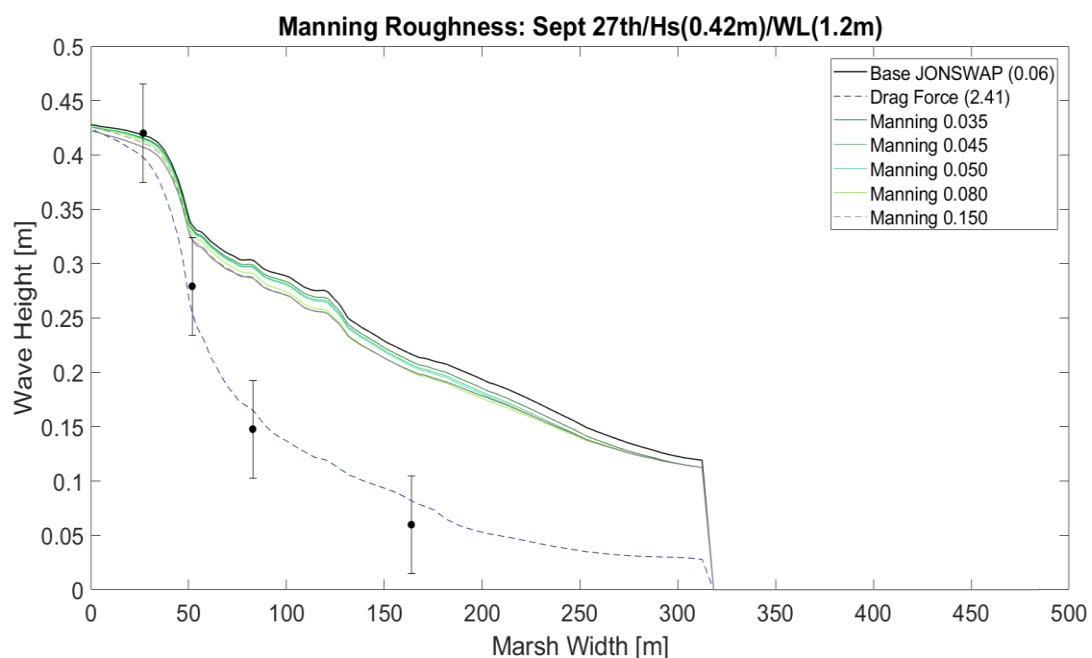
Figure 34 Shows the manning comparison of multiple manning roughness coefficients, altered using the value changes associated with uneven marshland The JONSWAP value represents that bottom friction coefficient used in the base run where no vegetation was implemented. The drag force indicates the Jadhav and Chen value that was determined to be the most accurate in the previous section. These are used to compare the performance of the model under different implementations.

a significant increase would have an impact. Figure 34 shows that manning coefficient is not able to appropriately recreate the observed dissipation rates. This is expected considering the properties of this nearshore site, meaning that the application of the manning roughness coefficient is conditional, depending environmental characteristics of the area of interest. From the conclusion from Smith et al, (2016), it is possible that the manning formulation performs better under shallower water conditions, where bottom friction is much more influential.

Explicit Vegetation Validation

A validation for both implementations are carried out in this paper, however in this chapter the explicit implementation is the only one shown. The result of the implicit representation is discussed in terms of correlation and error but the figures representing them are shown in appendix C.6.

The effects of the vegetation initially reduce the accuracy of the domain decomposition model reducing the correlation to 73%. However, the correlation along the marsh reaches 95, 97 and 94 percent with less than 12 % normalized root mean square error for each sensor. The Manning implementation resulted in good correlations of 92, 91 and 90 percent for sensors two, three and four. The initial wave climate at sensor one was only 68% correlated. From sensor 1 to 4
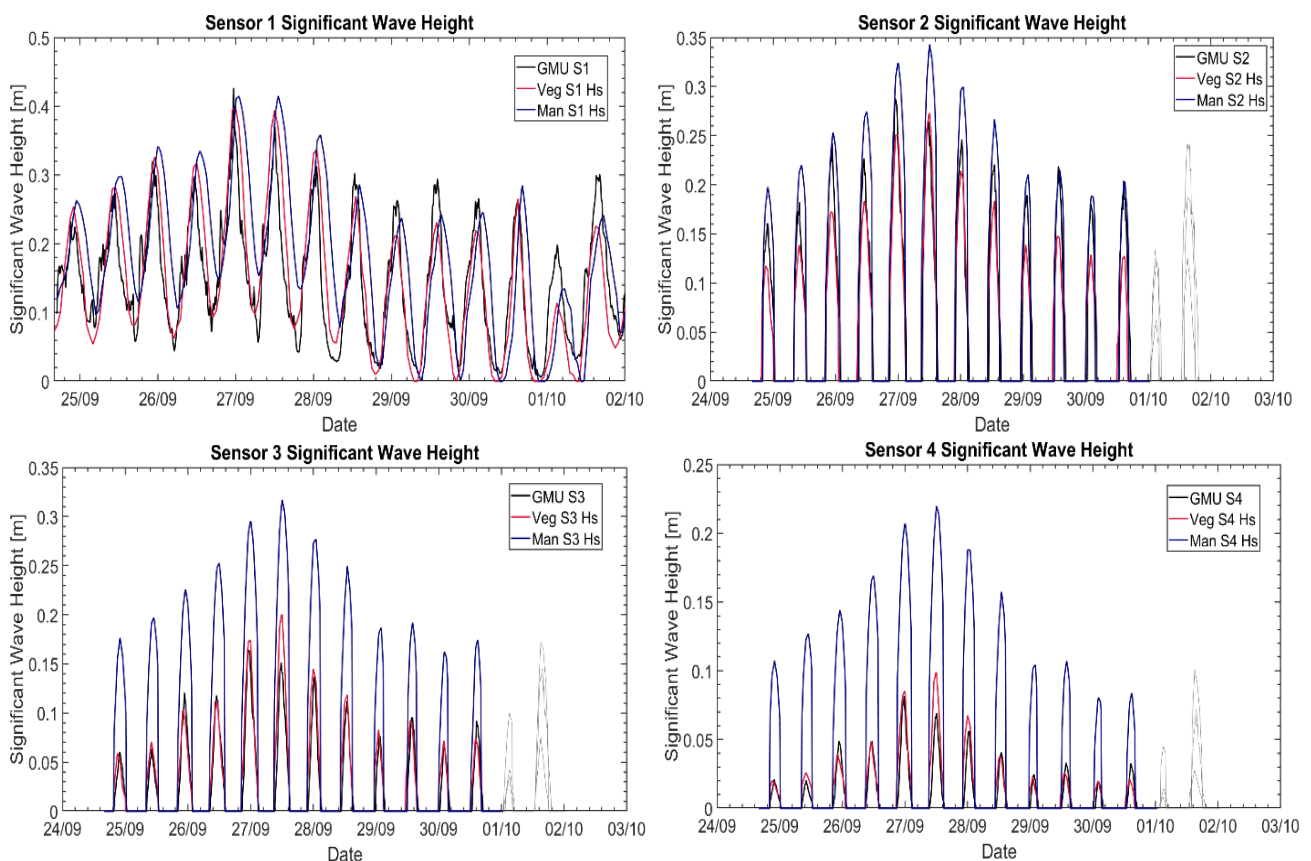
Figure 35 shows the comparison between the significant wave height at each sensor, for both vegetation implementations. The field data is indicated in black and is identified by GMU S1,2,3 and 4. The Vegetation implementation results are indicated by the red line and are represented in the legend as Veg S1, 2, 3, and 4. The manning implementation results are indicated in blue and are represented in the legend as Man S1,2,3 and 4.

the normalized root mean square error increase from 28% at the first sensor to 36%, 88% and finally 95% respectively. From these results the explicit vegetation representation performed much better in this nearshore climate.

The correlation indicates tendency to for the models to overestimate wave heights particularly at sensors three and four where the drag coefficient is expected to increase due to a reduction in current velocity. Further, the lower wave heights are better represented with higher wave heights being overestimated.
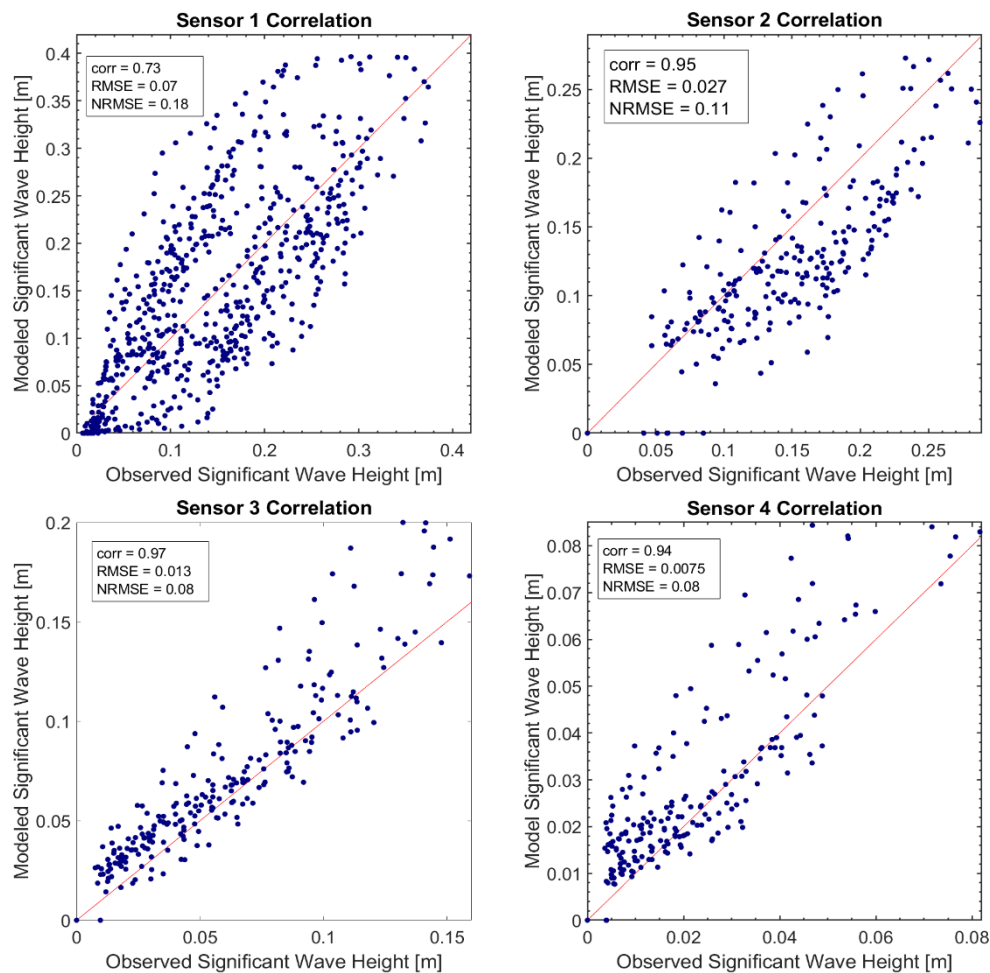
Figure 36 the correlation at each sensor with the explicit vegetation implementation.

Points of Discussion

- The difference between the two implementations is very clear. The error and correlation showed a much better performance by the explicit implementation.
- Both implementations show a sudden reduction in wave height within the first 50 meters of the shore, although the vegetation is much more significant.
- The site shows a general insensitivity to bottom friction, clearly seen by the lack of reaction to the varied manning values.

scussion

6. Discussion

The discussion section will initially focus on discussing the key point identified in results section. Then the results are summarized and compared to other studies on saltmarshes discussed in Vuik et al. 2016, Keefer et al. 2017 and Smith et al. 2016. This will be followed by limitations and uncertainties of the approach taken in this paper.

6.1. Regional model

The regional model is used primarily to recreate key storms that contributed to forcing at the research site. These storms were identified and discussed briefly in the results section. The model performed well overall but was found to be very sensitive to wind forcing which is expected considering that a majority of the domain is in deep water. Uncertainties in the wind forcing lead to inaccuracies in wave heights, water levels and wave periods.

Validation

The regional model performed well for all bulk wave characteristic resulting in wave heights that are 80% correlated with normalized errors below 12 % and water levels that are 95% correlated with normalized errors below 10%. However, the model showed consistent underestimation of the wave height and trouble recreating all surges present at the research site throughout the allotted time. The model also showed difficulty in recreating the observe peak periods at the buoys. During calibration of the regional model the sensitivity to bottom friction, breaker parameter and computational grid resolution was all tested. The model showed low sensitivity to all these parameters, indicating that the model more sensitive the wave and water level generation process as appose to the wave dissipation and propagation process. In the regional model the waves are generated through transfer of wind energy to the water surface. Water level is influenced by the pressure gradients provided by the meteorological file. An error or limit in these processes may lead to the underestimation observed wave characteristics in the model.

Wave generation and influence on wave characteristics

In SWAN the user can influence the wind forcing through breakpoints where specific wind speeds and wind drag coefficient are set. The break points are used to determine the friction velocity which is incorporated to the wind generation source term discussed in chapter two. This model uses the Wu formulation to determine the drag coefficient values, which showed to be appropriate for speeds under 20 m/s (This speed is not exceeded in the model research site). The Wu formulation expresses a constant relationship from 0 to 7.5 m/s winds, then an unbound linear relationship for speeds greater than 7.5 m/s. Though the model results showed

that this relationship appropriately recreates the wave heights observed at the buoy, the consistent underestimation at the lower values suggest that the lower wind drag threshold is too small. The Wu et al. (1982) is determined through two previous studies (Wu et al (1969); Wu et al,(1980)). Both developed the drag formulation using a combination of field and laboratory observations. However, these studies were limited by available data (observations at high wind speeds such as hurricanes winds) and use of the Charnock constant to develop the formulas. The lack of high velocity wind data partially explains why Zijlema et al. (2012), showed an inability for the Wu formula to appropriately describe the wind drag trend at high wind speeds. The Charnock constant was vital to determining the variation of roughness length with wind velocity but was described to be limited by errors in determining wind stress coefficients and errors in fitting curves used to find the constant. Inaccurate transfers of energy between the wind and water interfaces will lead in an inaccurate distribution of energy, which is used to determine the spectral profile of the wave climate. From this spectra periods and wave heights are determined. If the energy distribution is not accurate it is possible that the resulting characteristics are also inaccurate. Despite its limitations the Wu formulation has shown an ability to properly predict drag coefficients at wind speeds lower than 20 m/s. It is also worth pointing out that the transfer of energy from wind to waves is a complex process dependent on several different variables such as viscosity, wave celerity and surface tension. For this research, the wave heights and water levels are acceptable for further analysis, but inaccuracies in the results may stem from several uncertainties present in the formulas used to determine the wind drag. Besides the Drag coefficients, uncertainties in the source term may also lead to inaccurate results, though there is little influence that the user may have on this.

Pressure and Water Wave

The amount of influence the meteorological file has on the wave climate is also dependent the pressure wave created using a Fourier transform of the pressure gradient. If the pressure wave resulting from this calculation is in phase with the water wave, energy transfer between the wind wave interface occurs. This process impact both wave characteristics and water levels.

In Delft 3D, water level is also affected by a number of different variables, the first being the pressure gradients provided by a space and time varying meteorological file. The pressure gradients are determined using the hydrostatic pressure formula integrated over the mech and time interval. This means that the water level depends significantly on the accuracy of the meteorological file used. Water levels are also significantly influenced by the tidal range of the site, which is provided by the boundary conditions in the form of TPXO files. The tidal ranges are added to water level gradients to provide the final water level, meaning that an underestimation of tides can result in underestimation of the final water levels. This model showed a slight underestimation of the tidal range between September 27th and October 2nd which matches up with water level errors. Tidal range errors can be caused by an error in the file but may also occur when a model is too dissipative, meaning the bottom roughness applied in the flow model is too high. However, the error in the water level is too high to be just the

tides therefore the inaccuracies is most likely due to a combination of uncertainties in the meteorological forcing, tidal forcing, and physical forcing parameters.

6.2. Domain Decomposition

The Domain Decomposition is used to recreate the east shore region of the Chesapeake Bay, which requires a much finer bathymetric grid then the one used in the reginal model. It is important that the model not only recreates the significant wave heights and water levels but also creates the distinct flow patterns observed during the falling and rising periods of the tidal cycle explained in section two of chapter five.

Validation

Like the regional model, the domain decomposition model is able to accurately recreate both the significant heights and water levels. Water levels showed good correlation in the water level (98%) with a normalized error of 19%, while water levels also showed a good correlation of 86% and a normalized error of 16%. Inaccuracies in the domain decomposition matched inaccuracies in the regional model. Most of the errors occur at low water levels, which is evident in the correlation where a consistent underestimation is observed. The tides are included in the water level comparisons for this model identify where the surge is being underestimated or not represented. From this comparison the time period past October 1st, showed little to no variation from the tidal signal. Like the regional model the wave heights were much more heavily impacted by the wind forcing applied to the domain. The results show that for a storm with wind speeds below 20 m/s, the Wu formula can adequately recreate the wave climate.

Impact by bottom friction and Breaker parameter

Unlike the regional model the region is shallow enough to also be influenced by both the breaker parameter and the bottom friction. However much higher sensitivity was shown for the breaker parameter as appose to the bottom friction. The bottom friction was chosen to be 0.06 JONSWAP coefficient to indicate a wave climate that is both influenced by swell and locally generated wind waves, with a dominance toward wind waves. However, the underestimation of wave heights at lower water levels, indicate that this value may be to large, a value of 0.05 to 0.055 may be more appropriate. On the contrary the breaker parameter is much more impactful on the wave climate. (Massel, 1996) and (Nelson, 1994) indicated breaker parameters below 0.6 are more appropriate for relatively flat regions such as this research site. The calibration of the domain decomposed model showed this to be true, as a breaker parameter of 0.5 resulted in the most accurate recreation of the observed wave heights. However, there were still situations where the wave heights and water levels were overestimated, possibly due to inaccuracies in the meteorological in recreating local wind conditions as discussed in the earlier sections.

Tidal Characteristics

The domain decomposition model produced a sinusoidal tidal signal that showed no dominance by either the ebb or flood tidal cycles. It was also found that maximum current velocities occurred during the falling and rising tidal periods, while the minimum current velocities occurred during the maximum and minimum water levels. These characteristics are found at the first observation point, and typically occur in short basins, where the water levels within the basin match the water levels at sea. This makes sense given that the position of the first observation point is located near an inlet. The short basin characteristics hold well into the research site, being visible at all observation points indicated in Figure 27 during periods of no storm surge (between September 28th and October 1st). This characteristic means that during high tide, larger wave height are able to penetrate deeper into the inlet. Figure 37 shows two high tide conditions at different water levels. Both conditions show a penetration wave height between 0.8 and 1 meter in the region where short basin characteristics are observed. Because the water levels vary but the wave heights do not significantly decrease at the lower water levels where bottom friction would dominate, it can be said that these regions are more inertially dominant. This indicates that the site a low sensitivity to the bottom friction. Furthermore, as the wave propagate into the inlet there is a difference in wave heights between the two images, however this difference is not cause by the bottom friction. It is instead caused by the change in water depth which occurs at X in Figure 37, decreasing the wave height based on the breaker parameter. Once the waves are in Y they show little change until sensor 1, again indicating the minimal impact of bottom friction in this region.
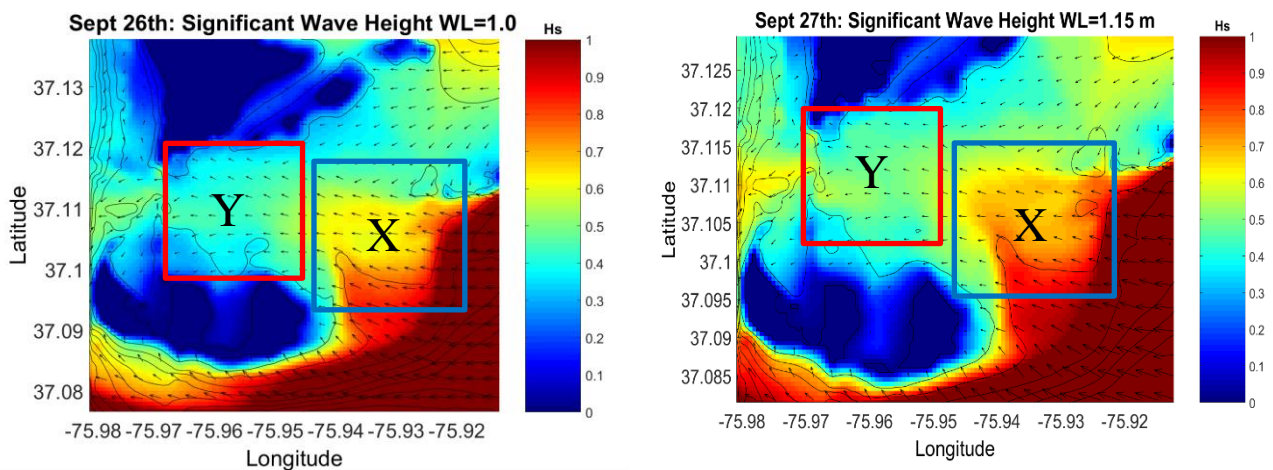
Figure 37 shows the penetration of the signficiant wave height for September 26th on the left and September 27th on the right.

The inclusion of storm surge increased the rising period velocity result in enhanced flood dominance in the area due to storms. However, as the wave climate propagates into the research site, a phase shift occurs due to bottom friction, slowly moving peak velocities in phase with maximum and minimum water levels until they reach sensor one. This phase shift is significant when talking about drag coefficient. The larger the current velocities the lower the drag coefficient. The lower the drag coefficient, the less dissipation that will occur by the vegetation.

Therefore, if the highest currents fall in phase with the highest water levels, which incidentally have the highest wave heights, then larger wave heights can penetrate deeper into the marshland. This may indicate a climate where wave dissipation by marshland is limited by the tidal characteristics. It highlights an area that merits consideration when developing marshland for coastal defense purposes.

6.3. SWAN model

The SWAN standalone model is used to assess the difference between the implicit manning roughness coefficient method and the explicit vegetation dissipation method. Like the previous sections, the validation of this model for both methods are initially assessed. These validation results distinctly show which method performed better at replicating the energy dissipation across the marsh. This will be followed by a description of the cross-shore energy dissipation profiles shown in the results section. In this section the cross-shore wave height reduction profiles shown in the results are discussed, identifying key characteristics as well as the contribution to dissipation different wave dissipation mechanisms have on the wave climate. Theoretical explanation behind the results is then given followed by the influence the Delft 3D models have on the Standalone SWAN model.

Validation

The validation for the stand-alone SWAN model was carried out for both vegetation dissipation implementation methods. The results showed that sensor one does experience some reduction in wave height when the vegetation is applied to the domain, changing the significant wave height results. Therefore, the profiles provided by the domain decomposition model and the SWAN stand-alone are not completely identical. The SWAN model can recreate the climate with a 73% correlation and a 0.18 normalized error which is acceptable as seen in Figure 37. The model can appropriately recreate the wave heights during the storm surge periods but begins to underestimate the wave height during periods of no storm surge (September 28th to October 1st).

The reduced water level increases the influence of both the drag and bottom friction on the wave heights, therefore reduction of the bottom friction is a good first step, since this value may also be causing issues in the Domain Decomposition model. Once past the first sensor, the vegetation dissipation model is able to recreate the waves with a 95, 97 and 94 percent correlation from sensor two to four respectively, all below a normalized error of 12 percent. The vegetation dissipation model shows a tendency to overestimate wave heights, with the most egregious overestimations occurring past October 1st and on September 27th at noon. The period beyond October 1st are the points where all three models consistently perform the worst, indicating an issue that cascades from model to model. On September 27th the increased wave height occurs at sensors three and four. The wave height during this time period at sensor two agrees well, indicating a change between these sensors that impacts the results. Between the sensors the bathymetry changes, the wave direction changes, and the current velocity changes. Among these variables current velocity has the most influence on wave reduction due to its

impact drag forces. Because the average velocity is used to determine the drag coefficients, current velocity is likely too high at these points, resulting in a low drag force and increased wave heights.

The manning roughness implementation performs worse at sensors two through four, showing significant overestimation of the significant wave heights. The correlations are still high, all reaching 90% but the error increases the further into the marsh from 0.36 at sensor two to 0.89 and 0.95 at sensors three and four. This shows a clear inability by the manning coefficient in its ability to replicate the dissipation observed by vegetation, validating the conclusion made in (McKee Smith, Anderson Bryant and Wamsley, 2016) and (Keefer, 2017).

Cross Shore Wave Height Reduction Profiles Implicit Vegetation representation
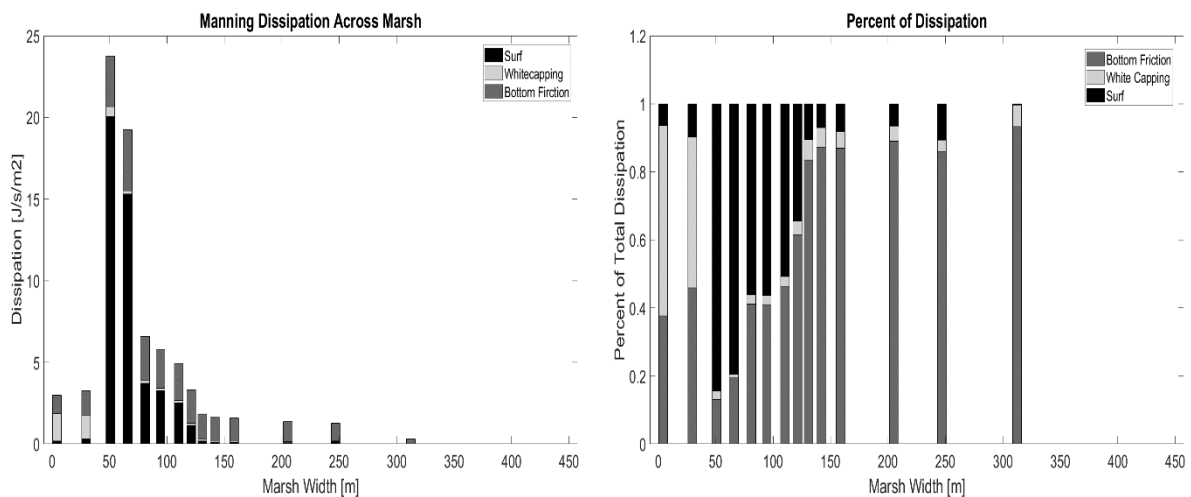
Figure 38 shows the cross-shore profiles of the for the energy dissipation occurring under the Implicit vegetation representation. Both graphs are color coded to indicate the energy dissipation mechanism and do not solely show dissipation by the implicit manning roughness. The figure on the left indicates the energy dissipation magnitudes while the figure on the right indicates the percent of total dissipation that each mechanism contributes along the marsh.

The implicit manning roughness implementation shown in Figure 38 showed a region of significant energy dissipation where 60% of the total dissipation takes place. At this breaking zone the incoming wave energy is reduced by 43 J/s/m^2 between 30 and 80 meters into the marshland. Figure 38 shows a wave climate that is originally dominated by whitecapping and bottom friction but transition to other forms of breaking as the wave climate reaches the marsh. This likely a result depth induced breaking, which has shown to be dominant in the entire region not just the study site. As the Wave transitions to the rear of the marsh the dissipation by breaking is reduced and the manning roughness begins to dominate wave dissipation in the area. The magnitude of the dissipation because of the manning roughness does not change significantly, throughout the profile, until the very end of the marsh where water levels and wave heights are too small to contain any noticeable energy. The percentages shown on the

right of Figure 38 indicates the transition in influence from on mechanism to another, illustrating that bottom friction or roughness holds more influence at lower water depths.

As discussed in chapter 2, the manning roughness coefficient is implemented into SWAN as a bottom friction term that has been adapted to represent different vegetation covering. The manning values are incorporated into the Bretschneider et al. (1986) equation used to relate the nikarudse friction length (Kn) to the manning n roughness coefficient. The friction length is incorporated into the Madsen formula to determine a bottom friction coefficient that is partly dependent on the root mean squared bottom orbital velocities. The Madsen formula stems from Madsen et al. 1988 paper that conducted lab experiments examining relationships between sediment response and wave attenuation under wave forcing. Basic bed geometry and their associated Nikarudse friction length values were determined. The friction length in these experiments were determined for a single sand grain size, and only address the interface between the water column boundary layer and the bed. The interaction between bed and the boundary layer may lead to the creation of bed forms through turbulence and radiation shear stresses resulting in an increase roughness. Bretschneider et al. (1986) created the equation relating the friction length to the manning roughness coefficient. The manning values were originally made for assess open and closed channel flow which typically deal with water layers that do not experience the same level of obstruction that occurs in a marsh by tall vegetation. These values have been adapted to fit a wide range of material from concrete and gravel to salt marsh vegetation. The adaptation of these bottom roughness values for vegetation do not address all the physical interactions that occur when a plant of significant height obstructs the propagation of a wave. Chief among these interactions is the incorporation of drag forces across most of the water column as appose to an interaction at the boundary layer. The wave climate of the east shore site serves to highlight the difference between bottom roughness formulation and the incorporation of drag forces. The inertial characteristics of the tidal climate in the region also reduce the impact that bottom roughness would have if a site was friction dominant.

Cross Shore Wave Height Reduction Profiles Explicit Vegetation Representation

Compared to the implicit manning roughness implementation the explicit vegetation dissipation representation showed far less dissipation because of wave breaking. Though white capping is present at the edge of the shore, like the implicit results, wave breaking in general stop at the beginning of the breaker zone. Instead the vegetation is shown to dominate immediately, contributing 70% of the total energy dissipation between 30 and 80 meters into the marsh. The domination of wave energy is consistent throughout the marsh, however the percent contribution on the right of Figure 39 shows a trend of increasing influence by bottom friction as the wave penetrates the marsh. The explicit representation also significantly reduces the wave heights penetrating the marsh, by 44% in the first 80 meters.

As discussed in chapter two, the explicit vegetation representation is implemented into SWAN as cylinders, suggested by Dalrymple et al. (1984), whose characteristics can vary vertically and horizontally. In SWAN the energy loss because of vegetation is determined by work done on the water column. The Drag force due to pressure gradients across the water column are applied along the entire height of the plant. The fact that the drag force is applied along the entire vegetation height means that the forcing is not limited to the boundary layer. The explicit vegetation representation provides, and overall larger surface area for which forcing can be applied, because it combines bottom friction by sea bed material with Drag forcing by plants.
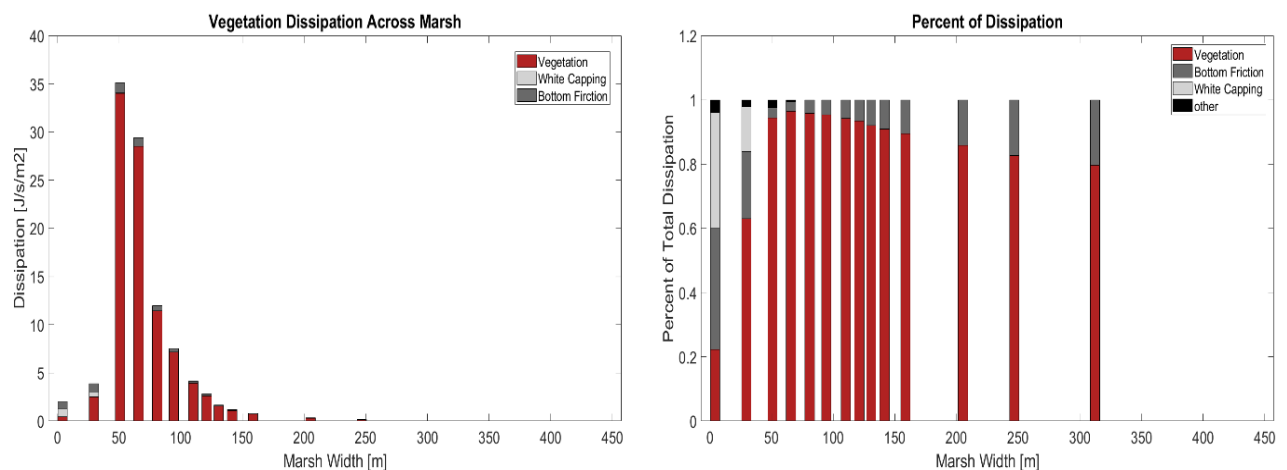
Figure 39 shows the cross-shore profiles of the for the energy dissipation occurring under the explicit vegetation representation. Both graphs are color coded to indicate the energy dissipation mechanism and do not solely show dissipation by the implicit manning roughness. The figure on the left indicates the energy dissipation magnitudes while the figure on the right indicates the percent of total dissipation that each mechanism contributes along the marsh.

Variation in drag force and manning roughness coefficients

The variations in drag force formulation showed that the Jadhav and Chen (2012) drag coefficient performed the best out of the three formulations. As discussed in chapter 4, the main difference between these formulations are that the Jadhav and Chen was derived using filed observations of a marsh covered by spartina alterniflora under forcing from a cyclone, whereas the other two were laboratory experiments that use stiff cylinders (Mendez and Losada, (1999), and flexible plastic strips to derive the drag formulation.

These formulations were varied based on Reynolds numbers as a function of current velocities provided by the model. The peak mean and minimum current velocities were selected from the Delft 3D model and applied to the formulas. It was revealed that the average current velocities performed the best overall while the maximum current velocities underestimated the dissipation and the minimum current velocities overestimated the dissipation. However, the maximum current velocities performed much better that the beginning of the marsh where the max velocities are most likely to occur, whereas the minimum velocities performed better at the back of the marsh where minimum velocities are expected. This indicates the necessity of a varied drag coefficient to recreate the wave climate appropriately throughout the marsh. The average velocity showed a sudden drop in wave height at 310 meters into the marsh, which is not completely representative of reality. It is more likely that the wave height dissipates more gradually.

Implementation of the manning roughness was carried out by implementing the base manning values for salt marshes (0.035) and altering the magnitude based on marshland uniformity. These values are discussed in (Arcement and Schneider, 1989) and (Bunya *et al.*, 2010). Manning values for shrubs and coastal forest were also tested to see if significant increases the magnitude effected the dissipation profile. While the increase in manning roughness coefficients showed an increase in dissipation rate, the magnitude is not significant enough to improve the accuracy. As previously stated the lack of drag coefficient significantly handicaps the manning roughness coefficient when attempting recreate marshland, specifically marshland with vegetation that is a meter tall. As Smith et al. 2016 suggested, the manning roughness is better suited for channel flows with thin water layers and relatively short vegetation.

6.4. Summary of Results and Comparison to Other Studies

In general, across the eight days between Sept 24th to October 2nd the salt marsh reduced wave heights by an average of 96.5 % in 310 meters. In the first 50 meters an average of 42.5% of the total wave heights were reduced amounting to a total energy reduction of 70%. Over the entire length of the saltmarsh vegetation contributed to 92% of the total energy dissipation, while bottom friction only contributed to 5% of the total dissipation with the remaining 3% being dissipated by wave breaking before the presence of vegetation. Like Vuik et al. (2016), no clear breaking zone is present due to the vegetation. Instead the wave dissipation process is

smoother and is dominated by the vegetation which increases the total dissipation by 30%. The 30% increase in wave energy dissipation translates in a 0.1 to 0.3 meters difference, which is like the results produced by Keefer et al. (2017).

When comparing these results with Smith et al (2016), the percent change in wave heights was larger. Smith et al (2016) showed a reduction of 50% over several hundred meters which was much smaller than the 96.5% average wave height reduction observed over 300 meters in this research. This value was also larger than the total percent wave height reduction observed in the Vuik et al. (2016) and Keefer et al. (2017). This is mainly due to the difference in intensity and forcing of the storms. Keefer et al. (2017) and Anderson et al. (2016) both carry out their analysis under stronger storm conditions which produce higher wave heights and water levels. These three studies all observed more intense storm conditions compared to the one recorded in the east shore site. (McKee Smith, Anderson Bryant and Wamsley, 2016) and (Vuik *et al.*, 2016) both addressed a variety of different forcing conditions where the neither which reach wave heights below 0.4 meters. Keefer et al. (2017) assessed forcing by hurricane sandy which produced the highest wave heights among the three. One of the main differences between these storms and the one used in the paper, is the drag coefficient used. Keefer et al. 2017 based the selection of her drag coefficient on the value indicated by (Vuik *et al.*, 2016), which was 0.4 determined through calibration. Smith et al (2016) determined their drag coefficient using a formulation produced by their 2014 paper. This formulation was tested in the paper as well as (Vuik *et al.*, 2016), and varied by reynolds number, similar to all other formulations that were tested. The difference in drag coefficient indcates a lower current velocity observed in the the eastshore salt marsh than the other site. This would result in the higher wave dissipation observed in this region, however the drag coefficients in the field are dependent on more than just curren velocities. The vegetation characteristics play an important role in varying drag values between sites. The vegetaiton characteristics in the Eastshore site are larger than those at the dutch site, and the sites observed in the Smith et al (2016). Therefore a larger drag formulation would need to be implemented to address this difference. Along with this, the hieght of the vegetaiton is consistantly high enough to extend throughout most if not all of the water column, in some cases emerging above the water surface. This would also lend to an increase in drag force and overall wave dissipation. An overall summary of the result is provided in appendix E.

6.5. Limitations and Uncertainties

Beyond the uncertainties and limits in the Delft 3D and SWAN models, throughout the research certain choices were made that could limit the ability of the model to accurately recreate observed field data. These limitations vary from the data resolution to selection of variables and are shown below and discussed briefly.

- Inacuracies in periods and spectra
- Data resolution
- Partial resolving of the South Bay

- Choice of 0.06 for the JONSWAP bottom friction
- Use of Delft 3D Current Velocities
- Use of constant Drag forcing
- Use of constant vegetation characteristics

Underestimation of buoy periods and the Resulting Spectra

This inaccuracy in the periods showed up in the nearshore spectral analysis, shown in Appendix D. The spectral analysis of the field data showed a wave climate where a majority of the energy resided between 0.3 to 0.5 frequency bands. There is also another peak located in the 0.1 to 0.25 frequency bands, these concentrations indicate a wave climate that mostly dominated by locally generated winds with partial influence from a swell wave climate. The resulting model spectra indicated a similar bimodal profile, with peaks present in the 0.1 to 0.25and 0.4 to 0.6 frequency bands. The model's high frequency peaks were shifted to the right, indicating a higher energy concentration at shorter periods or higher frequencies in the model that is not present in the field data. However, the energy magnitude and dissipation are consistent throughout the domain indicating issues with the transfer of energy from high to low frequencies. A slow increase in dominance of lower frequency waves is recreated although not completely accurate. Considering the connection between the peak period and the spectra, it is likely that the issues stem from the initial generation of the waves which are strongly dependent on the meteorological file. The inability to recreate the spectra, hinders detailed analysis of energy transformation over the marsh to be validated by field data.

Temporal and Spatial resolution of data

Temporal and Spatial resolutions vary between data sources and can have a varying degree of influence on model results depending on the temporal and spatial size of the natural phenomenon that are being recreated. Course resolutions tend to miss key smaller scale features that have a varying degree of influence the resulting wave climate while resolutions that are too fine tend to be time consuming. Striking a good balance between these two issues is important and strongly dependent on the data available. For bathymetry most, key features have been properly resolved besides the South Bay, whose significance would need to be assessed using a larger SWAN standalone model. The coarsest bathymetric data is provided by the GEBCO, which is mainly used to recreate deep sea conditions which are not impacted by bathymetric features. As previously stated this data is also used to partially recreate the South Bay whose significance is unknown. Temporarily the Wind data is the coarsest data set, with time intervals of six hours. This data set showed to be appropriate when creating the water levels and wave heights but struggled with periods. These characteristics are strongly dependent on the conditions under which the waves were generated, typically by storms with given wind stressing represented by meteorological files. The wind speeds and wave directions may vary much more than once every six hours. The Fort.22 file was deemed acceptable because the error was below eight degrees, which indicated that waves and therefore wind are coming from the correct direction. It is possible that wave periods are much more sensitive to wind direction then other characteristics and require a temporally finer wind data set.

Partially Resolved South Bay

The significance of the South Bay was only realized later into this research and is therefore only partially resolved by the Virginia Tsunami Digital elevation model, the rest is resolved by the GEBCO data. This means that in the model part of the bay is represented by a course computational and bathymetric grid most likely does not capture all key feature in the region. The South Bay is also covered by a significant amount of saltmarsh vegetation, which from this paper has shown to significantly impact the resulting wave heights and energy. In the model, it is observed that during the ebb cycle, the shallower regions covered by the salt marsh are affecting the flow of the tidal water level into the region. This characteristic is most likely enhanced by the presence of the vegetation. However, the results showed that the wave height and water level were accurate enough without full resolution of the model and therefore resolving the South Bay is kept a next step.

Choice of JONSWAP 0.06 bottom friction

The choice of the JONSWAP 0.06 is based on a number of studies. Initially determined Hasselmann *et al.*, (1973), the base value of 0.037 was suggested to represent bottom friction under swell wave conditions. Later studies such as (Bouws *et al.*, 1983) revealed that for fully developed wind sea states the a value 0.067 should be chosen. This provided a range between which I attempted to calibrate the model. The final model uses a 0.06 bottom friction coefficient which is meant to represent a wave climate that is in between these two state but has a tendency to be more local wind driven. Using this reasonably accurate result are obtained although inaccuracies at low water level do suggest that this value may be too high. It is possible that a smaller value is more appropriate for this region. However, the wave climates are rarely solely swell, or wind driven, selecting a bottom roughness value is therefore much more complex as it depends on many more factors such as bed material characteristics. The result determined using 0.06 were reasonable and therefore the bottom roughness value is deemed acceptable. It is also worth noting that the region showed a low sensitivity to bottom roughness, therefore it is more prudent to simply choose a reasonable value that generally represents the sea state and use other parameters to calibrate the model such as the breaker parameter.

Use of Delft 3D Current Velocities

The formulation of the Reynolds number used the current velocities provided by the Delft 3D model under base conditions. The base conditions mean that there is no inclusion of vegetation in the domain, therefore any reduction in velocity by vegetation is not included. The reason for choosing the delft 3D current velocity mainly due to lack of filed data providing this information. In reality of the presence of vegetation does not simply dissipate energy, it also alters the flow of water through the vegetation field. In the field the variation of vegetation characteristics across the marsh can change velocities profiles, not only in the horizontal direction but also in the vertical direction as discussed in (NEUMEIER and AMOS, 2006). Neumeier et al. (2006) showed that vegetation height (emerged and submerged) and density change the velocity reduction trends across eh water column, with velocities changing linearly

when exposed to emergent vegetation and changing logarithmically when exposed to submerged vegetation. It was also shown that vegetation can increase velocities close to the bed due to vertical variation in density. What this shows is the complexity of flow patterns across the salt marsh. Without the presence of field data, the delft 3D current velocities were chosen for simplicity, the results showed that these velocities were appropriate for this analysis but more detailed field data would be valuable for further analysis on this matter.
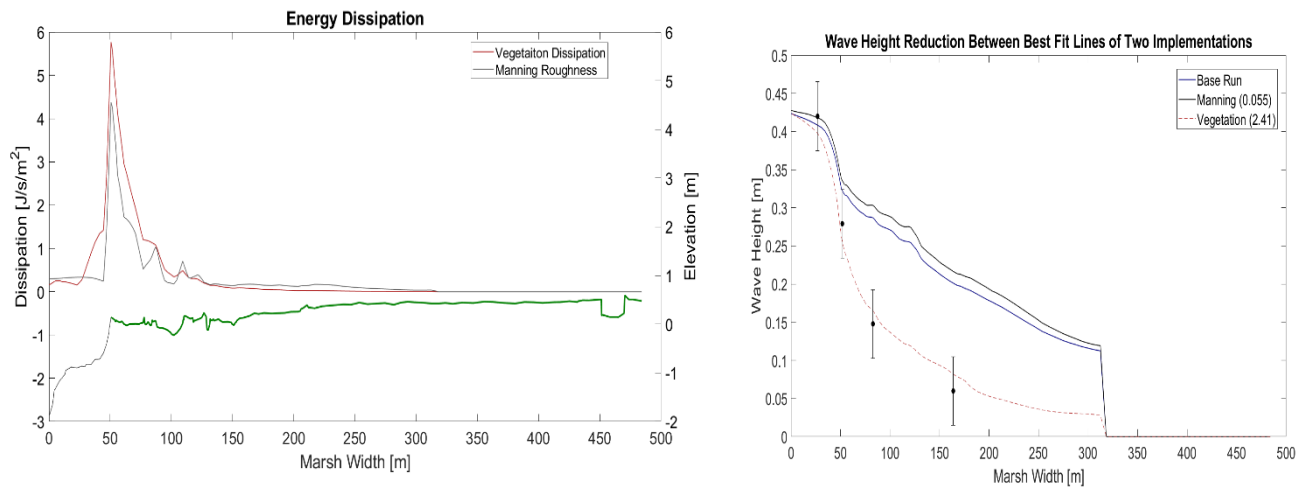
Implementation of Constant Vegetation

In this model, the vegetation is implemented using constant values for all vegetation characteristics which was determined by averaging observed values. This is not completely representative of the real-world conditions, where vegetation height, density, diameter, and health all vary based on a number of environmental factors. A change in any of these characteristics can lead to a variation in energy dissipation or unrealistic magnitudes for other characteristics such as drag coefficient during model calibration (leading to under or over estimation of their influence on wave dissipation). The implementation of Drag forcing in the model is carried out through a constant drag coefficient using the vegetation command in SWAN. This approach was chosen due to the uncertainty behind selection of a proper drag coefficients for marshland. The field surveys allowed for the selection of realistic vegetation characteristics, which should minimize the over or underestimation of the drag coefficient. SWAN does, however, allow for the horizontal variation of vegetation through the plant density using the NPLANTS command. This was not done due to time constraints but merits assessments to determine the level of over or under estimation of the drag coefficient. This may also shed light on the merits of implementing variations of other vegetation characteristics. It is also worth noting that the nonuniformity of these characteristics from season to season may make such variation in vegetation characteristics less applicable in an engineering sense. Meaning that one winter profile is not identical to another winter profile, it may make more sense to choose observed values for given characteristics that perform the worst and best and use them to determine ranges of dissipation for given vegetation types. The use of variable characteristics would only be useful for model validation.

Implementation of Constant Drag Forcing

The constant drag coefficients are determined using varied current velocities throughout the marsh to determine which drag coefficient formulation fits the best. The use of these varied current velocities indicates that the Reynolds number and the drag coefficients by relation, vary along the marsh. This relationship is ignored in the model since there is currently no varied drag coefficient implemented in SWAN. Though the average drag coefficient represents that overall wave height reduction reasonably well, its sudden dissipation of waves seen at 310 meters in Figure 40 is most likely not accurate (no field data was available to determine the validity of the model at the end of the marsh). If field data indicates a more gradual reduction of wave heights until this point, possibly creating a profile that fits minimum velocity wave heights, than varied drag coefficient are most likely the most appropriate way of recreating wave height dissipation. However, like the varied vegetation implementations, it is likely that

the same current velocities are not present for everyone storm on the marsh. Therefore, implementing this in engineering would likely require a range of drag coefficients determined by current velocities observed for different storms. This would likely need to be taken a step further, with and assessment of how the vegetation effects the current velocities, giving not only a range of expected wave height and energy dissipation but also current velocity reduction due to vegetation.

7. Conclusion

Figure 40 summarizes the results. Showing the wave energy dissipation on the left and the wave height reduction on the right. The manning roughness and vegetation labels in the legend represent the two different implementations, while base represent the no vegetation scenario.

7.1. Answering the Research Questions

In general, the Explicit Vegetation dissipation implementation shows more proficiency in recreating the dissipation rates across the salt marsh. The results validate the conclusions of Keefer et al. (2017) and Smith et al. (2014).

1. *To what extent does Delft 3D and SWAN accurately predict the wave conditions present at the east shore site both regionally and locally?*

The regional model was able to appropriately recreate all storms of significance from September 24th to October 2nd. The resulting wave climates were validated by offshore buoys provided by the NOAA, showing an 80% correlation between waves heights and a 95 % correlation between water levels. Both wave heights and water level results show a normalized root mean square error lower than 12%. The prevailing wave direction also matched observational data, though the correlation was low because the wind data produced constant forcing at six-hour interval. The model created the swell and locally dominated wind wave climate present during this time. The 1.2 meters surge was also properly recreated during this time, however the model showed difficulty in creating the surge caused during hurricane Joaquin. The model also showed difficulty recreating the peak periods at the buoys even though the trend is followed, indicating either possible issues in the meteorological file or model setup. However, the other results showed the wave heights and water levels could still be analyzed.

The domain decomposition model was able to recreate key ebb and flow patterns present in the east shore region. It showed a contribution from the South Bay basin to the north of the study

site during the ebb tidal cycle, indicating an area for future study. The model also revealed a wave climate that is minimally impacted by bottom friction, reinforcing conclusions by (Massel, 1996) and (Nelson, 1994). The domain decomposition model is able to recreate the significant wave heights at sensor one with an 86 % correlation and an error of 18%. The water levels are 98% correlated to the filed data with a 15% error.

The SWAN standalone model showed much better results using the explicit vegetation dissipation implementations. While the vegetation does reduce the initial the correlation at the first the sensor to 73%, the three other sensors show correlations above 95 percent with an error below 12%.

2. *What Drag coefficients formulation most accurately recreate energy dissiptaion at the easthshore site?*

Jadhav and Chen (2012), Anderson and Smith (2014) and Mendez and Losada (1999) were all tested using the cross shore current velocities and their relationship to the Reynolds number. The peak mean and minimum current velocities were all assessed for the three drag force formulations. The peak and minimum current velocities both overestimate and under estimated wave dissipation over the majority of the vegetated foreshore respectively. Understandably the max velocities are more accurate at the leading edge of the foreshore while the minimum velocities are more accurate near the back. This indicates that the explicit representation may benefit from implementation of a varied drag coefficient based on current velocities or Reynolds numbers. The results showed that for this wave climate the Jadhav and Chen (2012) and Mendez and Losada (1999) showed the closest correlation, with the Jadhav and Chen (2012) formula fitting the best. This formulation produced a drag coefficient of 2.41 for and average current velocity of 0.29 m/s.

3. *How are the key physical differences between the implicit manning roughness approach and explicit vegetation dissipation approach shown in the model results?*

The biggest difference between the two representations are the way in which they are implemented into the model. Because the manning roughness is implemented as a bottom friction, its influence is only felt at the boundary layer of the water column. In this wave climate, where bottom friction is not as influential as depth induced breaking, the manning roughness has much less effect of an impact on wave energy dissipation than the explicit vegetation dissipation representation. The relationship is clear when comparing the dissipation between the two implementations. Looking at the distribution of influence from different breaking mechanisms the exclusion of drag leads to an increase in depth induced breaking particularly at the breaker zone as seen in Figure 38. The implementation of drag reduces this depth induced breaking, causing the dominant form of dissipation by vegetation. The increased dissipation by vegetation showed and increased refraction of incoming wave. The vegetation not only impacts the energy but also reduces wave velocities as they propagate across the

foreshore. The reason that the explicit implementation is more effective at representing vegetation is because it simulates the effective surface area of the vegetation, allow for the entire water column to experience the drag force as oppose the just the boundary layer of the water column.

7.2. Topics of Interest

This section proposes key areas of interest branching off from the results of this study. The topics address some uncertainties discussed in chapter six such as the spectral inaccuracies as well as next steps in assessment of the East shore Site. These topics are proposed through a series of research objectives and questions as well as a description of the research process for each topic. This topic includes assessment of different storm events and implementation of Varied Drag Coefficients.

Test methodology on other storms

> *Primary Objectives:*
> Determine whether the models used in this study can consistently recreate accurate representations of other storms for a varying intensities and characteristics.
> *Research Questions:*
>   1.   Is the model able to recreate other storms with minimal changes to existing variables?
>   2.   If changes are needed, what are they and for what reason?
>   3.   How do wave dissipation processes change with varied storm conditions?

George Mason University has access to more storm data that can be applied to the Delft 3D+SWAN model to validate the methodology used in this paper for different forcing conditions. To this would simply require the implementation of different meteorological files into the domain decomposition model. Like this study the resulting wave climates produced by the model are then compared to the sensor one field data, indicating the correlation and root mean squared error of the model. Conducting this for multiple storms will create a robust validation for the Delft 3D+SWAN model.

From these validations the boundary conditions produced by the Domain Decomposition model are implemented into the SWAN standalone model where an assessment of wave dissipation is carried out. The multiple storms allow for an overall profile of the expected wave dissipation by the East Shore saltmarsh to be produced. The value of this research strongly depends on the type of storm data available. Ideally the storm data varies greatly in water levels and wave heights, allowing for a wider range of comparison between other saltmarsh studies. This also creates a robust wave dissipation profile for spartina alterniflora under several storm conditions

Varied Drag Coefficients

Primary Objectives:
Implement varied drag forcing into SWAN using the three drag formulations used in this study.

Research Questions:
1. How can varied drag forcing be implemented into the SWAN stand alone model?
2. Is the varied drag coefficient more or less accurate than the constant drag coefficient used in this study?
3. Is Jadhav and Chen (2012) still the most appropriate drag coefficient formulation for this

In the field, the drag coefficient is not constant throughout any marsh. Current velocities are affected by several factors that vary the speed as the wave propagates onshore. Therefore, recreating real world conditions would require the implementation of varied drag coefficients. For this site the Jadhav and Chen formulation has shown to consistently produce the best fitting wave height dissipation profile compared to the Mendez and Losada (1999) and Anderson and Smith (2014). This formulation is therefore used as a starting point in the implementation of varied drag coefficient into the SWAN standalone model. To change the drag coefficient, the source code of the program would need to be altered to incorporate a drag coefficient determined by formulas as opposed to user provided values. This can be done using horizontally varying current velocity input grids and the implementation of Reynolds numbers as well as the Jadhav and Chen drag formulation computation.

Multiple drag formulations can be implemented and tested for accuracy, shedding light on which formulations provides the best overall representation of the change in dissipation rates over the length of the marsh. The difference between constant drag formulations and varied drag formulation should also be assessed to determine whether the increase accuracy is significant enough to merit alteration of the source code.

7.3. Next Steps

The continuation of this topic would first require assessing the cause of the spectral inaccuracies observed in the model. The following next steps primarily center around this objective being that this is the biggest limitation to more detailed assessment of wave propagation across the marsh.

The question of when the manning coefficient loses its applicability is partially addressed in this paper. In appendix C the results of the SWAN standalone model is shown for multiple day during the September 24th to the October 2nd time period. This data varies based on the different manning implementations as well as wave heights and water levels. From this appendix the reduction in wave heights and water levels reduce the deviation between the manning

roughness and the explicit implementation. This seemingly matches the assumption made by Smith et al, (2016) who suggested that the manning roughness is more appropriate for thin water layers. Furthermore, in appendix C.5 is a figure indicating the impact of wave height reduction in relation to vegetation height. The vegetation height is initially reduced to the lowest observed height, then continually reduced until the profiles between the implicit and explicit implementation match up. This brief analysis is an initial indication of where the manning coefficient performs the best. The assumption here, is that the manning coefficient performs better in situations where vegetation characteristics are more closely related to vegetation seen in channels. Conducting analysis such as this but selecting characteristics that fit vegetation cover in open channels or even on dikes may lead to the conclusion that the manning roughness coefficient is only applicable for vegetation that reach a height, density, or diameter. The accuracy of the manning coefficient may also be partially dependent on the relation between vegetation height and water depth. Conducting this assessment would round out the research and would be a good next step that directly branches off the work done here.

It would also be beneficial to determine the cause of the regional model's underestimation of observed peak periods. As stated in the discussion the bottom friction and breaker parameter had little to no effect on the results at the deep-water buoys. However, the resolution of the computational grid can be further reduced to fit the minimum resolution of the GEBCO data. If this does not impact the results of the model, then the meteorological file needs to be checked. Garzon et al, (2017) conducted an analysis on this meteorological file along with a group of other files. GMUs choice to provide the ECMWF file is based on the conclusion of this report which concluded that the ECMWF file performed the best in recreating water levels in the Chesapeake Bay region. However, in general all the models underestimated the wind speed in the region. This underestimation may very well contribute significantly to the inaccuracies at the buoys and should be addressed. Combining this with the 6-hour temporal resolution may contribute significantly to the results. Therefore, following the assessment of resolution another assessment of multiple meteorological models for significant wave heights in terms of their modeled winds and spatial resolutions would be a good second step. It may be that the models do not resolve the storms accurately enough to appropriately recreate periods and the resulting spectra in this region. It is also worth noting that a wind drag coefficient was increased from 0.003 to 0.004 but showed no change in the results (see appendix D.5). At this point it may be necessary to explore other means of determining boundary conditions in the region. Once an accurate wave spectrum is developed, more detailed studies on energy transformation in the region can be conducted from points of generation to points of complete dissipation. A study such as this would show the types of wave energy penetrating inlet and reaching the marsh.

Once an accurate wave spectrum has been developed, a more detailed analysis regions contributing to the flow at the research site such as the South Bay, which contains a significant amount of vegetated marsh land that can influence the flow. The development of such a model would require field data to validate the results. In terms of bathymetry Digital elevation model data has a spatial resolution between 10-30 meters which is more than enough to resolve any

significant bathymetric features. In this case the bathymetric feature in this case would be the inlets, the main channels, the barrier islands, and the intertidal marshes. Along with providing a more accurate flow boundary, a study in this region can provide an opportunity to assess energy flow patterns over a large stretches of salt marsh in the region. Combining the implementation of vegetation and accurate spectral energy profiles would also help in determining larger scale energy transfer trends.

7.4. Concluding Remarks

In general, there was a distinct underperformance by the implicit manning roughness approach when compared to the Explicit vegetation dissipation approach. The lack of Drag force implementation handicaps the ability of the manning coefficient to recreate observed wave climates over saltmarshes. It is possible that there are conditions where the implicit approach is more applicable, however these conditions will need to be determined through further research. The work done in this paper is a first step in a wide range of analysis that can be carried out in this region. This type of analysis helps shed light on the uncertainties of saltmarsh modeling while contributing to a robust knowledge base that is needed to improve Building with Nature methods.

Bibliography

Anderson, M. E. and Smith, J. M. (2014) 'Wave attenuation by flexible, idealized salt marsh vegetation', *Coastal Engineering*, 83, pp. 82–92. doi: 10.1016/j.coastaleng.2013.10.004.

Arcement, G. J. and Schneider, V. R. (1989) 'Guide for Selecting Manning's Roughness Coefficients for Natural Channels and Flood Plains'. Available at: http://dpw.lacounty.gov/lacfcd/wdr/files/WG/041615/Guide for Selecting n-Value.pdf (Accessed: 27 March 2018).

Barber, N. F. and Ursell, F. (1948) 'The Generation and Propagation of Ocean Waves and Swell. I. Wave Periods and Velocities', *Philosophical Transactions of the Royal Society A: Mathematical, Physical and Engineering Sciences*. The Royal Society, 240(824), pp. 527–560. doi: 10.1098/rsta.1948.0005.

Battjes, J. A. and Janssen, J. P. F. M. (1976) 'Energy loss and Set-up due to breaking of Random Waves', p. 19. Available at: http://citeseerx.ist.psu.edu/viewdoc/download?doi=10.1.1.454.5806&rep=rep1&type=pdf (Accessed: 13 June 2018).

Battjes, J. A. and Janssen, J. P. F. M. (1978) *Energy loss and set-up due to breaking random waves*, *Proceedings of 16th Conference on Coastal Engineering, Hamburg, Germany, 1978*. Delft: Council on Wave Research, the Engineering Foundation. Available at: https://repository.tudelft.nl/islandora/object/uuid%3A2fba43fe-f8bd-42ac-85ee-848312d2e27e (Accessed: 11 February 2018).

Bertotti, L. and Cavaleri, L. (1994) 'Accuracy of Wind and Wave Evaluation in Coastal Regions'. Available at: https://icce-ojs-tamu.tdl.org/icce/index.php/icce/article/viewFile/4945/4625 (Accessed: 28 February 2018).

Bouws, E. *et al.* (1983) 'On the Balance Between Growth and Dissipation in an Extreme Depth-Limited Wind-Sea in the Southern North Sea', *Journal of Physical Oceanography*, 13(9), pp. 1653–1658. doi: 10.1175/1520-0485(1983)013<1653:OTBBGA>2.0.CO;2.

Bretschneider, C. L. (1952) 'THE GENERATION AND DECAY OF WIND WAVES IN DEEP WATER', *Transactions*. American Geophysical Union, 33(3). Available at: https://agupubs.onlinelibrary.wiley.com/doi/pdf/10.1029/TR033i003p00381 (Accessed: 9 June 2018).

Bretschneinder, C. L. (1964) *Generation of Waves by Wind State of the Art*, *National Engineering Science Company*. Washington. doi: 10.1017/CBO9781107415324.004.

Bunya, S. *et al.* (2010) 'A High-Resolution Coupled Riverine Flow, Tide, Wind, Wind Wave, and Storm Surge Model for Southern Louisiana and Mississippi. Part I: Model Development and Validation', *Monthly Weather Review*, 138(2), pp. 345–377. doi: 10.1175/2009MWR2906.1.

Cavaleri, L. and Rizzoli, P. M. (1981) 'Wind wave prediction in shallow water: Theory and applications', *Journal of Geophysical Research*, 86(C11), p. 10961. doi:

10.1029/JC086iC11p10961.

Collins, J. I. (1972) 'Prediction of shallow-water spectra', *Journal of Geophysical Research*, 77(15), pp. 2693–2707. doi: 10.1029/JC077i015p02693.

Dalrymple, R. A. *et al.* (1984) 'WAVE DIFFRACTION DUE TO AREAS OF ENERGY DISSIPATION', *ASCE*. Available at: https://ascelibrary.org/doi/pdf/10.1061/%28ASCE%290733-950X%281984%29110%3A1%2867%29 (Accessed: 21 February 2018).

Dietrich, J. C. *et al.* (2011) 'Hurricane Gustav (2008) Waves and Storm Surge: Hindcast, Synoptic Analysis, and Validation in Southern Louisiana', *Monthly Weather Review*, 139(8), pp. 2488–2522. doi: 10.1175/2011MWR3611.1.

Engquist, B. and Majda, A. (1977) 'Absorbing Boundary Conditions for the Numerical Simulation of Waves', *Mathematics of Computation*, 31(139), pp. 629–651. Available at: http://www.jstor.org/stable/2005997 (Accessed: 23 June 2018).

Garzon, J. L., Ferreira, C. M. and Padilla-Hernandez, R. (2018) 'Evaluation of weather forecast systems for storm surge modeling in the Chesapeake Bay', *Ocean Dynamics*, 68(1), pp. 91–107. doi: 10.1007/s10236-017-1120-x.

Hallegatte, S. *et al.* (2013) 'Future flood losses in major coastal cities', *Nature Climate Change*, 3, pp. 802–806. doi: 10.1038/NCLIMATE1979.

Hasselmann, K. *et al.* (1973) 'Measurements of wind-wave growth and swell decay during the Joint North Sea Wave Project (JONSWAP)', *Ergänzungsheft 8-12*. Deutches Hydrographisches Institut. Available at: https://repository.tudelft.nl/islandora/object/uuid:f204e188-13b9-49d8-a6dc-4fb7c20562fc/?collection=research (Accessed: 10 February 2018).

Jadhav, R. S. and Chen, Q. (2012) 'FIELD INVESTIGATION OF WAVE DISSIPATION OVER SALT MARSH VEGETATION DURING TROPICAL CYCLONE', *Coastal Engineering Proceedings*, 1(33), p. 41. doi: 10.9753/icce.v33.waves.41.

Keefer, M. N. (2017) 'Wetlands as a nature-based flood defense : Numerical modeling of wave attenuation by vegetation in coastal New Jersey Documentation & Supplemental Information'.

Kim, T.-H. *et al.* (2011) 'Validation of global ocean tide models using the superconducting gravimeter data at Syowa Station, Antarctica, and in situ tide gauge and bottom-pressure observations', *Polar Science*. Elsevier, 5(1), pp. 21–39. doi: 10.1016/J.POLAR.2010.11.001.

Kobayashi, N., Raichle, A. W. and Asano, T. (1993) 'WAVE ATTENUATION BY VEGETATION', *ASCE*. Available at: https://ascelibrary.org/doi/pdf/10.1061/%28ASCE%290733-950X%281993%29119%3A1%2830%29 (Accessed: 21 February 2018).

Komen, G. J. *et al.* (1994) *Dynamics and modelling of ocean waves*. Cambridge University Press.

Madsen, O. S., Poon, Y.-K. and Graber, H. C. (1988) 'Spectral Wave Attenuation by Bottom Friction: Theory', *Coastal Engineering Proceedings*. Council on Wave Research, the

Engineering Foundation, 1(21). Available at: https://icce-ojs-tamu.tdl.org/icce/index.php/icce/article/view/4241/3922 (Accessed: 26 February 2018).

Madsen, O. S. and Rosengaus, M. M. (1988) 'Spectral Wave Attenuation by Bottom Friction : Experiments', *Coastal Engineering Proceedings*. Council on Wave Research, the Engineering Foundation, 1(21). Available at: https://icce-ojs-tamu.tdl.org/icce/index.php/icce/article/view/4270/3951 (Accessed: 21 February 2018).

Massel, S. R. (1996) 'On the largest wave height in water of constant depth', *Ocean Engineering*. Pergamon, 23(7), pp. 553–573. doi: 10.1016/0029-8018(95)00049-6.

McKee Smith, J., Anderson Bryant, M. and Wamsley, T. V (2016) 'Wetland buffers: numerical modeling of wave dissipation by vegetation'. doi: 10.1002/esp.3904.

Mendez, F. J. and Losada, I. J. (2004) 'An empirical model to estimate the propagation of random breaking and nonbreaking waves over vegetation fields', *Coastal Engineering*. Elsevier, 51(2), pp. 103–118. doi: 10.1016/J.COASTALENG.2003.11.003.

Méndez, F. J., Losada, I. J. and Losada, M. A. (1999) 'Hydrodynamics induced by wind waves in a vegetation field', *Journal of Geophysical Research: Oceans*, 104(C8), pp. 18383–18396. doi: 10.1029/1999JC900119.

Miche, M. (1944) 'Mouvements ondulatoires de la mer en profondeur constante ou décroissante', *École nationale des ponts et chaussées*. École nationale des ponts et chaussées, 3, pp. 369–406. Available at: https://repository.tudelft.nl/islandora/object/uuid:6fceef55-d71b-4e3e-a94f-98ff17cb8f91?collection=research (Accessed: 23 February 2018).

Murty, T. S., Flather, R. A. and Henry, R. F. (1986) 'The Storm Surge Problem in the Bay of Bengal', *Pergamon Journals Ltd.* , 16, pp. 195–233. Available at: https://ac.els-cdn.com/007966118690039X/1-s2.0-007966118690039X-main.pdf?_tid=6f213772-188c-11e8-9203-00000aacb362&acdnat=1519385396_9b17fe898798d40bb7b97a80808ec468 (Accessed: 23 February 2018).

Nederhoff, K., Van Dongeren, A. and Van Ormndt, M. (2014) *Validation Cases - Delft Dashboard - Deltares Public Wiki*. Delft. Available at: https://publicwiki.deltares.nl/display/DDB/Validation+Cases?preview=/77238017/127633271/1201428-000-ZKS-0011-r-Delft Dashboard_final.pdf (Accessed: 13 June 2018).

Nelson, R. C. (1994) 'Depth limited design wave heights in very flat regions', *Coastal Engineering*. Elsevier, 23(1–2), pp. 43–59. doi: 10.1016/0378-3839(94)90014-0.

Neumann, B. *et al.* (2015) 'Future Coastal Population Growth and Exposure to Sea-Level Rise and Coastal Flooding - A Global Assessment'. doi: 10.1371/journal.pone.0118571.

NEUMEIER, U. and AMOS, C. L. (2006) 'The influence of vegetation on turbulence and flow velocities in European salt-marshes', *Sedimentology*. Wiley/Blackwell (10.1111), 53(2), pp. 259–277. doi: 10.1111/j.1365-3091.2006.00772.x.

Pierson, W. J. and Moskowitz, L. (1964) 'A proposed spectral form for fully developed wind seas based on the similarity theory of S. A. Kitaigorodskii', *Journal of Geophysical Research*, 69(24), pp. 5181–5190. doi: 10.1029/JZ069i024p05181.

Powell, M. D., Vickery, P. J. and Reinhold, T. A. (2003) 'Reduced drag coefficient for high wind speeds in tropical cyclones', *Nature*, 422, pp. 279–283. Available at: https://www.nature.com/articles/nature01481.pdf (Accessed: 5 May 2018).

Putnam, J. A. and Johson, J. W. (1949) 'The dissipation of wave energy by bottom friction', *Transactions, American Geophysical Union*, 30(1), p. 67. doi: 10.1029/TR030i001p00067.

Snyder, R. L. *et al.* (1981) 'Array measurements of atmospheric pressure fluctuations above surface gravity waves', *Journal of Fluid Mechanics*. Cambridge University Press, 102(1), p. 1. doi: 10.1017/S0022112081002528.

Team, S. (2017a) *SWAN: Scientific and technical Documentation*. 1.2. Delft: Delft University of Technology. Available at: http://swanmodel.sourceforge.net/download/zip/swantech.pdf (Accessed: 18 February 2018).

Team, S. (2017b) 'SWAN User Manual', 3(41.20), p. 141.

Tolman, H. L. (1992) 'Effects of Numerics on the Physics in a Third-Generation Wind-Wave Model', *Journal of Physical Oceanography*, 22(10), pp. 1095–1111. doi: 10.1175/1520-0485(1992)022<1095:EONOTP>2.0.CO;2.

Verboom, G. K. and Slob, A. (1984) 'Weakly-reflective boundary conditions for two-dimensional shallow water flow problems', *Adv. Water Resources*, 7, pp. 192–197. Available at: https://ac.els-cdn.com/0309170884900186/1-s2.0-0309170884900186-main.pdf?_tid=9fe80955-d35d-478e-8c63-9b470fd6c9b9&acdnat=1529782783_1481a5b4d0a1e57102f68132accd6cbb (Accessed: 23 June 2018).

Vuik, V. *et al.* (2016) 'Nature-based flood protection: The efficiency of vegetated foreshores for reducing wave loads on coastal dikes', *Coastal Engineering*. Elsevier B.V., 116, pp. 42–56. doi: 10.1016/j.coastaleng.2016.06.001.

Wamsley, T. V *et al.* (2009) 'The potential of wetlands in reducing storm surge', *Ocean Engineering*, 37, pp. 59–68. doi: 10.1016/j.oceaneng.2009.07.018.

Wu, J. (1969) 'Wind stress and surface roughness at air-sea interface', *Journal of Geophysical Research*. Wiley-Blackwell, 74(2), pp. 444–455. doi: 10.1029/JB074i002p00444.

Wu, J. (1980) *Wind-Stress coefficients over Sea surface near Neutral Conditions—A Revisit*, *Journal of Physical Oceanography*. doi: 10.1175/1520-0485(1980)010<0727:WSCOSS>2.0.CO;2.

Wu, J. (1982) 'Wind-stress coefficients over sea surface from breeze to hurricane', *Journal of Geophysical Research*. Wiley-Blackwell, 87(C12), p. 9704. doi: 10.1029/JC087iC12p09704.

Zijlema, M., van Vledder, G. P. and Holthuijsen, L. H. (2012) 'Bottom friction and wind drag for wave models', *Coastal Engineering*. Elsevier, 65, pp. 19–26. doi: 10.1016/J.COASTALENG.2012.03.002.

Appendix A. Literature Review Background information

These appendices address several figures described in the literature review section, providing more detailed description of different figures and methods described in chapter 2. Detail on all the SWAN and Delft 3D are not included because of the amount that would need to be described, for more detail on these refer to the associated technical manual.
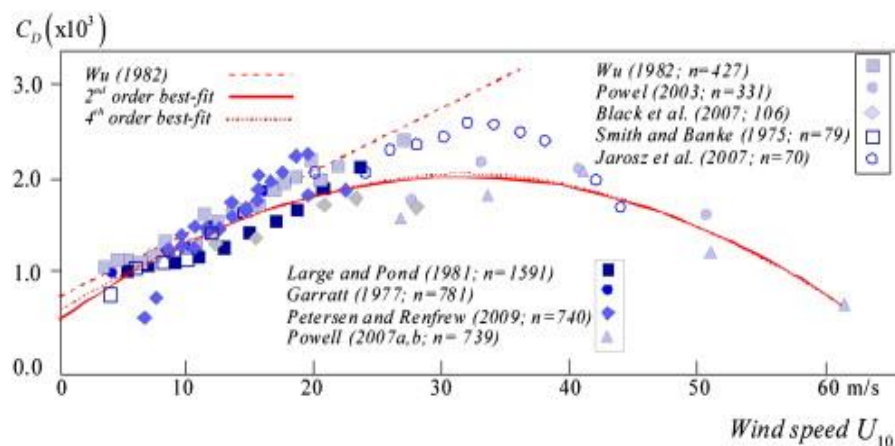

Figure 41 shows the comparison between the Wu drag coefficient formulation and the relationships derived from Zijlema et al (2012)

A.1 Zijlema (2012)

The image is taken from Zijlema et al. (2012) which discusses various relationships between the changing wind speeds and the associated drag coefficients. As discussed in Chapter 2, the Wu1982 formulation has been the accepted wind drag coefficient formulation used by SWAN. This formulation depicts an almost linear relationship between wind speeds and wind drag indicated in the above image by the dashed linear best fit line. The two other lines indicate the second and forth order best fit polynomial lines for the observed field data. The field data was taken from a number field studies each assessing storm data from a number of cases with "n" number of observation points. The studies indicated that the Wu formulation used by other modeling software, often overestimates the drag forcing at higher wind speeds (typically higher then 20m/s). The observations clearly indicate a threshold at which drag forcing no long increases but instead levels out and begins to decrease. The overall field data fits with the

polynomial fitting shown by the solid red lines. Zijlema et al. 2012 used these results formulate a wind drag coefficient that fits with the polynomial fit.
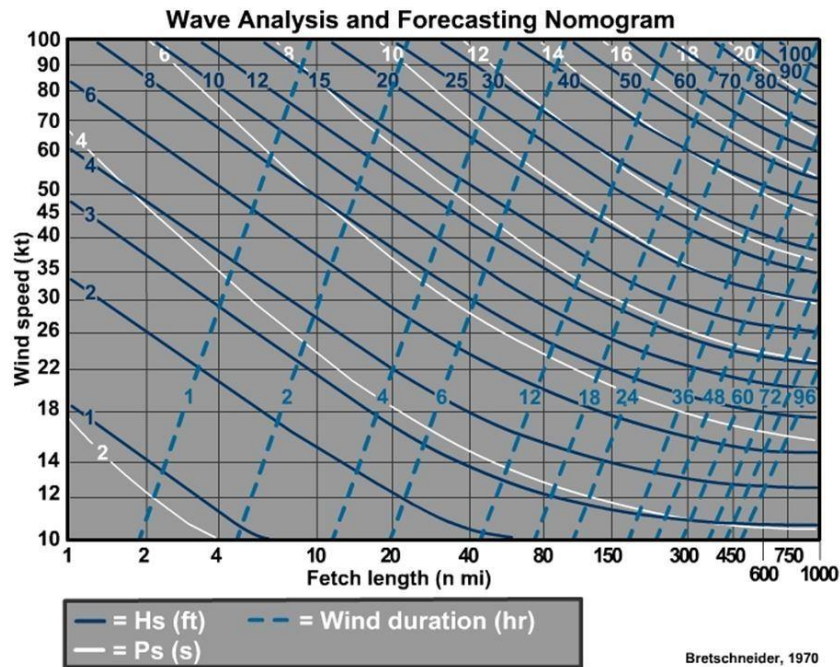
A.2 Bretschneider Diagram

Figure 42 Show the Bershneider diagram depicting the relationship between Wind speed, fetch length, wave height, wave period and sustained wind duration.

This Bretschneider diagram is used to determine characteristics of relevant wave climates as a function of the sustained wind speeds and fetch length. In this paper this diagram is used to help analyze the results of the regional model. The primary purpose of the regional model is to generate the desired wave climates necessary to run the two remaining models. Understanding what storm characteristics are responsible for each part of the observed wave climate helps understand under and over estimation in the validations.

The relationships depicted in this diagram are described in (Bretschneider, 1952) while the original diagram is presented in (Bretschneinder, 1964). Using research on formulation of basic wave characteristics conducted by Sverdrup and Munk (1947) as well as the forecasting methods developed from this paper, Bretschnieder to relate the wave characteristics as a function of wind duration, wind speed and fetch length. The figure shown above is developed through the integration of equation equation 24 resulting in equation 25 which describes the final relationship between duration, speed, and fetch.

$$\frac{gt}{U} = \int \frac{U}{Cg}\left(\frac{gF}{U^2}\right); \ \frac{Cg}{U} = \frac{1}{2} * \frac{C_o}{U}$$

equation 24

$$\frac{tU}{F} = \frac{gt}{U} \Big/ \frac{gF}{U^2}$$

<div align="right">**equation 25**</div>

A.3 Hydraulic Equation for Storm surge

The equations shown below are the depth average motion equations presented by (Murty, Flather and Henry, 1986), to determine storm surge.

$$\frac{\partial u}{\partial t} + u\frac{\partial u}{\partial x} + v\frac{\partial u}{\partial y} - fv = -g\frac{\partial \eta}{\partial x} - \frac{1}{\varrho}\frac{\partial p}{\partial x} + \frac{1}{\varrho h}(\tau_{sx} - \tau_{bx})$$

<div align="right">**equation 26**</div>

$$\frac{\partial v}{\partial t} + u\frac{\partial v}{\partial x} + v\frac{\partial v}{\partial y} + fu = -g\frac{\partial \eta}{\partial y} - \frac{1}{\varrho}\frac{\partial p}{\partial y} + \frac{1}{\varrho h}(\tau_{sy} - \tau_{by}$$

<div align="right">**equation 27**</div>

$$\frac{\partial \eta}{\partial t} + \frac{\partial}{\partial x}(hu) + \frac{\partial}{\partial y}(hv) = 0$$

<div align="right">**equation 28**</div>

Where:

    t = time
    η = elevation of the sea surface
    u, v = components of depth-mean current q
    t_{xx}, t_{yy} = components of the wind stress t_s, on the surface
    t_{bx}, t_{by} = components of the bottom stress t_b
    p = atmospheric pressure on the sea surface
    h = the total water depth (=D+ η where D is undisturbed depth),
    ϱ = the density of the sea water, assumed uniform
    g = the acceleration due to gravity
    f = the Coriolis parameter (=2wsinϕ, where w is the angular speed of the earth's rotation and ϕ latitude).

Equations 26 and 27 for each coordinate, equate the acceleration of the water (on the left) to the forces acting on it (on the right). The difference between the two equations are the components of current velocity and bottom stress they apply. Equation 26 addresses the wind stress at the surface while equation 27 assess the bottom stress. These equations depict the dependency of storm surge on pressure gradients in deep water while wind stress increases in influence in shallow water (as described in chapter 2).

A.4 Choosing Manning roughness values

These two tables indicate n values need to implement manning roughness for both bottom friction and flood plain vegetation. These values along with the process discussed in (Arcement and Schneider, 1989) were used in (Bunya *et al.*, 2010) to determine different manning roughness coefficient values for designated vegetation classes. In this paper the manning roughness values provided by Bunya were used but varied based on the marshland uniformity.

Bottom Roughness (Flood Plain)			
Bed Material	Grain size (mm)	Straight Uniform channel	Smooth Channel
Firm Soil	--	0.025-0.032	0.020
Sand	0.2-2	0.026-0.035	--
Gravel	2-64	0.028-0.035	0.024-0.026
Cobble	64-256	0.030-0.050	--
Boulder	>256	0.040-0.070	--

Table 3 shows the range of manning roughness values for different bed material as a function of grain size and channel uniformity.

Flood-plain conditions		N value adjustment
	Smooth	0.000
Degree of irregularity (n1)	Minor	0.001-0.005
	Moderate Severe	0.011-0.020
Variation of flood-plain cross section (n2)		**0.0**
Flood-plain conditions		**N value adjustment**
	Negligible	0.000-0.004
Effect of obstructions (n3)	Minor	0.005-0.019
	Appreciable	0.020-0.030
	Small	0.001-0.010
	Medium	0.011-0.025
Amount vegetation	Large	0.025-0.050
	Very Large	0.050-0.100
	Extreme	0.100-0.200
Degree of meander (m)		**1.0**

Table 4 shows the manning roughness coefficient assigned to flood planes that can vary based on the amount of vegetation, obstructions, and degree of irregularity.

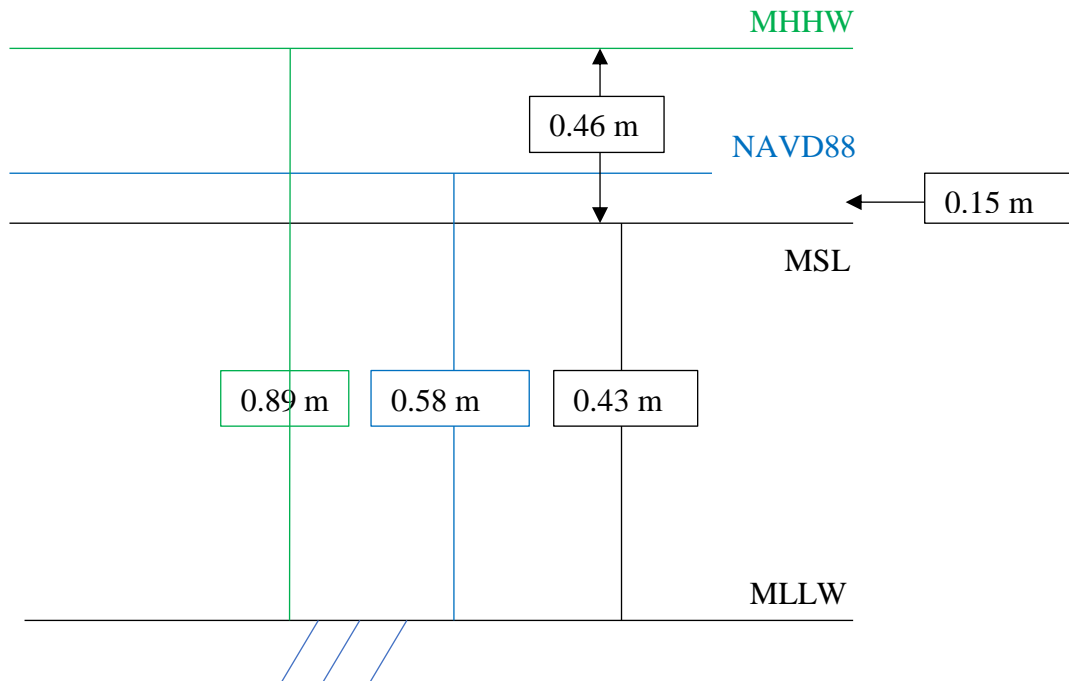# A.5 NOAA datum description

Kiptopeke

Figure 43 shows the vertical datum provided by the NOAA government website.

The figure above shows the relevant vertical datums provided by the NOAA for the Kiptopeke tide station. This tide station is the closest to the research site and therefore more closely resembles site conditions. The NAVD88 datum is the north American vertical datum of 1988. This datum was used in the field data and therefore required conversion if it were to be compared to the model results which were set to mean sea level (MSL). The MHHW vertical datum was used in the Virginia Tsunami Digital Elevation Model. The file was converted to MSL using the value indicated above.

Appendix B: SWAN Input Files

SWAN stand-alone input files are text files that use keywords to indicate to SWAN the kind of actions that need to be taken. These Keywords are described in the SWAN manual; therefore they won't be fully described in detail, in this paper. However, there will be an example of the Command files used, vegetation landcover files, equidistant wind files, computational grid, and bathymetry files. The spectral file is not described because it is completely described in the SWAN user manual.

Appendix B-1: Command Files

Below is the command file used for the base run with the two vegetation implementations commented out:

```
$************************************HEADING***************************************
PROJ 'ES_data' 'R1s'
$
$ PURPOSE OF TEST: Test vegetation implementation of SWAN
$
$************************************MODEL Input***********************************
$
SET LEVEL 0.4912 NOR 0 INRHOG 1 NAUT
COORDINATES SPHE CCM
$
MODE NONSTAT
$
CGRID CURVILINEAR 130 256 CIRCLE 36 0.04 1.0 24
READGRID COORDINATES 1. 'ESsmall.grd' 2 0 1 FREE
$
$
INPGRID BOTTOM CURVILINEAR 0 0 130 256 EXC 999.000
READINP BOTTOM 1.0 'ESsmall.bot' 2 0 FREE
$
WIND 5.1 30 DRAG WU
$
BOU SEG IJ  0 79 0 0 0 130 130 91 VARIABLE FILE &
0.000721 'DDnew.lon5t078.sp2' 1 &
0.000721 '    ' 2 &
0.000721 '    ' 3 &
0.000721 '    ' 4 &
0.000675 '    ' 5 &
0.001183 '    ' 6 &
0.001182 '    ' 7 &
0.001183 '    ' 8 &
0.001183 '    ' 9 &
0.001183 '    ' 10 &
```

```
0.001404 '   ' 11 &
0.000015 '   ' 12 &
0.000008 '   ' 13 &
0.000015 '   ' 14 &
0.000016 '   ' 15 &
0.00 '   ' 16
$
$ OFF QUAD
$
INITIAL ZERO
GEN3 KOMEN AGROW
WCAP KOMEN 2.36E-5 3.02E-3 2. 1. 1.
BREAKING BKD 1.0 0.8 7.59 -8.06 8.09
FRICTION JONSWAP CON 0.038
$
$ FRICTION MAD
$ INPGRID FRICTION REG  -75.975187 37.081324 0 257 176 0.000359 0.000359
$ READINP FRICTION 1 'ManningCover.dep' 2 0 FREE
$
$ VEGETATION 0.5 0.007 496 0.4
$ INPGRID NPLANTS REG -75.968259 37.082757 0 250 299 0.000182 0.000182
$ READINP NPLANTS 1 'ConVeg.dep' 2 0 FREE
$
$*******************************Output_Request*********************************
$
POINTS 'RG1_GPS' FILE 'GPS.txt'
$BLOCK 'RG1_GPS' HEADER 'SWAN_RUN1G.mat' HS WATLEV QB OUT 20150924.000000 10 MI
TABLE 'RG1_GPS' HEADER 'SWAN_RUN1G.tbl' HS DIR TPS DEP DISSIP DISVEG WATLEV
SPEC 'RG1_GPS' SPEC2D ABS 'SWAN_RUN1G_SPEC.txt'
$
POINTS 'RG1_SMGP' FILE 'ESSMALLGRIDPOINTS.txt'
$BLOCK 'RG1_SMGP' HEADER 'SWAN_RUN1SMGP.mat' HS WATLEV QB OUT 20150924.000000 10 MI
TABLE 'RG1_SMGP' HEADER 'SWAN_RUN1SMGP.tbl' HS DIR TPS DEP DISSIP DISVEG WATLEV
SPEC 'RG1_SMGP' SPEC2D ABS 'SWAN_RUN1SMGP_SPEC.txt'
$
POINTS 'R1_SP' FILE 'SP.txt'
$BLOCK 'R1_SP' HEADER 'SWAN_RUN1.mat' HS WATLEV QB OUT 20150924.000000 10 MI
TABLE 'R1_SP' HEADER 'SWAN_RUN1.tbl' HS DIR TPS DEP DISSIP DISVEG WATLEV
SPEC 'R1_SP' SPEC2D ABS 'SWAN_RUN1_SPEC.txt'
$
POINTS 'R1_B' FILE 'changed_boundary.txt'
$BLOCK 'R1_B' HEADER 'SWAN_RUN1B.mat' HS WATLEV QB OUT 20150924.000000 10 MI
TABLE 'R1_B' HEADER 'SWAN_RUN1B.tbl' HS DIR TPS DEP DISSIP DISVEG WATLEV
SPEC 'R1_B' SPEC2D ABS 'SWAN_RUN1B_SPEC.txt'
$
TEST 1,0
COMPUTE STAT 20150920.190000
STOP
$
$*********************************END*********************************************
```

Appendix B-2: Vegetation Implementation and Bathymetry

The base command file does not implement any form of vegetation into the calculations. It applies a constant JONSWAP bottom friction to the entire domain. The three different command files implement the same base input file, but differ in their implementation of bottom roughness or friction.

The vegetation implementations are separated between the implicit manning roughness representation and the explicit vegetation dissipation representation. The manning roughness is outlined by the green box and will replace the "FRICTION JONSWAP CON 0.038" command just above it. This approach takes the manning values and implements them into the Madsen formula, applying a spatially varying manning roughness over the different vegetation classes.

1. "FRICTION MAD" indicated that the Madsen formulation is to be used for bottom friction.

2. "INPGRID FRICTION REG -75.975187 37.081324 0 257 176 0.000359 0.000359" provides the dimensions of the grid, because the command file uses spherical coordinates the dimensions are all given in degrees.

3. "READINP FRICTION 1 'ManningCover.dep' 2 0 FREE" identifies the file that is to be read by SWAN that contains the Manning Cover information. For more detail on the individual command refer to the SWAN manual.

The vegetation dissipation approach is outlined in orange. This approach separated the influence of the bed and the vegetation. Therefore in this representation the JONSWAP bottom friction in still utilized, and the VEGETATION and NPLANT command are used to describe the vegetation.

1. "VEGETATION 0.5 0.007 496 0.4" indicates that vegetation is to be implemented into the SWAN model using the given vegetation characteristics.

2. "INPGRID NPLANTS REG -75.968259 37.082757 0 250 299 0.000182 0.000182" indicates the vegetation landcover grid dimensions.

3. "READINP NPLANTS 1 'ConVeg.dep' 2 0 FREE" indicates what file should be read and how it should be read.

The Vegetation implementation files and the computation grid files have the same format, however the computational grid contains both the x and y coordinates whereas the vegetation files only contain 1 variable. It is therefore necessary to indicated which block identifies the x and y coordinates in the computational grid. An example of this command file is shown below.
x-coordinates

```
 -75.967170   -75.967114   -75.967057   -75.967001   -75.966945   -75.966889
 -75.966832   -75.966776   -75.966720   -75.966663   -75.966607   -75.966551
 -75.966495   -75.966438   -75.966382   -75.966326   -75.966270   -75.966213
 -75.966157   -75.966101   -75.966044   -75.965988   -75.965932   -75.965876
```
…

…

y-coordinates

37.125028	37.125029	37.125029	37.125030	37.125030	37.125031
37.125031	37.125031	37.125032	37.125033	37.125033	37.125033
37.125034	37.125034	37.125035	37.125035	37.125036	37.125036

…

The due to the size, what is shown above is not the complete file, but it shows the general structure. Each block of data indicates a row of coordinates. They this file can start at the bottom left corner or top right corner depending on the set up. The vegetation files have no variable indicators but follow the same principle.

The bathymetry file is similar to the vegetation file except the first row of the coordinates in the file indicate the first row of coordinates of the map.

Appendix B-3: Equidistant wind file

The equidistant wind file were created extract the necessary information from the fort.22 file that was provided by GMU. Equadistant grids are grids of equivalent spacing that apply a single variable to the computational grid. The fort.22 file contains the wind speed in the x and y direction as well as the pressure during that time. These files are both temporally and spatially variant, with each block indicating a new time. For this paper the three files were created, .amu, .amv and .amp (wind in the x direction, wind in the y direction, and pressure). The format is shown below:

```
***********************************START***************************************
### START of HEADER
### This file is created by Deltares                    $ Comments such as these indicate the beginning
                                                         and end of the header section

### Additional comments
FileVersion      = 1.03
Filetype         = meteo_on_equidistant_grid            $ Indicating the type of files
n_cols           = 277                                  $ Number of columns per block
n_rows           = 284                                  $ Number of rows per block
grid_unit        = degree                               $ Grid units degree is spherical coordinate system
x_llcenter       = -98.86                               $ Center of lower left cell
dx               = 0.141                                $ Size of a single cell in x direction
y_llcenter       = 6.836                                $ Center of lower left cell
dy               = 0.141                                $ Size of single cell in y direction
NODATA_value     = -999.000                             $ No data value
n_quantity       = 1                                    $ Number of variables described in block
quantity1        = x_wind                               $ Name of variable
unit1            = m s-1                                 $ Variable units
### End OF HEADER
TIME =  0.0 minutes since 2015-09-20 18:00:00 +00:00                  $ First time interval
1.2      0.8      0.6      0.7      0.8      0.7      0.6      0.5      0.4 …          $ Variable input
TIME = 360.0 minutes since 2015-09-20 18:00:00 +00:00                $ Second time interval
1.2      0.8      0.6      0.7      0.8      0.7      0.6      0.5      0.4 …
**********************************END********************************************
```

All of these files are tab delimited and have their commands or keywords completely described in the Delft 3D manual.

Appendix C: Wave Height Dissipation Profiles

The figures of this section are wave height dissipation profile for high water periods between September 25th to September 30th for different manning roughness coefficient values from 0.35 to 0.8. The associated water levels are shown in the figure below. There are three drag coefficients shown below, all calculated using the mean current velocities for each point in time. The Reynolds numbers, average velocity and associated drag coefficients are shown in the table below.

Date	Mean Current Velocity	Reynolds Number	Mendez and Losada (1999)	Anderson and Smith (2014)	Jadhav and Chen (2012)
Sept. 25	0.1471	644.34	14.98	1.96	4.39
Sept. 26	0.2396	1049.52	5.17	1.40	2.83
Sept. 27	0.2893	1267.23	3.44	1.26	2.41
Sept. 28	0.2627	1150.71	4.24	1.33	2.61
Sept. 29	0.2602	1139.76	4.32	1.34	2.64
Sept. 30	0.2765	1211.16	3.79	1.29	2.50

Table 5 shows the velocities, Reynolds numbers and the drag coefficients calculated for 6 different periods in time.
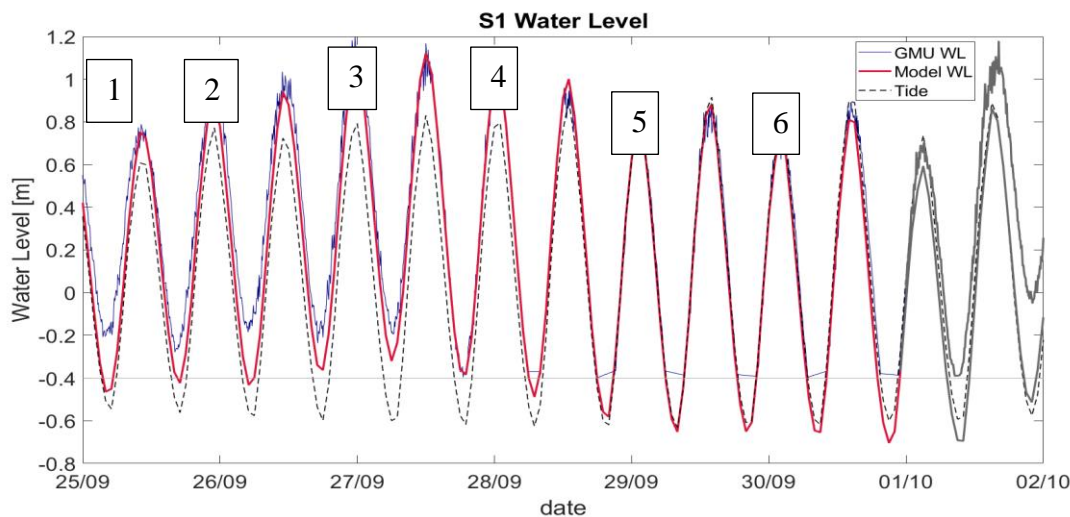
Figure 44 this imageis used to indicate atwhat points the dates were selected.

Appendix C.1
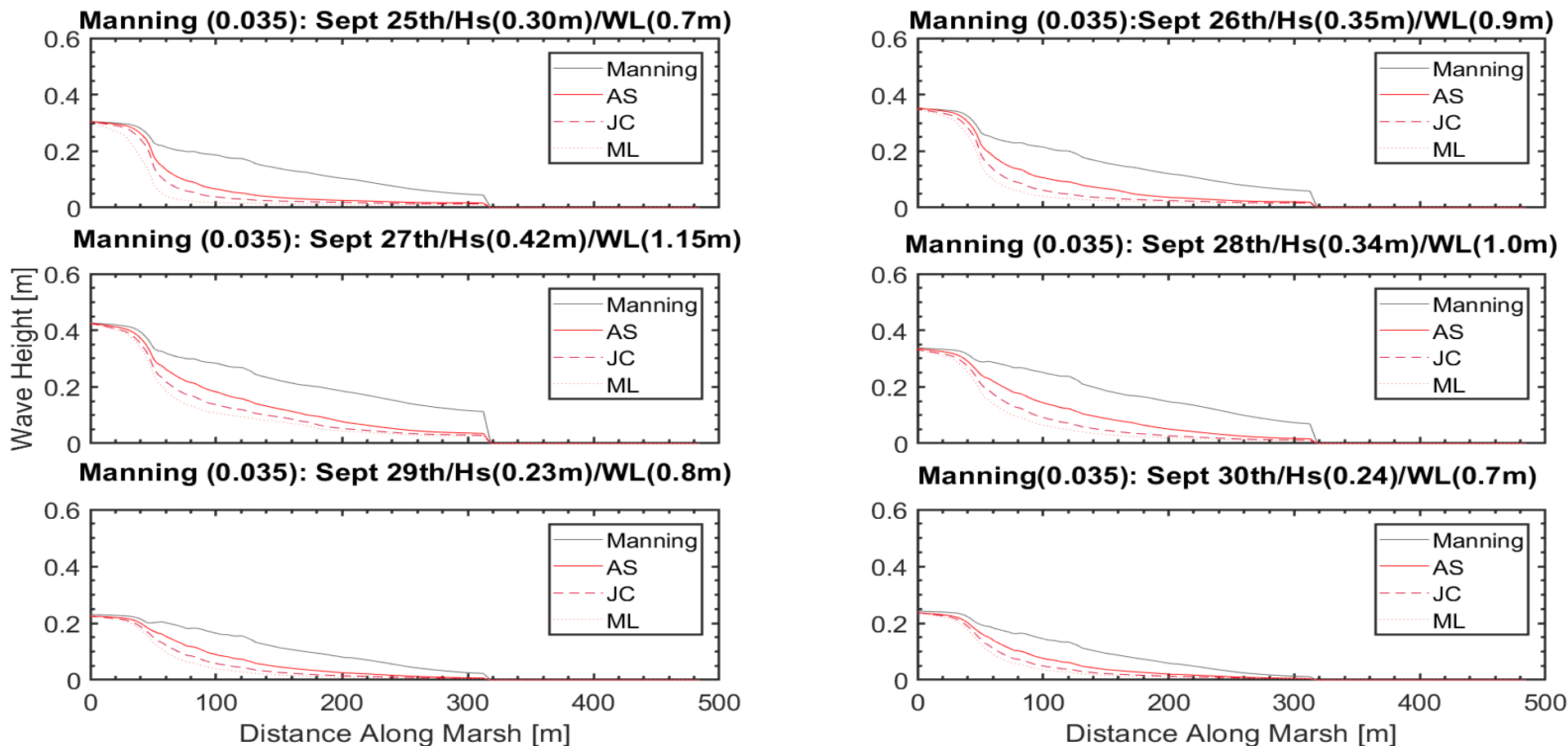
Figure 45 shows the *wave* height reduction profile for the manning 0.035 for each day from sept.25th to Sept. 30th.

Appendix C.2
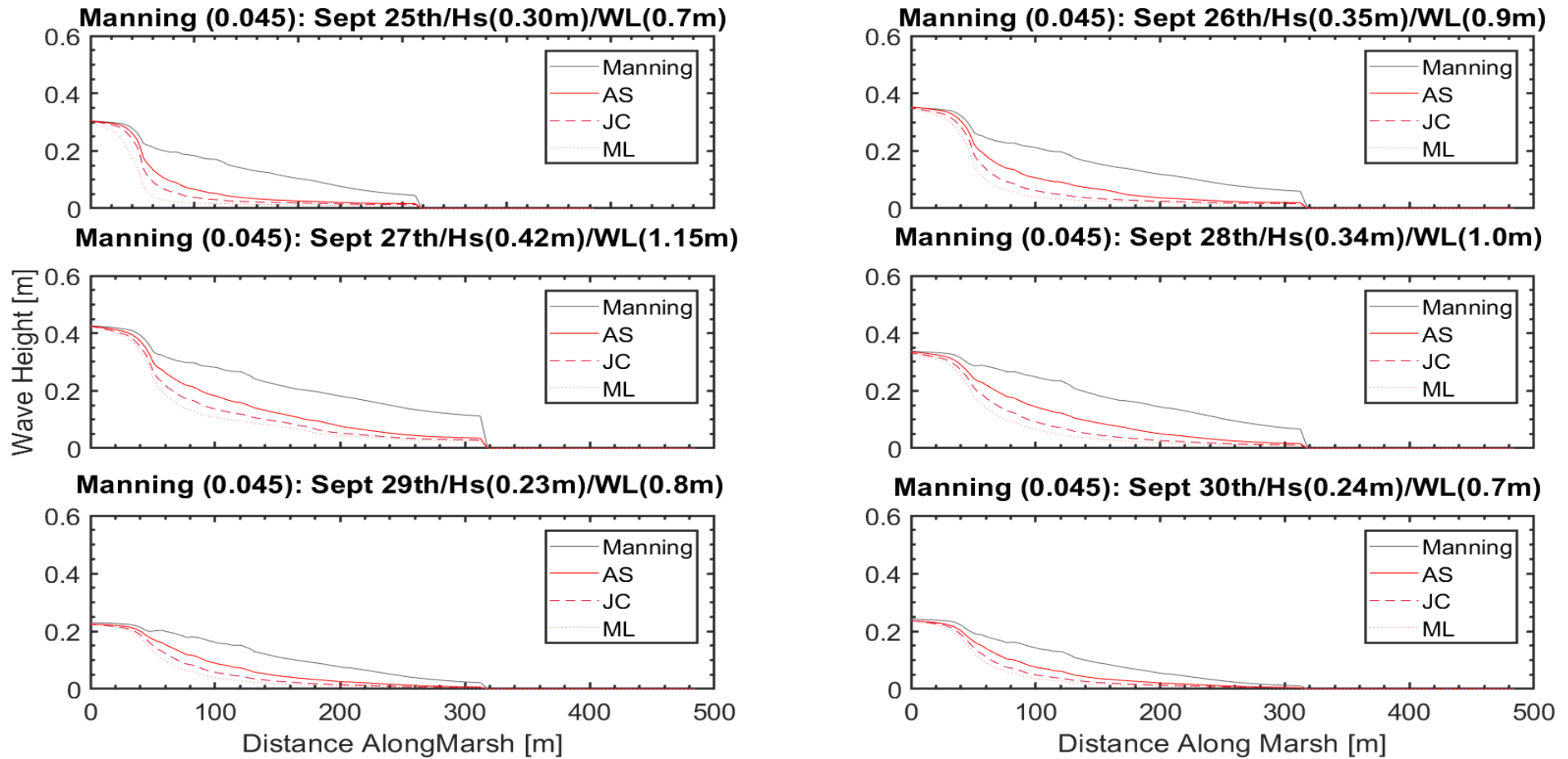
Figure 46 shows the wave height reduction profile for the manning 0.045 for each day from sept.25th to Sept. 30th.
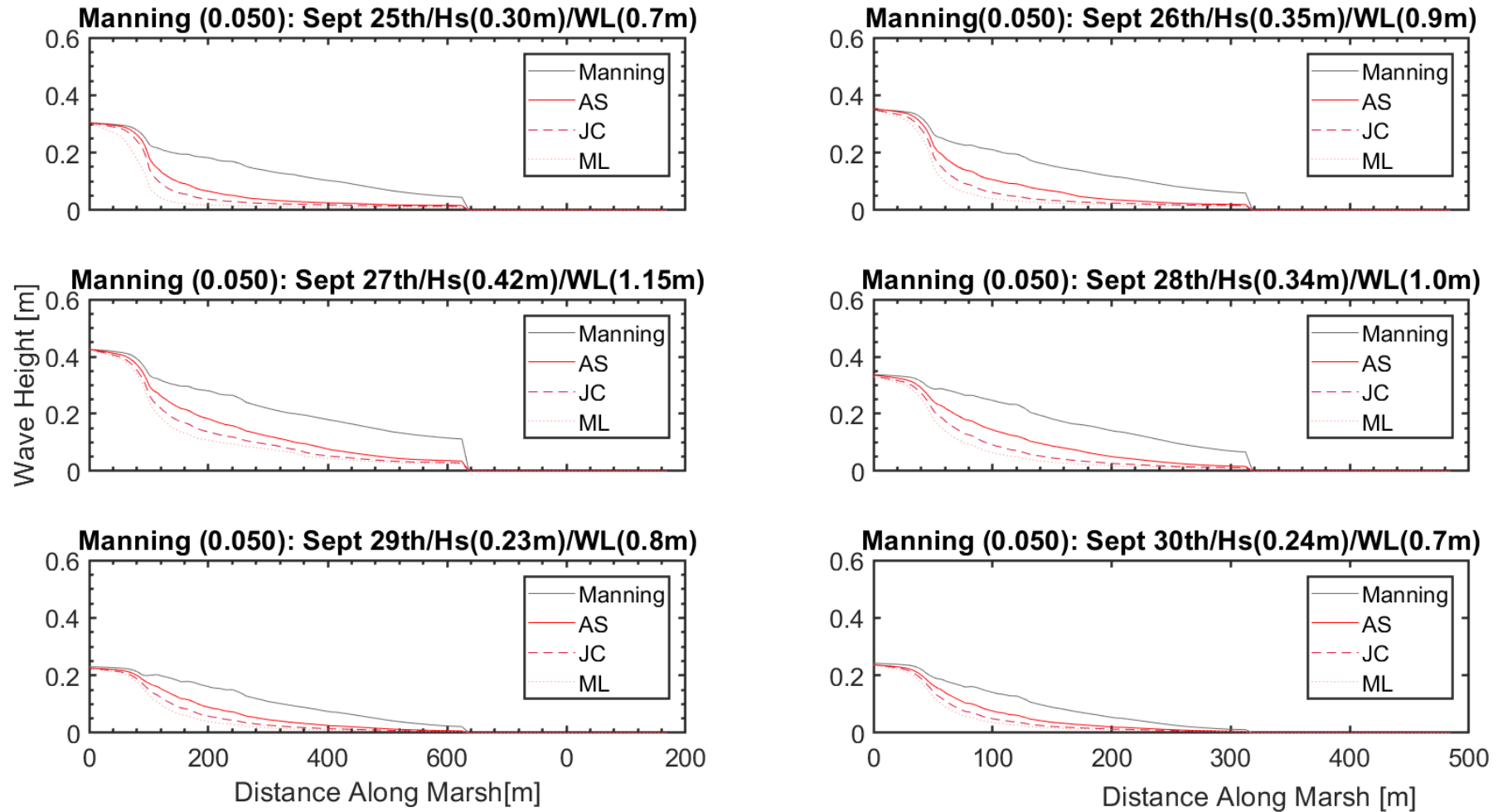
Appendix C.3

Figure 47 shows the wave height reduction profile for the manning 0.050 for each day from sept.25th to Sept. 30th.
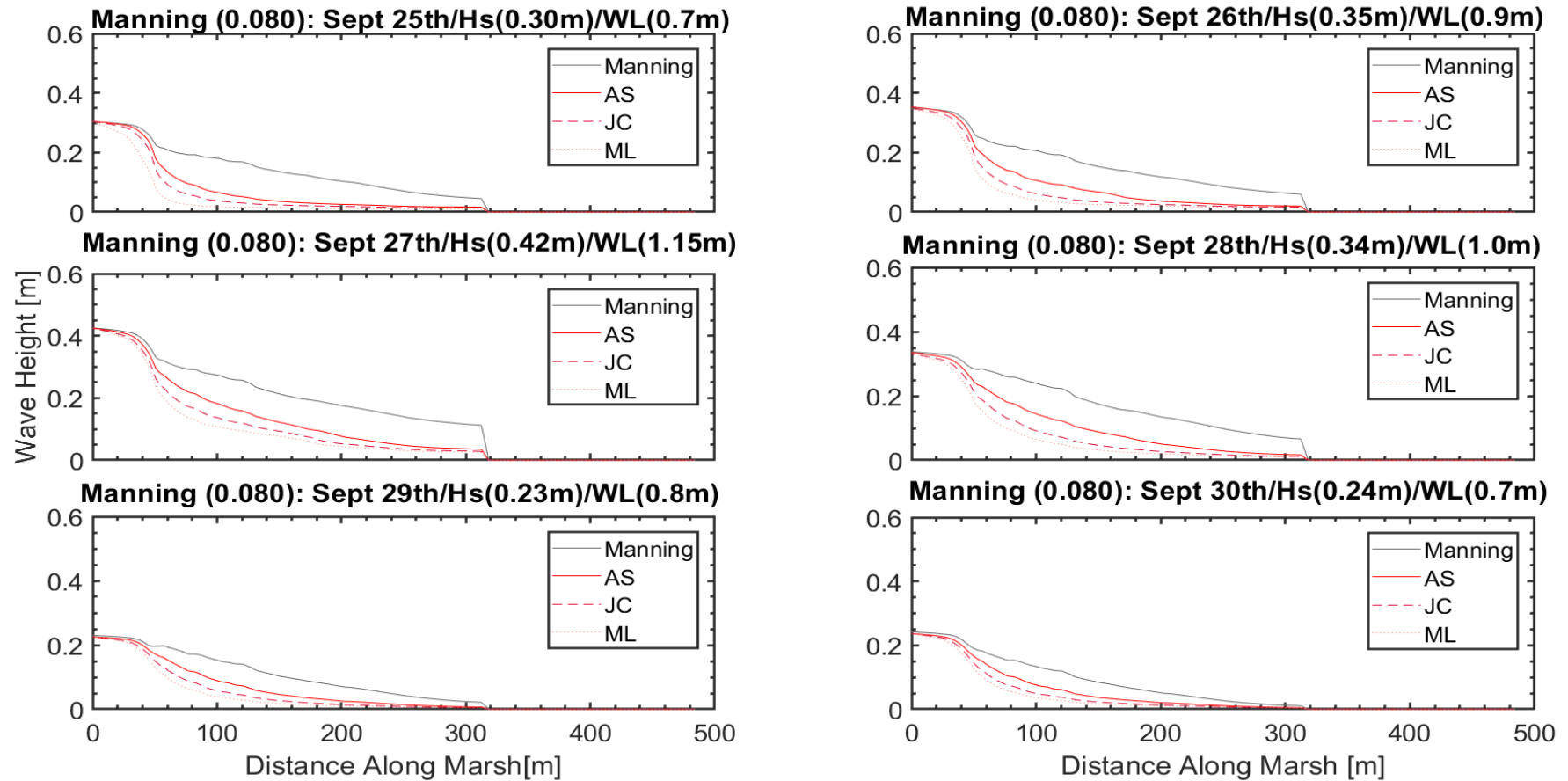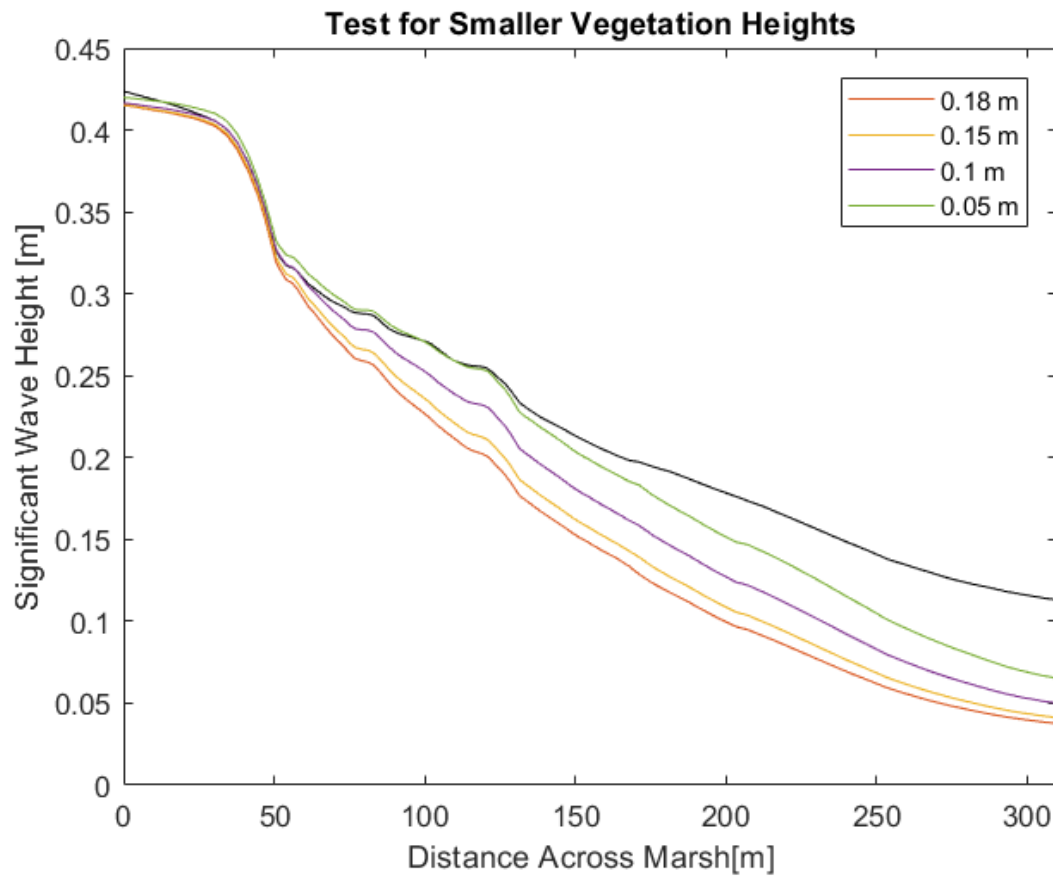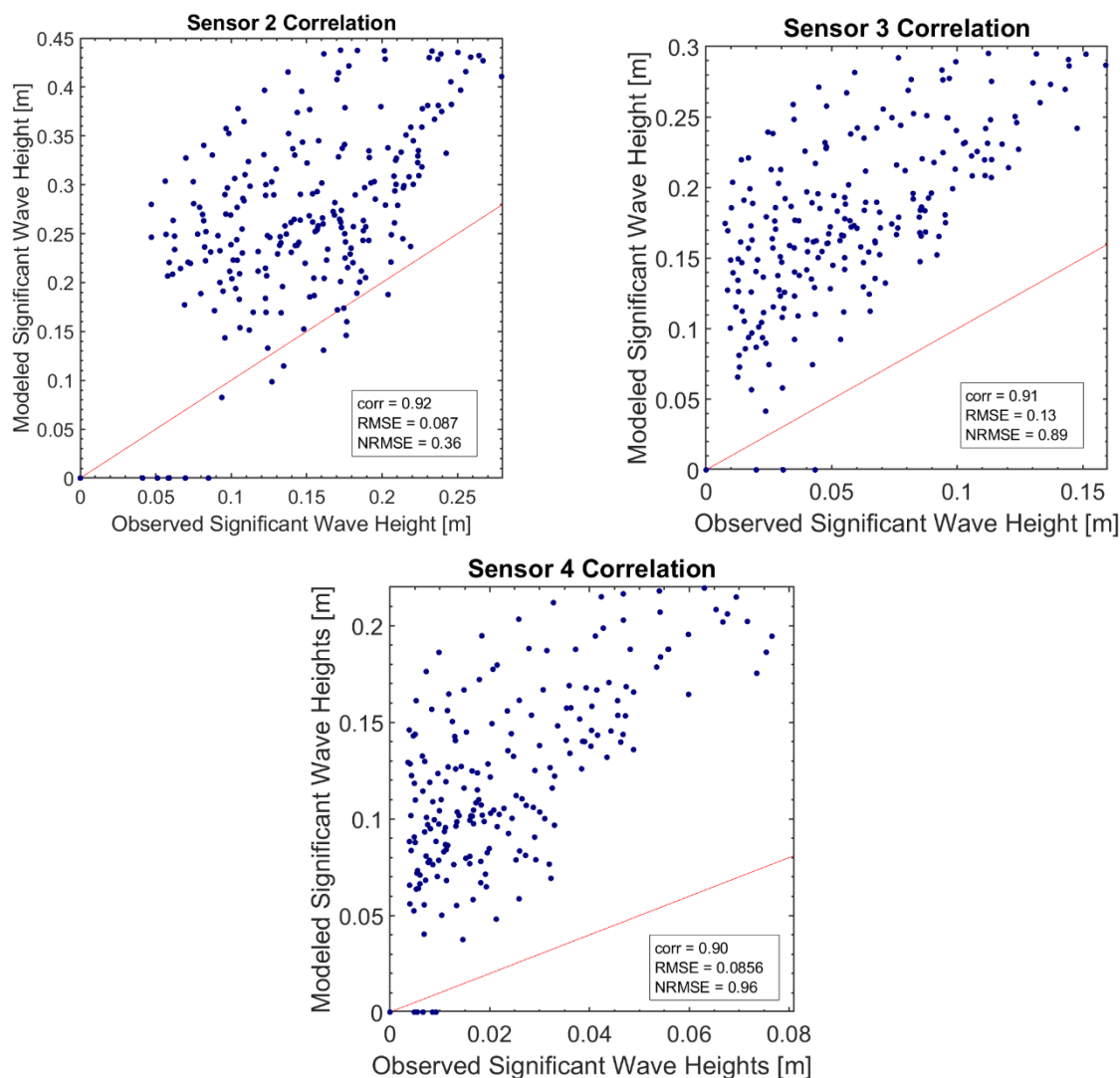
Appendix C.4

Figure 49 shows the wave height reduction profile for the manning 0.080 for each day from sept.25th to Sept. 30th.

Appendix C.5: Vegetation height reduction

Figure 50 shows the wave height dissipation profile with the vegetation height reduced to the minimal observed height of 0.18 m. then subsequently reduced to 0.15 than intervals of 0.05m. This figure is meant to illustrate at what point the implementation s begin to produce similar results.

Appendix C.5: Brief Analysis

The proceeding appendices show the results of the different days for varied manning roughness coefficients, as well as the drag formulations for the average current velocities. Each of these days have different water levels and wave heights. In all these observations, the conclusion of the paper holds, and the manning roughness shows significant underestimation of the total wave dissipation. It was also shown that the higher drag coefficients result in a better representation of the over all dissipation. At lower wave heights and water levels (Sept 29th - 30th) to total wave reduction at 310 meters is equal. However, the rate of reduction between the two implementations are significantly different. The explicit representation shows a larger initial dissipation than the implicit which dissipate the wave energy more gradually along the length of the marshland. The lower wave heights also performed better than larger wave heights, which is contrary to expectations for the manning roughness coefficient.
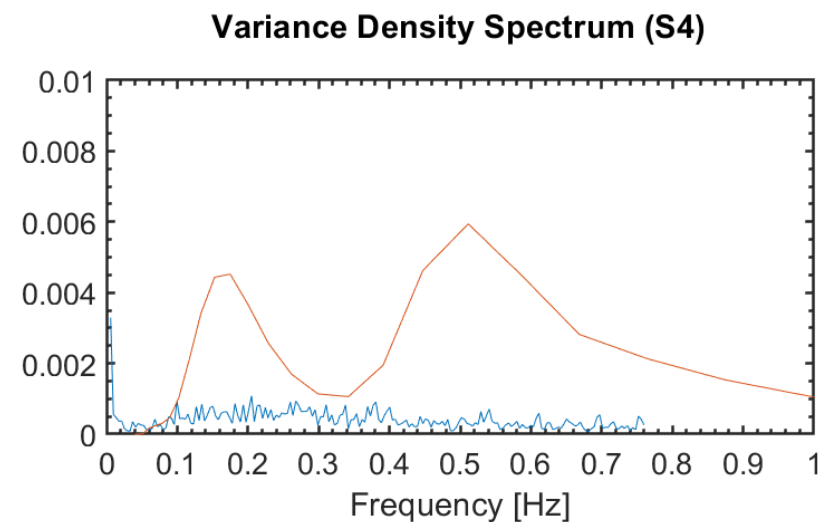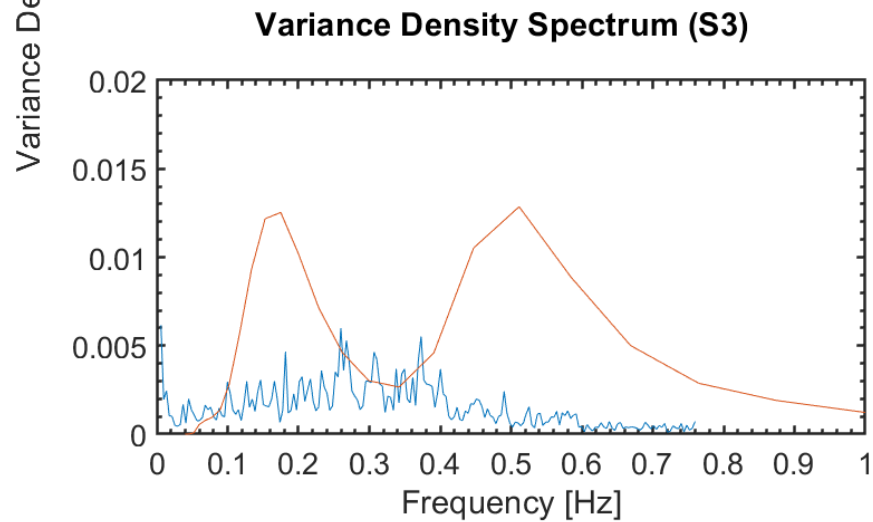
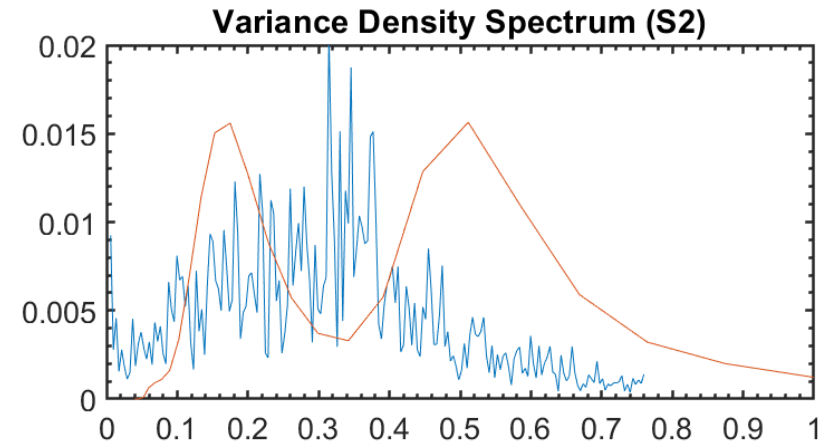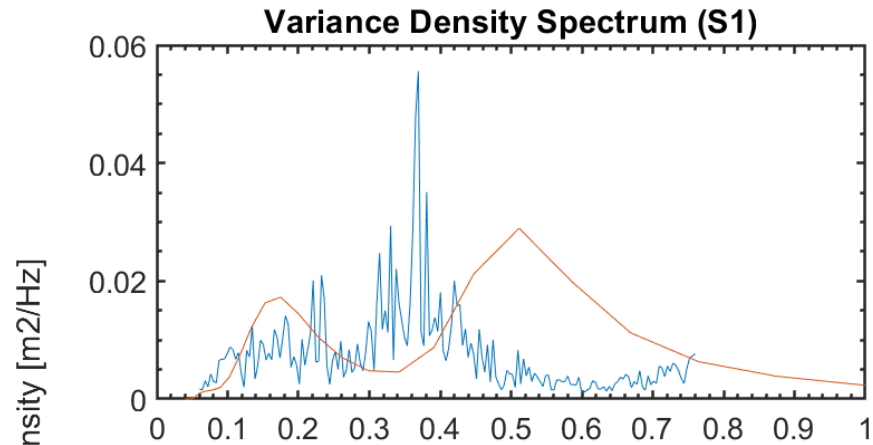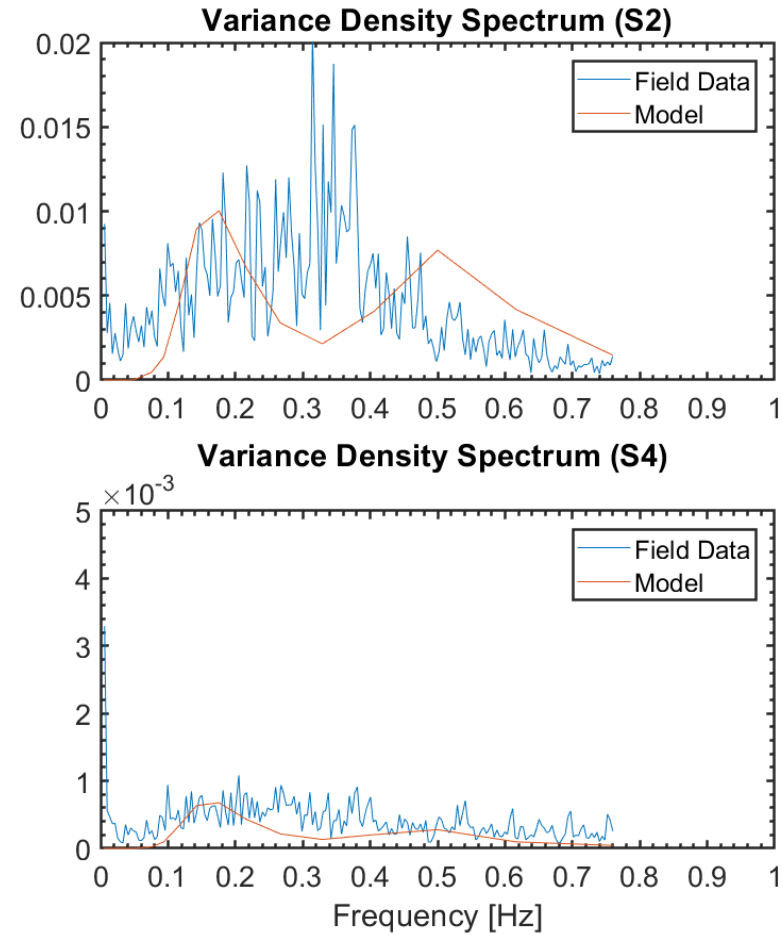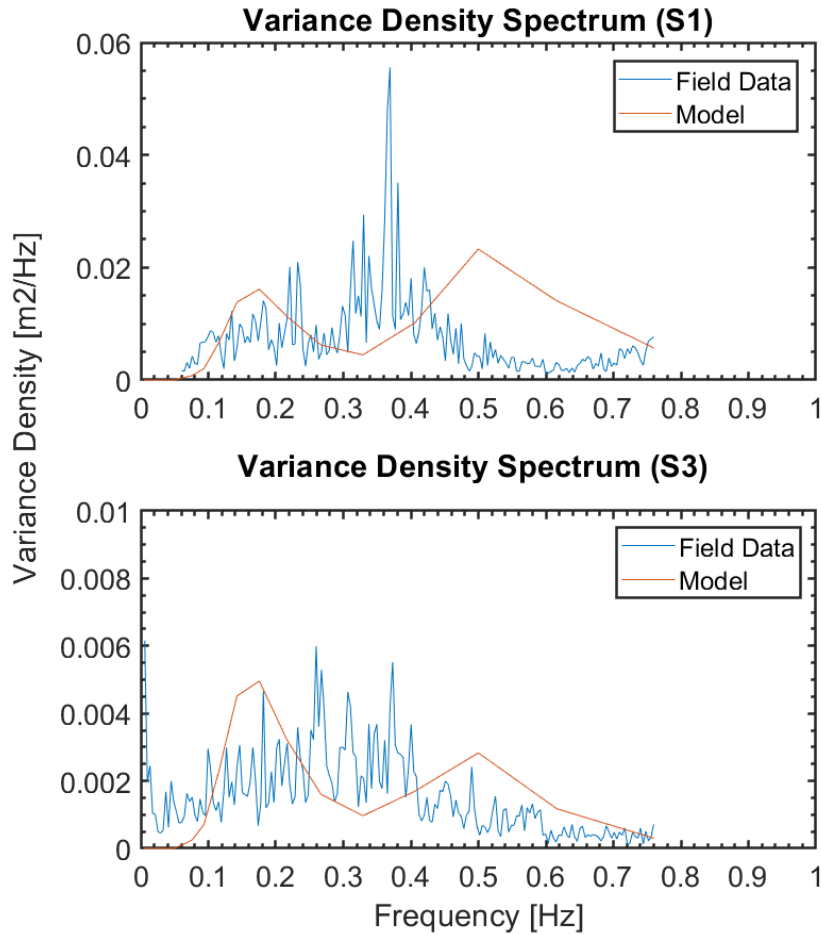## Appendix C.6: Manning Coefficient correlation

Appendix D: Spectral Profiles

Appendix D-1: Base Spectra for Domain Decomposition
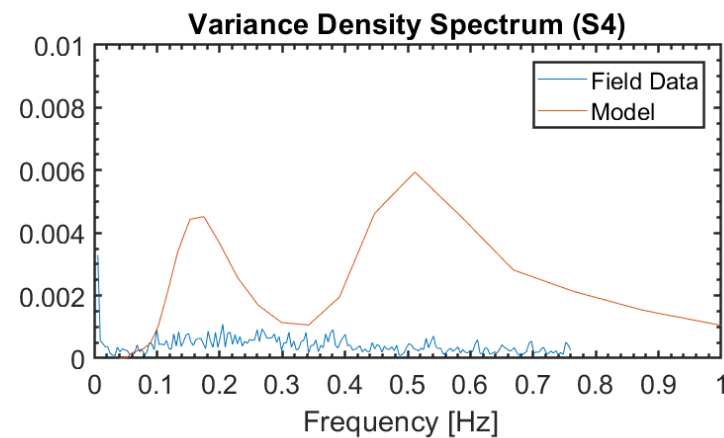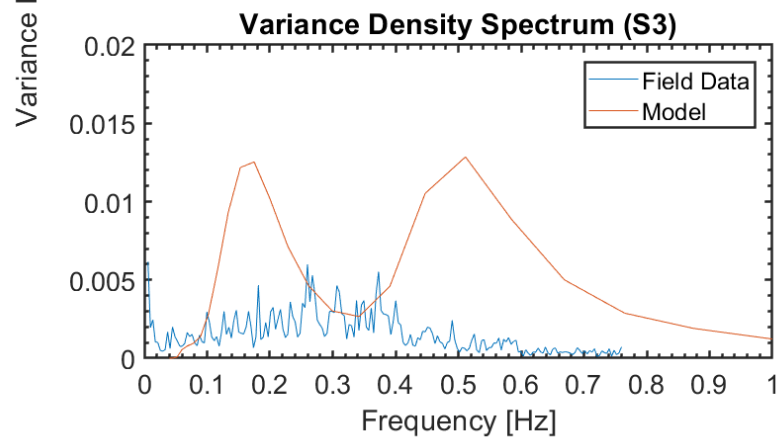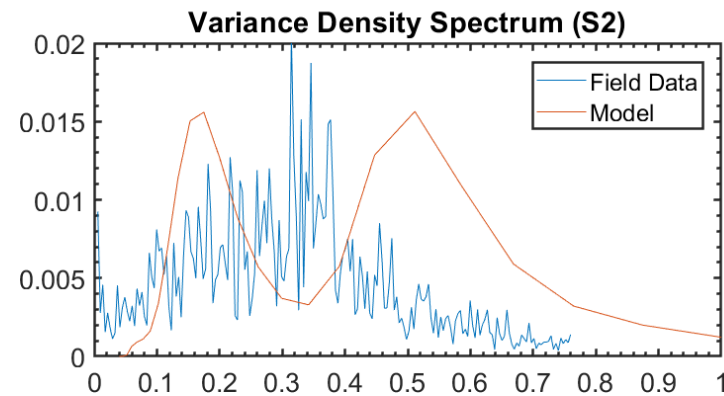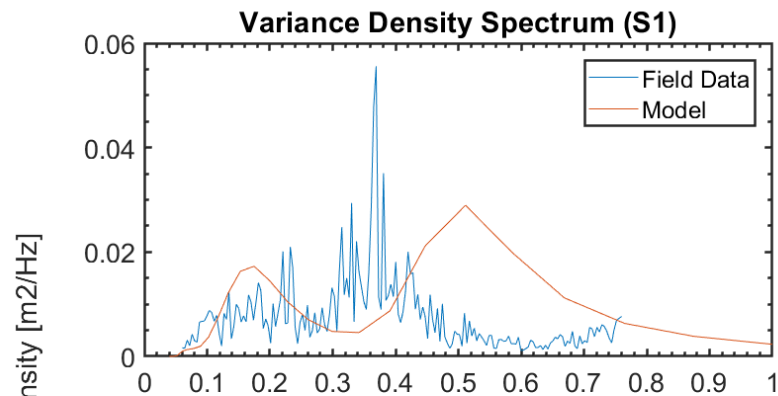
Appendix D-2: Manning Roughness Spectra SWAN Standalone

Appendix D-3: Vegetation Spectra SWAN Standalone

Appendix D.4: Pressure to energy spectrum conversion:

The East Shore wave data was recorded using four wave sensors fixed to the sea bed with a length of 0.35 meters. The data of these sensor are given in a pressure (PSI) time series recorded at 6 minutes intervals. To retrieve the Hmo and Tmo from this raw pressure data, an energy spectrum would need to be formed. This would first require the creation of the pressure spectrum, the conversion of pressure to water level, the creation of the energy spectrum and finally the extrapolation of the spectral wave height and period. The equation representing this conversion for pressure frequency components to surface wave amplitude is shown below.

$$a(f) = \frac{P(f)}{W_w K(f, z)}$$

<div align="right">**equation 29**</div>

Where a(f) represents the surface wave amplitude fluctuation as a function of frequency and the P(f) is the pressure fluctuation as a function of frequency. W_w is the specific weight of water near the surface, and K(f,z) is the vertical pressure response function. To calculate the spectrum of the time steps of the data must be in significantly small enough to resolve each individual wave. For this data information was recorded every 0.25 seconds, meaning that there will be 4 readings with 32 reading being taken on average per wave. From the raw pressure data the mean and trend needs to be removed in order to extract the tides and other low frequency waves. Not doing this will cause distortions in the results when the spectrum is determined. In the MATLAB code this was done by removing atmospheric pressure readings during the allotted time and determining the best fit trend line (polyfit).

The pressure must be converted from psi to pascals to convert this data to fluctuations in meters (multiply the pressure by 68947.6). It is important to note that the atmospheric pressure data was taken at intervals of six minutes, meaning that the intervals must be interpolated to the 0.25 second intervals found in the sensor data.

Using the pressure signal the pressure spectrum is determined through Fast Fourier Transform for a given range of frequencies, time series and transform length (typically equal to the power of 2 of the length of the series). The pressure fluctuations are windowed using the hanning windowing approach to prevent spectral leakage, which occurs when the number of waves does not fit the time series. This would lead the energy of one frequency to leak into other frequencies resulting in errors in the final analysis. Converting the pressure spectrum to an energy spectrum requires the use of the dispersion relation. From the pressure spectrums the frequency and water depth are determined. The depth was determined by a combination of GPS data and the distance of the sensors from sea bed. In the table below the depth determined by GPS for each sensor site is shown (this depth is measured from mean sea level). The distance of the sensor from the sea bed is subtracted from this depth giving the distance from the measuring point to mean sea level, this will be used in the dispersion relation. The frequency is used to determine the period needed for the resolution of the dispersion relation (Newton-

Rapshon method) shown below. From the dispersion relation, the wave number and wavelength are determined which are then incorporated into the equation 29 to calculate the a(f) or energy spectrum of the data.

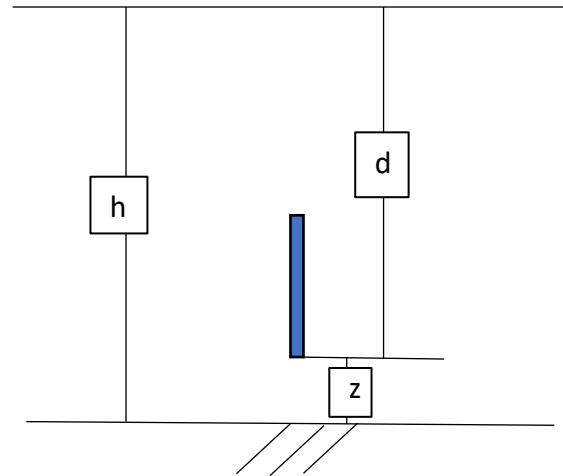| SENSOR	h	z	d (NAVD88)
S1	0.182313	0.095	0.087313
S2	0.036982	0.115	-0.078018
S3	0.06529	0.05	0.01529
S4	-0.19394	0.03	-0.223943

Figure 51 shows the values used to determin the sensor elevation of each sensors. (h) is the wvter depth, (z) is the sensor elevation, and (d) is the distance between the water surface and the boom of the sensor.
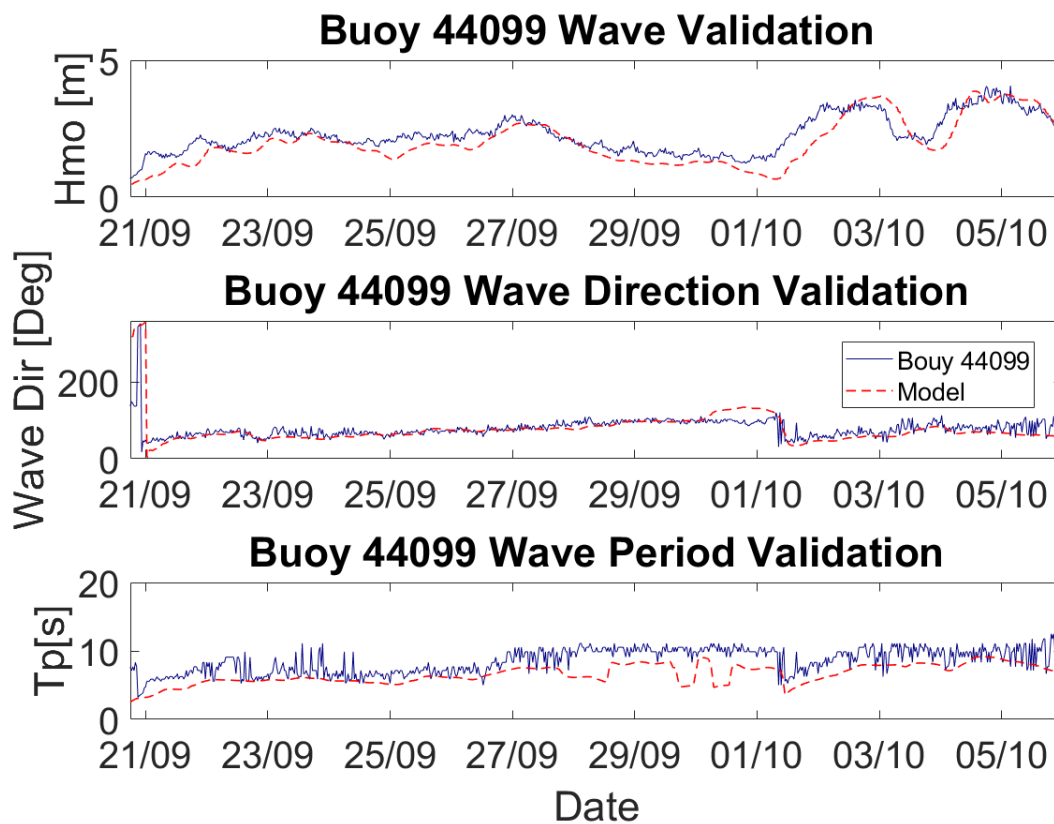
Appendix D.5: Check of Increased Wind Drag

Figure 52 shows th results of the model with an increasedwind drag coefficient. (0.003 - 0.004).

Appendix E: Marsh Description

Marsh Dissipation Description						
Vegetation Characteristics						
Height Range [m]	Ave. Height [m]	Diameter [mm]	Ave. Diameter [mm]	Stem Density [stem/m^2]	Ave. Stem Density [stem/m^2]	Drag Coef.
1.02 - 0.21	0.71	1 - 9.9	5	540 – 240	344	2.41
Storm						
Peak Wind Speed		Wind Direction			Wind Drag (Wu)	
12.72 m/s		N-NE (0-90)			0.001285-0.003	
Physical Features						
Slope		Marsh Length		Bottom Friction	Breaker Parameter	
0.4/100		500 m		0.06 (JONSWAP)	0.5	
Hydrodynamics						
Peak Significant Wave Height		Water Level Range	Depth Range	Wave Period Range	Current Velocity Range	
0.42		0 - 1.15 m	0 - 2 m	2 - 10 s	0.04 -0.7 m/s	
Wave Height Reduction						
50 [m]		80 [m]		160 [m]	310 [m]	
40%		60%		80%	90%	
0.42 - 0.25		0.25 - 0.168		0.168 - 0.084	0.084 - 0.042	
Modeling Description						
Models Applied: Delft 3D+SWAN		**Regional**	**Domain Decomposition**		**SWAN Standalone**	
Water Level cor		94%	98%		--	
Water Level NRMSE		7%	19%		--	
Wave Height cor		81%	86%		89%	
Wave Height NRMSE		10%	16%		9%	
Wave Direction cor		27%	--		--	
Wave Direction NRMSE		9%	--		--	
Wave Period cor		15%	--		--	
Wave Period NRMSE		60%	--		--	

Appendix F: Model Parameters

SWAN Model Setup		Regional/ Domain Decomposition	
Setup	Nautical convention	**Regional Grid (252,302)**	8.25 km by 8.25 km
North Orientation	90		
Coordinate	Spherical	**DD1 Grid (42,32)**	1.65 km by 1.65 km
Grid resolution	5 m		
Grid Size	107, 256	**DD2 Grid (87,82)**	330 m by 330 m
Grid Type	Curvilinear		
Frequency Grid	Circular	**DD3 Grid (117,107)**	66 m by 66 m
Freq. min	0.04 Hz		
Freq. max	1 Hz	**DD4 Grid (92,157)**	13.2 m by 13.2 m
Directional Bins	36		
Frequency Bins	24	**Wind Drag Breakpoint**	0 [m/s] 7.5 [m/s] 35 [m/s]
Boundary Shape	JONSWAP		
Peak Enhancement	3.3	**Wind Drag**	0.0012875 0.0012875 0.003
Bound Spec	Vary		
Physical Parameters	--	**Manning Regional**	0.02
Generation	3		
White capping	KOMEN	**Manning DD1**	0.02
Breaking	0.8		
Bottom Friction	JONSWAP, 0.038	**Manning DD2**	0.015
		Manning DD3	0.015
		Manning DD4	0.015
		Tidal Forcing	All
		Directional Convention	Nautical Convention
		Number of Directions	36
		Low Frequency Limit	0.04
		High Frequency Limit	1
		Number of Frequency Bins	24
		Breaker Parameter	0.5
		Bottom Friction	0.06 (JONSWAP)